Fermilab

A Search for New Gauge Bosons

in $\overline{p}p$ Collisions at $\sqrt{s} = 1.8$ TeV

by

Manoj Kumar Pillai

Submitted in Partial Fulfillment

of the

Requirements for the Degree

Doctor of Philosophy

Supervised by Professor A. Bodek

Department of Physics and Astronomy

The College of Arts and Sciences

University of Rochester

Rochester, New York

1996

Acknowledgements

My Advisor Prof Arie Bodek was the primary source of inspiration for this search. He recognised the potential of this method in the search for new physics beyond the Standard Model. I owe an immense debt of gratitude to Dr. K. Maeshima (Fermi National Accelerator Lab) who worked with me on a day to day basis, while at the same time shouldering the responsibilities of the Convenor of the Exotic Group. My thanks to Dr. C. G. Pilcher (University of Chicago) from whom I learnt a lot of numerical techniques, and to my friend and colleague, E. Hayashi, who completed the di-electron analysis, for his cooperation.

I would also like to thank my mother and sister for their patience. My thanks and warmest regards to Swami Asaktananda, Secretary, Ramakrishna Mission Ashrama (Narendrapur, WB, India), and Satya-da, our principal, without whose support and encouragement this would never have been possible.

Abstract

A search has been conducted for the existence of an additional neutral heavy gauge boson, Z', decaying to $\mu^+\mu^-$ and produced in the $\overline{p}p$ collisions at the Center-of-mass energy $\sqrt{s} = 1.8\,TeV$. The Z' is a neutral heavy gauge boson predicted to exist in several Grand Unified theories and is expected to be produced in high energy $\overline{p}p$ collisions. The data used for this search amounts to a total of $107\,\mathrm{pb}^{-1}$ of integrated luminosity collected by the CDF Collaboration at Fermilab during the 1992/1995 collider runs. From the absence of events with high invariant mass, limits are set on the production of new gauge bosons at the 95% Confidence level. The models that have been studied include a Z' with standard model like couplings, several superstring inspired E_6 models, and the Alternative Left-Right Model. By combining both $\mu^+\mu^-$ and ee decay modes a lower limit of 690 GeV is placed on the existence of a Z' with standard model like couplings.

Contents

List of Tables

List of Figures

Chapter 1

Introduction

1.1 Standard Model of Elementary Particles

The fundamental forces in Nature are of four different types:

- Electromagnetic

- Weak

- Strong

- Gravitational

They vary in their relative strengths as well as their range of action.

Within the Standard Model of particle interactions the fundamental spin-1/2 constituents of matter are classified as leptons and quarks. The leptons participate in the electromagnetic and weak interactions, and the quarks participate, in addition, in the strong interactions. Neutrinos do not participate in the electromagnetic or strong interactions. All the particles interact through the gravitational interaction. Gravitation

is not included in the following discussion because gravitational effects for elementary particle are negligible in our energy range. In addition, it is not known how to construct a quantum theory of gravity.

Based on these interactions, the fundamental fermions are grouped into generations or families. This is very much like the periodic table where the elements were classified on the basis of their structure and properties. The first generation of quarks and leptons are the lightest ones, the next generation is substantially heavier. This classification of quarks and leptons into generations is done on the basis of their mass, and the occurrence of similar properties.

Fundamental Particles					
Fermions					Bosons
Quarks	Q ($|e|$)	Leptons		Q ($|e|$)	$W^{\pm}, Z^{o}, \gamma,$
u **c** **t**	$+2/3$	ν_e ν_{μ} ν_{τ}		0	8 gluons (g)
d **s** **b**	$-1/3$	**e** μ τ		-1	Higgs (H)
• Quarks and gluons carry color (R,G,B)					
• Leptons, $W^{\pm}$,Z^{o}, γ are colorless					
• The quarks and leptons also have antiparticle counterparts					

Table 1.1: The fundamental particles of the Standard Model grouped by generation. Only the existence of the Higgs boson remains in doubt.

Table 1.1 illustrates the manner in which the various fermions are grouped into families (sometimes referred to as generations) within the Standard Model.

Historically, the first development in the direction of a field theory for particles was Quantum Electrodynamics (QED), which has been very successful in explaining the physics of all electromagnetic interactions. The electromagnetic interaction is carried by the photon, a spin 1 particle of zero rest mass, which couples to the electromagnetic charge of a particle. The next interaction that has been well investigated is the weak

interaction. Fermi's theory of Beta-decay [1], the first attempt to construct a theory of weak interactions, was based on a current-current contact interaction. This type of interaction is unrenormalisable. In order to construct a better theory for Beta decay, particles called the W^+ and W^- were introduced. However, a renormalisable theory also requires an additional particle as a partner to the W, which is referred to as the Z boson.

The Electromagnetic and the weak interaction theories are based on a field theory of particle interactions. Just as Quantum Electrodynamics (QED) has been very successful in predicting and explaining phenomena dealing with electromagnetic interactions, a similar model has been constructed for the weak interaction. This model is based on the $SU(2)_L$ symmetry of weak interactions. A. Salam and S. Weinberg [6] combined both electromagnetism and weak interaction theories into a single Unified gauge theory of electroweak interactions. This model is based on the non-Abelian gauge group $SU(2)_L \times U(1)_Y$. After the introduction of the electroweak theory, the W and the Z particles were discovered to be massive particles as predicted by the theory. The photon, by contrast, is known to be a massless particle. In order to explain this difference in masses of the bosons (and several other theoretical consequences of massive W and Z particles) a new phenomenon has been hypothesised. It requires the existence of a self-interacting isospin doublet scalar field known as the Higgs field, which interacts with the W and the Z particles, and also with all the fermions. There is a Vacuum Expectation Value (VEV) for the Higgs fields which results in the W, Z bosons acquiring masses. The theory is free from uncontrollable divergences. The Higgs boson has not been discovered yet, and is the subject of several searches.

The strong interaction is based on an SU(3) color gauge group, the quarks falling into fundamental representation of this group. This group has rank 2 and has 8 generators corresponding to which there are 8 massless gauge particles. These particles, also known as gluons, carry color quantum numbers. The self interaction between gluons results in the effective force between quarks becoming very large at large distances. In contrast to the situation in QED, this leads to "confinement" phenomenon, in which quarks are confined to within the hadrons (or mesons), and cannot exist singly.

The Standard Model of interactions is based on the $SU(3)_c \times SU(2)_L \times U(1)_Y$ gauge group which breaks down to the observed low energy $SU(3)_c \times U(1)_Q$.

There are several unanswered questions within the Standard Model. Some of the more interesting questions are whether one could reasonably continue the process of unification of the interactions, that is, have a larger gauge group from which the forces arise by symmetry breaking at other scales. One motivation for such a search is that that the standard model has a large number of parameters. It is hoped that there are some relations between these parameters. One strong hint of the existence of such a unified field theory is the cancellation of EM charge within a single generation of quarks and leptons. Renormalisation of coupling constants also predicts the existence of a Unified Gauge group for these interactions (GUTs) at mass scales near 10^{15} GeV or so. There are several such theories, some of the consequences of these theories are discussed here. Most of these theories, since they have a rank larger than the Standard Model , have an extra U(1) symmetry group (or multiple U(1)s or SU(2)s) when their symmetry is broken to accommodate the Standard Model at low energies. Such extra symmetries lead to predictions for new particles such as new gauge bosons. Even though unification

of the fundamental forces occurs at very high energy scales, some effects are manifested at low energy. Definite predictions can be made at the low energy scale concerning the particle content, behaviour, masses and couplings. Superstring theory is a natural candidate for a theory at very high energies. One clear advantage of this theory is that it does not possess any arbitrariness. All interactions and interaction strengths are well defined at the string scale, which is near the Planck scale. However, it is difficult, from this theory, to make very definite predictions about the behaviour of matter at low energies. One reason for this is the large number of ways in which the superstring theory in 10 dimensions can be reduced to an effective theory in 4 dimensions. It is so large that it is virtually impossible to study all of them to find out which one gives the correct low energy description. Suffice it to say that from the plethora of models the correct model or even a probable candidate is yet to be found.

However almost all the promising models predict the existence of extra neutral gauge particles like the Z which couple to Standard Model fermions as well as any exotic fermions. At least one of these gauge particles is expected to be light (in many models) and its couplings mix with the standard model Z. These bosons are referred to as Z' bosons.

The motivation for searching for Z' is not all theoretical. There are strong experimental reasons for searching for such a gauge boson. We have found massive gauge bosons (Z boson) in the past and it is certainly natural to expect that it may be a partner of a series of bosons. Secondly, it is also expected that all the known forces in the Standard Model emerge from some single unified force. Whatever may be the model that describes this unified theory, any such theory would be described by a larger

gauge group in which there are more neutral gauge bosons. This thesis presents an experimental search for such bosons.

1.2   Production of Gauge Bosons in $\overline{p}p$ collisions

One of the most efficient ways of observing new gauge bosons in $\overline{p}p$ collisions is to identify charged leptons in the final state. Just like the standard Z boson, one of the decay modes of these new gauge bosons is to dilepton pairs (e^+e^- or $\mu^+\mu^-$). These bosons can be produced by the Drell-Yan process: $\overline{p}p \rightarrow l^+l^-$ which is the same process that has been used in the discovery of the Z particle at CERN [2, 3, 4]. Other possible decay modes include decays to W^+W^- pairs, new fermions, or supersymmetric particles. In this search, we concentrate on the decay modes to dimuon (and dielectron) pairs only. The other decay modes are considered indirectly by including their effect on the partial width of the Z' boson.

The production and decay of these gauge bosons is described, in the lowest order, by the Lagrangian:

$$L_{NC} = \overline{\psi}^k \gamma_\mu (v_\alpha^k + a_\alpha^k \gamma_5) \psi^k Z_\alpha^\mu \tag{1.2.1}$$

where α refers to different gauge bosons and the summation over the space-time index μ and the particle indices α and k is understood. Here, Z_α represent the physical gauge bosons of definite mass M_α and width , $_\alpha$. Values of $\alpha = 1,2$ correspond to the Standard Model photon and the Z boson, and $\alpha = 3,4$ corrspond to possible extra neutral gauge

bosons, which may appear in extensions of the Standard Model. The v's and the a's

correspond to vector and axial vector couplings to the appropriate fermions.

For the Standard Model, these couplings are given in Table 1.2. In this table, s_W is

the quantity $\sin\theta_W$ and c_W is the quantity $\cos\theta_W$, where θ_W is the Glashow-Weinberg

mixing angle (also called the electroweak mixing angle) involved in the Electroweak

symmetry breaking. The quantity e is the electron charge.

Table 1.2: Standard Model couplings of known fermions to electroweak gauge bosons.

Coupling constant	γ	Z
v^u	$\frac{2}{3}$e	$\frac{e}{s_W c_W}\left(\frac{1}{4} - \frac{2}{3}s_W^2\right)$
a^u	0	$-\frac{e}{s_W c_W}\frac{1}{4}$
v^d	$-\frac{1}{3}$e	$\frac{e}{s_W c_W}\left(-\frac{1}{4} + \frac{1}{3}s_W^2\right)$
a^d	0	$\frac{e}{s_W c_W}\frac{1}{4}$
v^e	-e	$\frac{e}{s_W c_W}\left(-\frac{1}{4} + s_W^2\right)$
a^e	0	$\frac{e}{s_W c_W}\frac{1}{4}$
v^ν	0	$\frac{e}{s_W c_W}\frac{1}{4}$
a^ν	0	$-\frac{e}{s_W c_W}\frac{1}{4}$

Using the Lagrangian in equation 1.2.1, the differential cross-section for the Drell-

Yan process $\overline{p}p \to l^+l^-$ can be calculated. The cross section depends on the kinematics

of the dilepton pair in the final state. These include the dilepton invariant mass (M),

rapidity (y), and the production angle in the centre of mass of the partons in the collision

(θ^*). This differential cross section is given by

$$\frac{d\sigma}{dM\,dy\,dcos\,\theta^*} = \sum_{q=quarks} [g_S^q(y,M)S_q(M)(1+cos^2\theta^*) + g_A^q(y,M)A_q(M)2cos\theta^*]$$

(1.2.2)

where S_q and A_q involve the vector and the axial vector couplings of the quarks and the leptons to different neutral gauge bosons, and g_S^q, g_A^q involve the parton distribution functions. Both θ^* and y dependences are usually integrated over.

The quantities $g_{S,A}^q$ in Equation 1.2.2 are given by:

$$g_{S,A}^q = \frac{M}{48\pi}x_ax_b[f_q^{(a)}(x_a,M^2)f_{\bar{q}}^{(b)}(x_b,M^2) \pm f_{\bar{q}}^{(a)}(x_a,M^2)f_q^{(b)}(x_b,M^2)]$$

(1.2.3)

and the sign $+(-)$ correspond to S (A), and

$$S_q = \sum_{\alpha,\beta} \frac{(v_\alpha^q v_\beta^q + a_\alpha^q a_\beta^q)(v_\alpha^l v_\beta^l + a_\alpha^l a_\beta^l)}{(M^2 - M_\alpha^2 + iM_{\alpha,\,\alpha})(M^2 - M_\beta^2 - iM_{\beta,\,\beta})}$$

(1.2.4)

$$A_q = \sum_{\alpha,\beta} \frac{(v_\alpha^q a_\beta^q + a_\alpha^q v_\beta^q)(v_\alpha^l a_\beta^l + a_\alpha^l v_\beta^l)}{(M^2 - M_\alpha^2 + iM_{\alpha,\,\alpha})(M^2 - M_\beta^2 - iM_{\beta,\,\beta})}$$

(1.2.5)

In Equations 1.2.5 and 1.2.3 standard conventions are used as in [22] and [23]. The quark and lepton masses have been neglected in this equation; a and b are the two colliding hadrons at the center of mass energy $\sqrt{s}$; and x_a and x_b are the momentum

fractions of the colliding partons (Figure 1.2). For the lepton-antilepton pair of invariant mass M, the rapidity y is related to the momentum fractions of the colliding parton as follows:

$$x_{a,b} = \frac{M}{\sqrt{s}} e^{\pm y} \tag{1.2.6}$$

The quantities, $f_{q,\bar{q}}^{a,b}$, are the relevant parton distribution functions for the proton. These functions give the probability that a parton with the appropriate momentum fraction is formed out of a proton. The mass dependence is obtained by integrating over the other variables in Equation 1.2.2

$$\left(\frac{d\sigma}{dM} \right)^S = \int_{ln(\frac{M}{\sqrt{s}})}^{ln(\frac{\sqrt{s}}{M})} dy \int_{-1}^{1} dcos\theta^* \frac{d\sigma}{dM \, dy \, dcos \, \theta^*} \tag{1.2.7}$$

We search for Z' bosons that are predicted to exist in E_6 based models. For these models, the low energy gauge structure is $SU(3)_C \times SU(2)_L \times U(1) \times U(1) \times U(1)$, and the neutral-current Lagrangian can be written in the form,

$$L_{NC} = J_{\beta\mu} C_{\beta\alpha} Z_{\alpha}^{\mu} \tag{1.2.8}$$

where the currents are the properly normalized currents corresponding to the orthog-

onal generators in E_6. The action of the generators on the fundamental representation

of E_6 is given by Table 1.3

Table 1.3: Action of the orthogonal basis (T_{3L}, Y, Y', Y'') for E_6 neutral currents on the fundamental representation, $\underline{27}$

	T_{3L}	$\sqrt{\frac{5}{3}}Y$	$\sqrt{\frac{5}{3}}Y'$	$\sqrt{\frac{5}{3}}Y''$
$\begin{pmatrix} u \\ d_1 \end{pmatrix}$	$\frac{1}{2}$ $-\frac{1}{2}$	$\frac{1}{6}$	$\frac{1}{3}$	0
d_{2L}	0	$-\frac{1}{3}$	$-\frac{2}{3}$	0
u^c	0	$-\frac{2}{3}$	$\frac{1}{3}$	0
d^c_{1L}	0	$\frac{1}{3}$	$-\frac{1}{6}$	$\frac{1}{2}$
d^c_{2L}	0	$\frac{1}{3}$	$-\frac{1}{6}$	$-\frac{1}{2}$
$\begin{pmatrix} \nu_1 \\ e_1 \end{pmatrix}$	$\frac{1}{2}$ $-\frac{1}{2}$	$-\frac{1}{2}$	$-\frac{1}{6}$	$\frac{1}{2}$
$\begin{pmatrix} \nu_2 \\ e_2 \end{pmatrix}$	$\frac{1}{2}$ $-\frac{1}{2}$	$-\frac{1}{2}$	$-\frac{1}{6}$	$-\frac{1}{2}$
$\begin{pmatrix} e^c_2 \\ \nu_3 \end{pmatrix}$	$\frac{1}{2}$ $-\frac{1}{2}$	$\frac{1}{2}$	$-\frac{2}{3}$	0
e^c_{1L}	0	1	$\frac{1}{3}$	0
ν_{4L}	0	0	$\frac{5}{6}$	$-\frac{1}{2}$
ν_{5L}	0	0	$\frac{5}{6}$	$\frac{1}{2}$

The model dependence that does not originate from the fermion assignments in

the E_6 gauge group is through the constants $C_{\beta\alpha}$. These can depend only on three

parameters, one of which can take only two values, and are chosen as θ_1, θ_2 and λ.

The value of θ_3 is fixed by other constraints [5]. One can also consider a mixing angle

β between the different fermions, as discussed in Ref [5]. In table 1.4, we show the

parameters for several models which have been investigated in this search.

One of the models that we investigate and set mass limits on Z' bosons (within this

Table 1.4: Parameters of Superstring inspired E_6 models (cf Aguila, et. al. in References)

	θ_1	(c_2,s_2)	λ	$\sin\beta$	($\lambda = 1$, no θ_1 dependence)
Z_η	$\left[-\frac{1}{2}\pi, \frac{1}{2}\pi\right)$	$(1,0)$	$[1,1.2)$	-	minimal Higgs breaking
Z	$\left[-\frac{1}{2}\pi, \frac{1}{2}\pi\right)$	$\left(\sqrt{\frac{5}{8}}, -\sqrt{\frac{3}{8}}\right)$	$[1,1.2)$	0	intermediate scale Higgs breaking
Z_χ	$\left[-\frac{1}{2}\pi, \frac{1}{2}\pi\right)$	$\left(\sqrt{\frac{3}{8}}, \sqrt{\frac{5}{8}}\right)$	$[1,1.2)$	1	intermediate scale Higgs breaking
Z_I	$\left[-\frac{1}{2}\pi, \frac{1}{2}\pi\right)$	$(0,1)$	$[1,1.2)$	-	intermediate scale Higgs breaking

model) is the "Standard Model" Z'. This model refers to a Z' with Standard Model couplings to the known fermions, and a width that is proportional to the mass of the Z'. However, the notation "Standard Model" Z' should be understood properly in that it refers to the values of the assumed couplings only. It should be clarified that an extra Z' boson is not predicted to exist within the Standard Model of particle interactions.

A plot of the total widths of the Z' in different E_6 models is shown in Fig 1.2. Note that the width of a standard model Z' is assumed to be proportional to its mass, and is therefore equal to 2.5 GeV at the Z mass (91 GeV).

The branching ratio for a Z' decaying to dielectrons or dimuons depends on the number of the decay processes available. Typical values of these branching ratios are shown in the Table 1.5 for superstring inspired models relative to the branching ratio of a Z to dielectrons or dimuons (measured to be 0.033).

Table 1.5: Branching ratio (Bratio) to dielectrons or dimuons (divided by 0.033 which is the dielectron branching ratio of the 91 GeV Z) for Superstring inspired E_6 models (cf Aguila, et. al. in References)

E_6 Models	Bratio/Mass(GeV)
Z_η	1.365/91.
	1.159/1000.
Z	1.554/91.
	1.338/1000.
Z_χ	1.906/91.
	1.85/1000.
Z_{LR}	0.53/91.
	0.417/1000.
Z_I	1.803/91.
	1.703/1000.
Z_{SM}	1.000/91.
	0.910/1000.
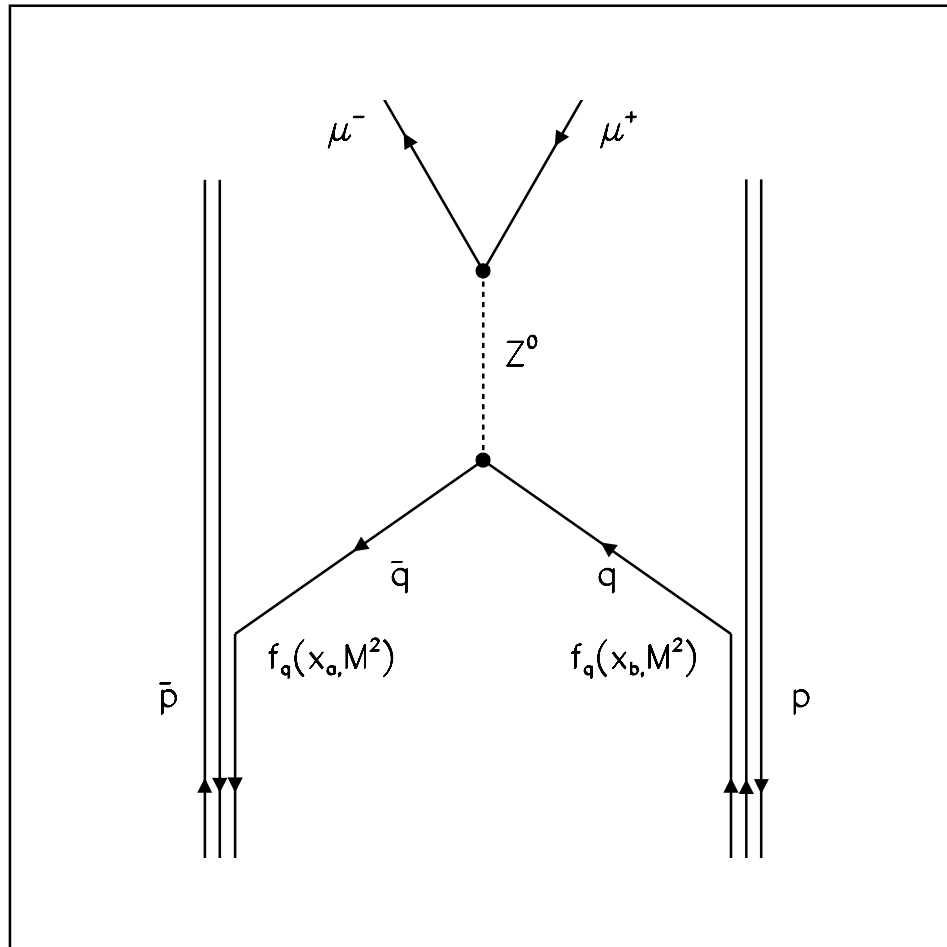
Figure 1.1: This figure shows the collision of a quark-antiquark pair producing a lepton-antilepton pair. The proton and antiproton are represented by p and $\bar{p}$, the quarks by q and $\bar{q}$ the muons by $\mu^{\pm}$, and the Z particle is represented by Z^0. The quantities f (with the appropriate subscripts) represent the structure functions.
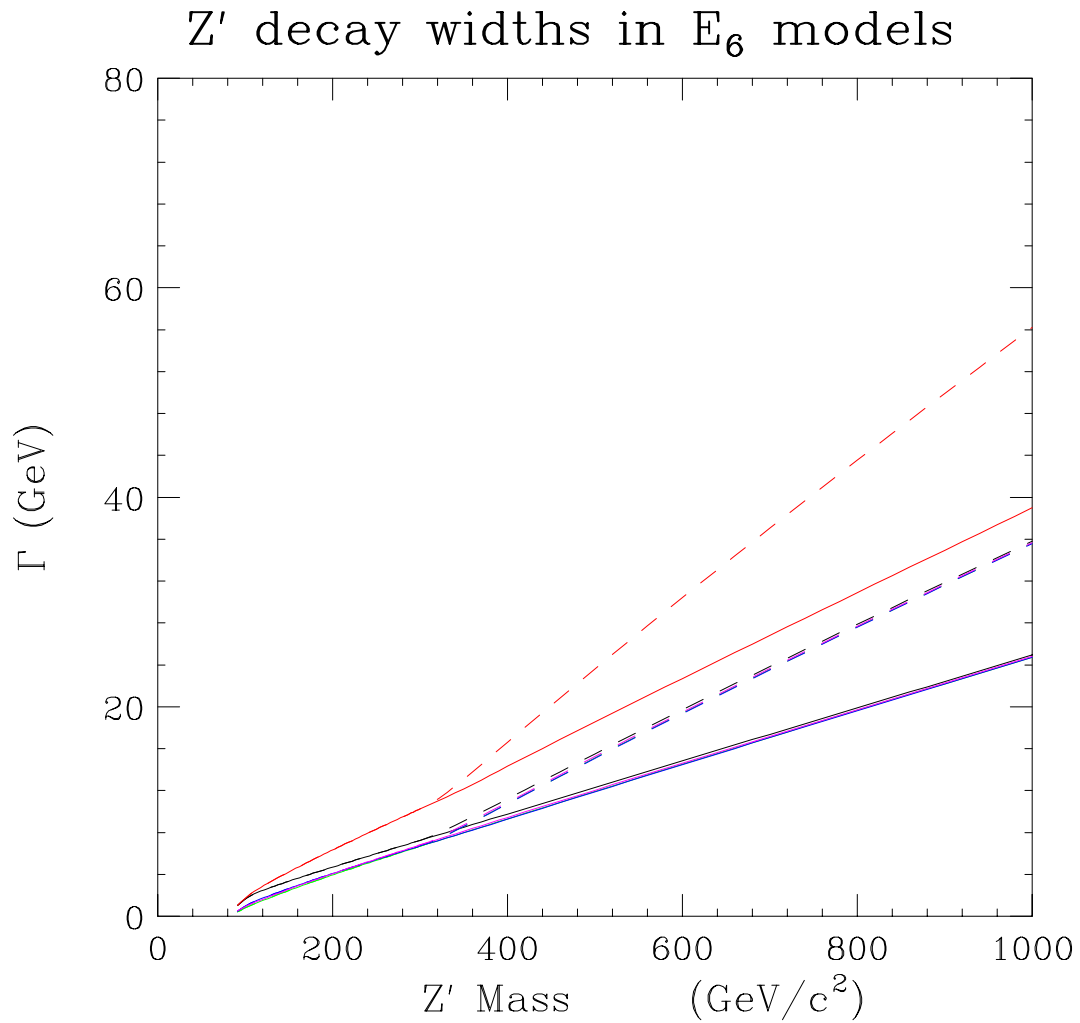
Figure 1.2: The Width of the decay of a Z' to dileptons as a function of the mass of the Z' for several E_6 models. The solid lines represent the case when the Z' is allowed to decay into the known fermions only (the decays into other fermions could be kinematically forbidden, for instance). The dashed lines represent the case when Z' decays into exotic and supersymmetric fermions in the model.

Chapter 2

Experimental Apparatus

2.1 The Tevatron

The Tevatron at Fermilab, a unique superconducting synchrotron designed to acceler-
ate protons and antiprotons, is the highest energy machine available in the world. It
is also a storage ring in which $\overline{p}p$ collisions occur at a center of mass energy of 1.8
TeV. Figure 2.1 shows a diagram of the Tevatron. It is a ring two kilometers in diame-
ter, utilizing superconducting magnets and radio-frequency fields to accelerate charged
particles. Negatively charged hydrogen ions are accelerated by a Cockroft-Walton gen-
erator to 750 keV. The electrons are stripped from the hydrogen ions, and the protons
are accelerated by linear accelerator(LINAC) to an energy of 400 MeV. The Booster
ring, a synchrotron, subsequently accelerates the protons to 8 GeV. The protons are
then injected into the Main Ring, which is a two kilometer diameter synchrotron using
conventional magnets. The Main Ring accelerates the protons to an energy of 150 GeV.
This proton beam is also used for the production of antiprotons by directing the protons

onto a tungsten target. Antiprotons are collected and stored in an Accumulator Ring where stochastic cooling is used to reduce their spatial and momentum dispersion. The antiprotons are subsequently accelerated to 150 GeV in the Main ring, injected into the Tevatron, and then accelerated to 900 GeV in a direction opposite to that of the protons. The proton and antiproton beams intersect at 4 points along the circumference of the ring. There are only 2 collision points, and at the other two points the beams are kept from colliding by using electrostatic separators. Quadrupole magnets are used to focus these beams to a diameter of approximately 40 μm at the B0 and D0 collision points. The Collider Detector Facility (CDF) is located at the B0 collision point.
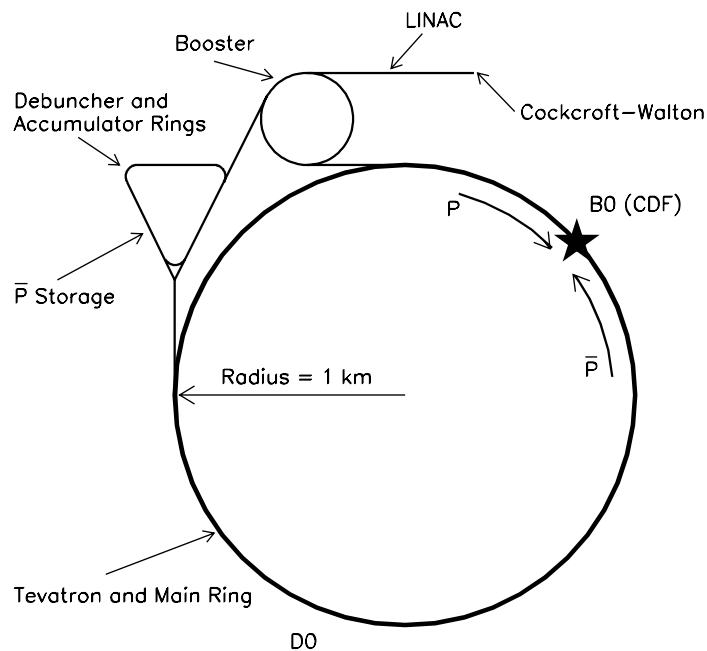
Figure 2.1: A schematic diagram of the layout of the various accelerators used at Fermilab to provide $p\overline{p}$ collisions at a center of mass energy of 1.8 TeV.

2.2 The CDF detector

The CDF detector at Fermilab (Figure 2.2) consists of several different elements designed to identify particles and measure their energy and momentum. Figure 2.2 shows a cutaway section of a quadrant of the CDF detector. A detailed description of the CDF detector may be found in Reference [8] and references therein. The analysis will be described in cylindrical coordinates, which is the natural system for the description of the detector. The principal axes are r-ϕ and z. The z axis is oriented along the beam line, in the direction of motion of the proton bunches. The detector is approximately cylindrical, with its axis along the z direction and its center located at the collision point.

It is convenient to use a different variable θ (the polar angle) instead of the cylindrical z variable, and we define it here:

$$z = r \times \cot \theta$$

where, θ is the angle subtended by the line joining the point under consideration with the positive z axis.

Another quantity that is frequently used is the the pseudorapidity variable, η, which is related to the z coordinate or the polar angle θ,

$$\eta = -log\ tan\ \frac{\theta}{2}$$

In terms of the pseudorapidity variable the Central detector extends from $\eta = 0$ to 1.1 (on either side), while the Plug region (not relevant to this analysis) extends from $\eta = 1.2$ to 2.4.

The $\bar{p}p$ collisions occur approximately at the center of the detector. Scintillator planes (beam-beam counters) are located at small angles to the beam direction and signal a collision. These counters are also used to determine the total integrated luminosity.

2.2.1 Central Tracking Chamber

The Central Tracking Chamber (CTC) is located in a 1.4116 Tesla magnetic field produced by a 4.8 m long superconducting solenoid of radius 1.5 m. The magnetic field strength is determined by the current flowing in the superconducting solenoid and is independently monitored by an NMR probe which is accurate to one part in ten thousand. It is this magnetic field that enables the measurement of the momentum of charged particles.

The CTC is a drift chamber with 84 cells, which are divided into nine superlayers. Five of these superlayers (also known as the axial superlayers) have their sense wires parallel to the beamline. Interleaved with these layers are four stereo superlayers with their wires at an angle of $\pm$ 3° with respect to the axis of the cylinder. High energy
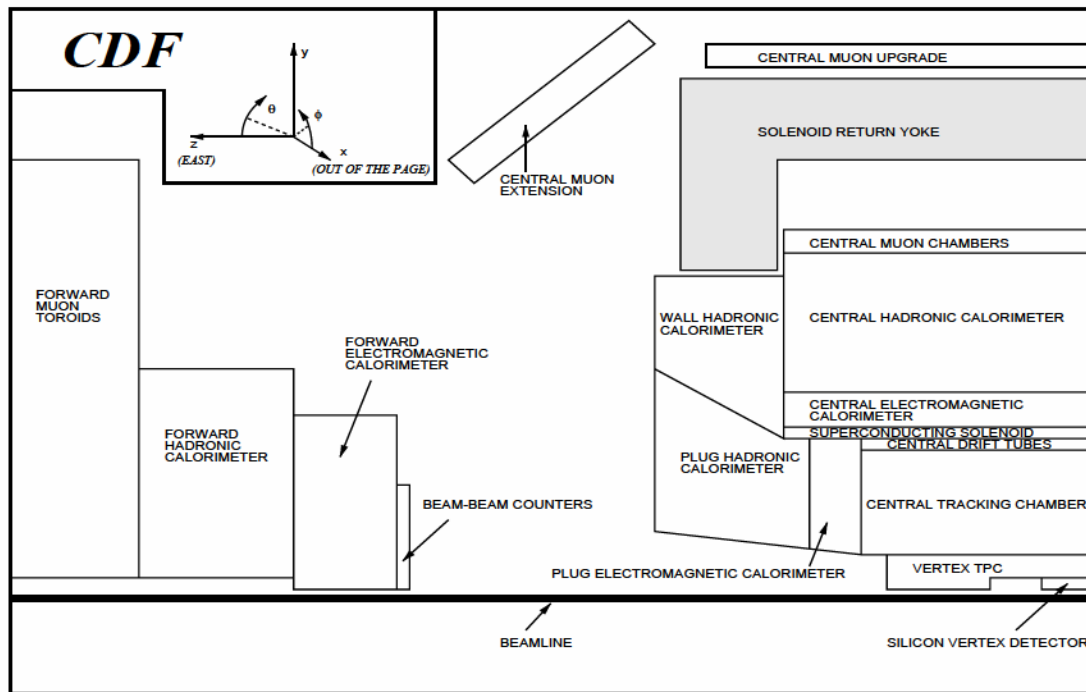
Figure 2.2: A cut-away diagram of the various components of the CDF detector (the interaction point is in the lower right corner). The coordinate system is defined by the proton beam momentum being in the $+z$ direction.

charged particles produce ionization in the gas within the CTC and this charge is collected on the sense wires. The drift time of the charge to the axial wires yields the r-ϕ position of the hits (the position where the charge was collected). The stereo wires, together with the axial wires are used in determining the z-position of the hits. A three dimensional sequence of hits is fitted to form a track. The curvature of the track in the magnetic field is inversely proportional to the transverse momentum of the particle and yields the momentum, and the charge of the particle. For tracks at 90° , the resolution is given by

$$\frac{\delta P_T}{P_T} \;\; = \;\; 0.0010 \times P_T \;\; in \;\; GeV/c,$$

and the z resolution is $\sim$ 4 mm. where, P_T is the particle's transverse momentum.

For this analysis, the momentum of the muons is determined from the CTC tracks. The invariant mass of the dimuon pair is found from the momenta and angles of the tracks.

2.2.2 Vertex Finding

A Vertex tracking chamber (VTX) is used to determine the precise location of the event vertex. The chamber covers almost seven units of pseudorapidity, and is optimised to provide good pattern recognition in the r-z plane. It consists of eight dual-time projection chambers surrounding the beam pipe which are mounted end-to-end along the beam direction. The position resolution of the z-vertex as determined by the VTX is of the order of a few mm. For the purpose of this analysis, these vertices are important for two reasons. First, the vertices are used to constrain the tracks of the charged particles which results in improved momentum resolution. Secondly, this constraint also removes a major fraction of the cosmic ray background. This is because cosmic rays are single muons coming from outside the detector and therefore do not necessarily come close in space or time to real event vertices.

2.2.3 Calorimetry

The calorimeters are used to determine the energies of electrons and hadrons. The CDF detector includes both lead Electromagnetic(EM) and iron Hadronic(HAD) sampling calorimeters which provide complete coverage in ϕ and extend out to 1.1 in η. The active media of the EM and HAD portions of the central calorimeters are scintillators. Coverage at forward angles is provided by the plug and forward calorimeters, which utilize gas proportional chambers as active media. In the central region, the scintillators are read out using wavelength-shifting light guides and Photomultiplier tubes(PMTs). The signals are fed into Analog to Digital Converters(ADCs), which are connected to other electronics (RABBIT/FASTBUS) for Data Acquisition(DAQ). The high voltage supplies to the PMTs are controlled and recorded continuously by computers during data taking. The RABBIT/FASTBUS systems are in turn connected through a series of networks and cables to computers which perform the DAQ. The calorimetry is very important in the identification of muons, which are essentially minimum ionizing particles. The calorimeter has a "tower structure", in other words, it is segmented in η and ϕ. Each tower spans $15°$ in ϕ and 0.1 in η (corresponding to the z-direction).

There are strip chambers in the central EM and Plug calorimeters. The strip chambers are located at the EM shower maximum, and are used to measure lateral shower profiles and thereby identify the particles that caused the showers (e.g. electrons, photons and neutral pions).

2.2.4   Muon Chambers

Muon chambers in the CDF detector are classified into several different types depending on the region of the detector where they are located. The first kind of muon chambers are located in the Central region and are known as the Central Muon Chambers or the CMU. They are drift chambers, located on top of the calorimeter wedges in the central region of the detector. They have wires which are offset so as to permit the accurate reconstruction of the track segment of a muon. The Central Muon Chambers are backed up by a second set of drift chambers which are located behind 8 absorption lengths of steel. These are the CMP or the Central Muon Upgrade chambers. The Central Muon Extension chambers (CMX) are located at a higher η compared to the Central Muon chambers(CMU). In the very forward direction are the Forward Muon Chambers (FMU), which are not used in this analysis. The location and coverage of the muon chambers in $\eta - \phi$ are shown in Figure 2.3.

Figure 2.3 shows the regions in η-ϕ covered by the muon chambers in the CDF detector. Different muon chambers cover different regions of the detector. The CMU and the CMP chamber coverage is the most relevant to this analysis.

2.3   Trigger

The recorded events are pre-selected by means of an online trigger. The CDF detector has a three-level trigger. The lowest level of triggering (Level 1) requires a minimum energy to be deposited in the calorimeter, with a corresponding signal in the beam-beam counters, to indicate a collision. The Level 2 trigger, during Run 1A, was a fastbus based

triggering system. At Level 2, calorimeter clusters are identified (clusters of energy) and tracks are reconstructed from the hits in the Central Tracking Chamber(CTC) by the Central Fast Tracker(CFT). These tracks (in r-ϕ) are then matched either to Electromagnetic clusters in the EM calorimeter, or to track segments in the muon chambers. When a track matches a muon stub to within 5 degrees in ϕ (the "muon matchbox"), it results in a trigger. Muons in the central region can trigger in the region $|\eta| < 0.6$. The output of the Level 2 trigger is sent to Level 3. The latter is a Silicon Graphics computer farm, with the ability to have an event being read in or written out of its buffer space while a second event is being processed. The complete offline reconstruction code was run at this level, with the exception of the transverse energy (E_t) which was calculated assuming z=0 and the initial database constants. A fraction of these events, which satisfy very restrictive criteria, are flagged for immediate offline processing. This data stream is referred to as the "express stream".

CDF η-φ Map for Central Muons

- CMX   - CMP   - CMU
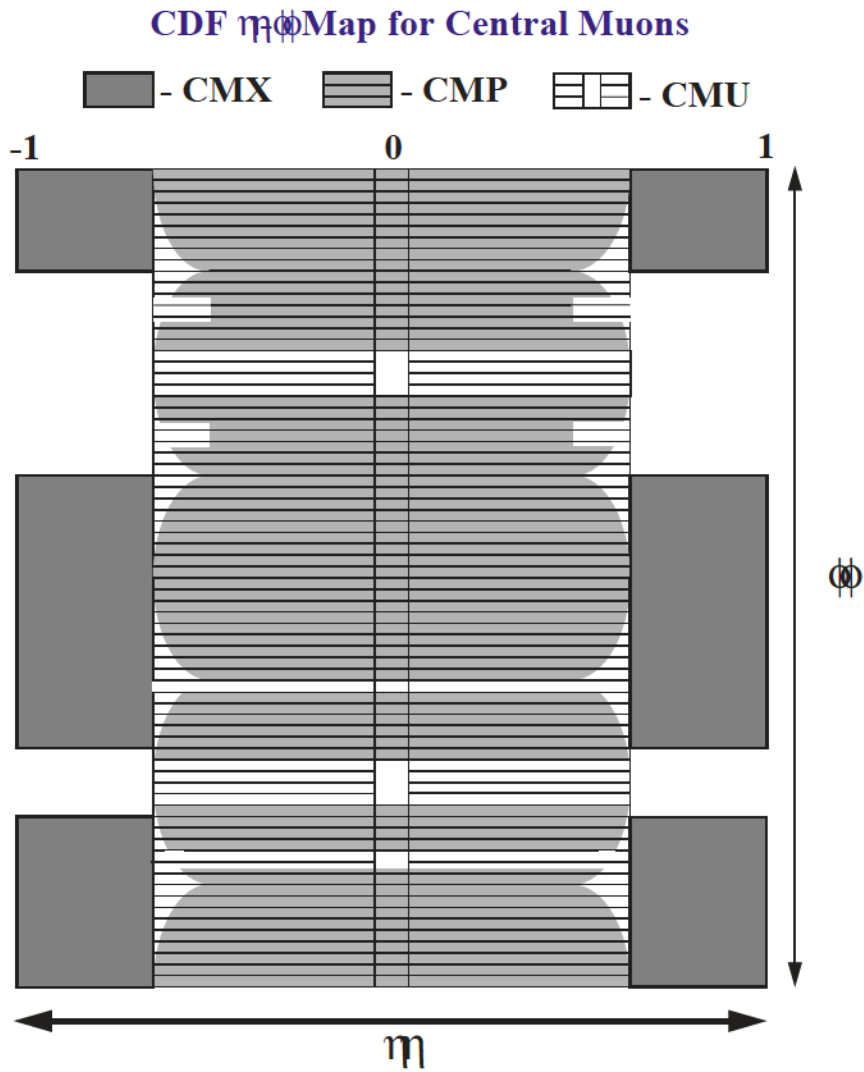
Figure 2.3: Regions in η-ϕ covered by different CDF muon chambers. These are the active regions of the detector where muons can be detected. The muon chamber coverage is not uniform in ϕ because the chambers do not extend all the way in ϕ.

Chapter 3

Data Sample and Cuts

3.1 Run 1A data pre-selection

The Run 1A dimuon data sample corresponds to 18.8 ± 0.7 pb^{-1} of integrated luminosity. The datasets were made by the electroweak group. These datasets were selected either from Stream-A or the express line data which records roughly 20% of all the data that is taken by CDF. The following selection criteria have been applied to the events in the Stream-A dataset to define the "Loose Z" Electroweak (EWK) sample:

The first muon is required to have

- Transverse momentum as measured by the CTC, $P_t > 18$ GeV

- Energy deposited in the Central Electromagnetic Calorimeter, to be less than 2 GeV, consistent with a minimum ionizing particle.

- Energy deposited in the Central Hadron Calorimeter, to be < 6 GeV, also consistent with a minimum ionizing particle.

- A requirement that the extrapolated CTC track match with a stub detected in the Central Muon Chamber (CMU) or in the Central Muon Upgrade (CMP), or in the Central Muon Extension (CMX).

  This track-stub matching is required in the r-ϕ plane.

  For a CMU stub, the track to stub match at the location of the muon chambers, $|dx(CMU)|$, is required to be within 2.5 cm. For a CMP muon, the match, $|dx(CMP)|$, is required to be within 10 cm. For a CMX muon, the requirement is $|dx(CMX)| < 8.$ cm

A second muon is required to have a P_t of at least 15 GeV.

This preliminary sample was selected by Mark Krasberg, et. al., [10] and it contained a total of 5444 events.

3.2   Run 1B data pre-selection

The Run 1B data sample corresponds to 978 good runs taken from Run 55384 (Jan 22, 1994) to Run 70987 (July 22, 1995), with a total integrated luminosity of 89.92 pb^{-1}. Of this a total of 88.57 pb^{-1} of data corresponds to runs which are muon good runs (i.e. had functioning muon chambers).

The Stream-A data sample (also known as the express-line dataset) is used for the Z' search in the dimuon channel.

This sample contains approximately 3.5 million events, which in a smaller pad data format, occupy approximately 30 tapes. Most of these events are not part of the Z' signal, indeed many of these events do not contain a muon. In order to reduce the size of the dataset and select events that are of interest to this analysis, we pre-select events that contain either a dimuon or a dielectron-electron or one muon and one electron candidate. The events must contain at least two objects (ELES or CMUOs or CMIOs) passing the following cuts:

- An electron ELES object with transverse energy in the calorimeter, E_t, measured by the Central Electromagnetic Calorimeter, greater than 15 GeV and a corresponding matching track in the CTC with a P_t greater than 13 GeV

- An electron ELES object with transverse energy in the calorimeter, E_t, measured by the Plug Electromagnetic Calorimeter, greater than 13 GeV

- An electron ELES object with transverse energy, E_t, measured by the Forward Electromagnetic Calorimeter, greater than 10 GeV

- A muon track in the central muon chambers, CMUO, with P_t, (measured by the Central Tracking Chamber), greater than 15 GeV

- A muon candidate as defined by a minimum ionizing signal in the electromagnetic and hadronic calorimeters, CMIO with P_t, (measured by the Central Tracking Chamber), greater than 15 GeV

Since muon CMIOs do not require a matching stub in the muon chambers,this

analysis requires that a CMIO come in pair with a CMUO or ELES. This means, of course, that events that have two CMIOs, but no ELES or CMUO passing the above requirements are not accepted into the preliminary data sample. This preliminary data sample consists of approximately 850000 events which is a factor of 4 reduction in the size of the data. This PAD dataset has been copied onto tapes, RK7456 - RK7465. Since there are $e - \mu$ events as well in this sample, it could in principle be used for other searches as well. Pertinent details about this sample are shown below:

Table 3.1: Events filtered from data tapes

FCC Tape ID	Stream A source tape ID	Number of passed events
RK7456	CCK176, CCK213 CCK464, CCM863	118118
RK7457	CCN013, CCP659 CCP802	87923
RK7458	CCK504, CCN537 CCP939, CCQ247	131365
RK7459	CCK935, CCL426, CCL470 CCL507, CCL859, CCP470	146111
RK7460	CCM307, CCM691, CCN368 CCN886	138013
RK7461	CCK239, CCL371, CCL393 CCQ234, CCQ492	104919
RK7462	CCQ922, CCR221, CCR859 CCQ951	97634
RK7463	CCR668	33897

In a further level of filtering, only those events that contain a well identified muon detected in the central region of the detector are selected. In order to select this muon, the following selection criteria are used:

- P_t, the transverse momentum of the muon as measured by the Central Tracking

Chamber, larger than 18 GeV

- Energy deposited by the muon in the calorimeters, both the EM and the hadron calorimeter be consistent with its being a minimum ionizing particle:

  CEM energy < 2 GeV

  CHA energy < 6 GeV

- Good spatial match between the extrapolated position of the track and the stub detected in the muon chambers:

  $|dx(CMU)| < 4$ cm, if the muon has a stub in the central muon chambers.

  $|dx(CMP)| < 8$ cm, if the muon has a stub in the central muon upgrade chambers.

  $|dx(CMX)| < 8$ cm, if the muon has a stub in the central muon extension chambers.

- That the muon be well isolated from other jets, and electromagnetic showers in the event.

  The isolation is measured by the variable:

  Isolation $= E_t$(Cone of 0.4) - E_t(muon tower)

  The requirement is that :

  Isolation < 2 GeV

  This means that there be no more than 2 GeV of energy in all the calorimeter towers surrounding the muon tower, within an η - ϕ cone of 0.4.

  This cut defines the event topology.

Z (and consequently Z') bosons are expected to decay into isolated dimuons.

Therefore the isolation cut is used to enrich the sample in Zs.

Any input tapes in the sample that are found to be bad are re-selected and the events added to the search sample. All duplicate events are removed at the final selection.

3.3 Run 1A search sample and selection Cuts

This section gives a brief description of the selection requirements that are used to pre-select a sample of candidate events. Events are required to have two tracks, at least one matching a stub in the fiducial region (i.e. within the active area of the muon chambers) of the central muon detector (CMU, or CMU/CMP). The second track can be fiducial or non-fiducial (outside the active area of the muon chambers but identified as a muon by tracking and calorimetry information) [9]. Non-fiducial muons need not have a matching stub in the central muon chambers (CMU/CMP/CMX). Both tracks are required to be consistent with a minimum ionizing particle in the calorimeter. We select the muons from the sample according to whether they satisfy a series of cuts : *tight* or *loose*. The highest P_t muon that satisfies the *tight* cuts is referred to as the *first* muon. After a muon satisfying the *tight* requirements has been found, another muon satisfying the *loose* cuts is chosen as the *second* muon.

The following is a summary of additional cuts used to select the muons (starting with the data sample from Run 1a or Run 1b) :

- The momentum measured by the CTC, $P_t > 18$ GeV/c. This cut has been already applied in the data sample selected for Run 1b.

- The momentum as measured by the CTC is more accurate if the tracks are beam constrained. The position of the interaction vertex is determined by the VTX (and/or the SVX). The CTC tracks are constrained to originate from their associated Vertex and their relative impact parameter with respect to the beam spot is constrained to be zero.

  After these constraints are applied, the track's curvature is determined, and the momentum is measured from its curvature.

  The momentum measured by the CTC, P_t(beam constrained) > 20 GeV/c. (Note that this cut is not imposed in special cosmic ray rejection studies).

- Muons are minimum ionizing particles. They deposit very little energy in the calorimeters compared to an electron or a hadron.

  EM Energy (energy deposited in EM calorimeter) < 2 GeV

  Had Energy (energy deposited in Had calorimeter)< 6 GeV

- The tracks are also selected so that the unconstrained track is associated with an interaction point, which is a vertex that was found by the VTX. The requirement is:

  $|\Delta(Z_\mu - Z_{vertex})| < 5$ cm, matching between the track Z and the closest vertex from the VTVZ bank

- The Z vertex of the interaction is required to be within the fiducial volume of the detector. $|Z_{vertex}| < 60$ cm, the vertex from the VTVZ bank closest to each muon is required to be within 60 cm of the center of the detector.

In addition the following additional tight cuts are used to select the *first muon*:

- A tight muon is a muon that is detected in the Central Muon detector. This type of muon is associated with stubs confirmation hits in the Central Muon Chambers (CMU) and the Central Muon Upgrade (CMP) , wherever the central muon chambers are covered by the CMP.

- The muon's track, as measured by the CTC, is extrapolated to the position of the muon chambers. The closest stub that matches the track and is consistent with the momentum measured by the CTC is found. For a tight muon, a track stub matching distance perpendicular to radial direction $|dx(CMU)| < 2$ cm is required.

- If the muon traverses through a region of the detector that is covered by the CMP, it is also required that the CTC track extrapolate to a stub in the CMP : $|dx(CMP)| < 5$ cm

- Fiducial requirement: The extrapolated track from the CTC is required to fall within the CMU or both the CMU and the CMP fiducial region, depending on whether there is a hit in the CMU or both the CMU and CMP. This is the same fiducial region that has been used for the analysis of the ratio of W and Z cross sections (R-analysis).

- Isolation (from calorimeter) < 2 GeV

The isolation variable is a measure of the activity in the event. It is defined as

$$Isolation = E_t(0.4) - E_t \qquad (3.3.1)$$

where $E_t(0.4)$ is the energy in a cone of radius 0.4 in $\eta - \phi$ space, and E_t is the transverse energy in the muon tower.

The following additional looser requirement is used to select the *second muon*:

- The muon is not required to match a stub in the central muon detectors.

- If, however, the loose muon does not match a stub, the muon's track is required to have traversed a radial distance of 103.6 cm in the CTC. This corresponds to a well measured track in the CTC.

It is also required that the event pass the level 1, level 2 and level 3 triggers as described in Table 3.2. In Run 1A, the CMUP/CMUNP triggers were separately introduced in the latter half of the run. Note that trigger requirements for Run 1B are different from those in Run 1A.

Table 3.2: List of triggers used for Run 1A data selection

Trigger type	Trigger name
Level 1	CMU_CMP_6PT0[*]
Level 2	CMU_CMP_CFT_9_2[*], CMUNP_CFT_9_2_5DEG
Level 3	MUO2_CMU_AND_CMP_18, MUO2_CMU_18

Tables 3.3 through 3.5 list the number of events that pass each of the above cuts in the Run 1A data sample. The sample of events passing the above described cuts has a

Table 3.3: Number of events passing first muon leg cuts in Run 1A

Type of cut	Number of events passing this cut
Total number of events in sample	5444
$P_t > 18$ GeV/c and CMU/CMP	3449
$P_t > 20$ GeV/c , beam constrained (when beam constraint fails use P_t unconstrained)	2952
CHA energy < 6 GeV	2712
CEM energy < 2 GeV	2693
Track stub match, dx (CMU) < 2 cm	2502
Track stub match, dx (CMP) < 5 cm (when there is a confirmation in CMP)	2157
Track vertex Z match, $|\Delta Z| < 5$ cm	2091
$|Z_{vertex}| < 60$ cm of the center of detector	1979
Track points to fiducial CMU/CMP	1745
Isolation (from calorimeter)< 2 GeV	1235
Second leg $P_t > 18$ GeV (see next table)	1152

total of 806 dimuon events of which 601 are of type CMUO-CMUO, and 205 are CMUO-CMIO. These include events where the muon track could not be beam constrained. The application of the level 1,2 and 3 trigger requirement to these 806 events reduces the sample to 750 events. After removing bad runs, we are left with a sample of 693 events, of which a further 184 events are removed by requiring reasonably well beam constrained track.

With all of the above cuts applied to the data we obtain a total of 509 events. Up to this point the cuts are identical to the cuts used in the R-analysis [9]. The R analysis at this point proceeds to apply the opposite charge requirement, the mass requirement in the Z region, and the standard cosmic ray filter rejection (CMCOS). For the Z' analysis the above three cuts are not applied. We do not require opposite sign, and we look at all invariant mass regions.

Table 3.4: Number of events passing 2nd leg CMUO cuts in Run 1A

Type of cut	Number of events passing this cut
P_t (CMUO) > 18 GeV/c	708
$P_t > 20$ GeV/c , beam constrained	680
(when beam constraint fails use P_t unconstrained)	
CHA energy < 6 GeV	658
CEM energy < 2 GeV	640
Track vertex Z match, $|\Delta Z| < 5$ cm	611
$|Z_{vertex}| < 60$ cm of the center of detector	601

Table 3.5: Number of events passing 2nd leg CMIO cuts in Run 1A

Type of cut	Number of events passing this cut
P_t (CMUO) > 18 GeV/c	444
$P_t > 20$ GeV/c , beam constrained	396
(when beam constraint fails use P_t unconstrained)	
CHA energy < 6 GeV	349
CEM energy < 2 GeV	333
Track vertex Z match, $|\Delta Z| < 5$ cm	313
$|Z_{vertex}| < 60$ cm of the center of detector	307
CTC exit radius> 103.6 cm	205

3.4   Run 1B search sample and selection cuts

After the preselection, standard Z' selection cuts are applied to the run 1B data sample.

The pre-selected input sample for run 1B consists of a total of 18291 events.

The Run 1B analysis incorporates additional cuts as follows:

- The tracks are required to be well measured by the CTC, i.e. the fractional error

  in the measurement of the curvature be less than 30%.

  $$\frac{\delta curv}{curv} < 0.3$$

  This is introduced to reduce the background of fake tracks during the period of

high luminosity running of the Tevatron in run 1B.

- The tracks of both the muons are required to extrapolate to within 10 cm of each other,

$$|Z_\mu^1 - Z_\mu^2| < 10 \text{ cm}$$

The tracks of the muon are required to originate close to each other, as they should if they come from the decay of a single particle. This cut reduces backgrounds from cosmic rays and from fake tracks.

Table 3.6: Number of events passing first muon leg cuts in Run 1B

Type of cut	Run 1B
Total number of events in sample	18291
$P_t > 18$ GeV/c and CMU/CMP	11570
$P_t > 20$ GeV/c , beam constrained	11315
(when beam constraint fails use P_t unconstrained)	
CHA energy < 6 GeV	11201
CEM energy < 2 GeV	10708
Track stub match, dx (CMU) < 2 cm	10666
Track stub match, dx (CMP) < 5 cm	10228
(when there is a confirmation in CMP)	
Track vertex Z match, $|\Delta Z| < 5$ cm	9504
$|Z_{vertex}| < 60$ cm of the center of detector	8112
Track points to fiducial CMU/CMP	
Isolation (from calorimeter)< 2 GeV	7870
Second leg $P_t > 18$ GeV (see next table)	7112

Tables 3.6 through 3.8 list the number of events that pass each of the above cuts in the Run 1B data. In run 1B, the sample of events passing the above described cuts consists of a total of 5014 dimuon events of which 3716 are of type CMUO-CMUO, and 1298 are CMUO-CMIO. These include events where the muon track could not be beam constrained.

Table 3.7: Number of events passing 2nd leg CMUO cuts in Run 1B

Type of cut	Run 1B
P_t (CMUO) > 18 GeV/c	4607
$P_t > 20$ GeV/c , beam constrained (when beam constraint fails use P_t unconstrained)	4397
CHA energy < 6 GeV	4237
CEM energy < 2 GeV	4110
Track vertex Z match, $|\Delta Z| < 5$ cm	3811
$|Z_{vertex}| < 60$ cm of the center of detector	3716

Table 3.8: Number of events passing 2nd leg CMIO cuts in Run 1B

Type of cut	Run 1B
P_t (CMUO) > 18 GeV/c	2505
$P_t > 20$ GeV/c , beam constrained (when beam constraint fails use P_t unconstrained)	2220
CHA energy < 6 GeV	1957
CEM energy < 2 GeV	1820
Track vertex Z match, $|\Delta Z| < 5$ cm	1694
$|Z_{vertex}| < 60$ cm of the center of detector	1668
CTC exit radius> 102.7 cm	1298

The total number of events in the Z-mass region (66 GeV-116 GeV) is 1948 events.

Table 3.9: Number of events passing final cuts in Run 1B

Type of cut	Run 1B
Total number in sample	5014
Remove duplicate events	4913
Require Lvl 1, Lvl 2, Lvl 3 trigger	4069
CTC exit radius> 103.6 cm	4052
Require vertex Z match, $\|Z_\mu^1 - Z_\mu^2\| < 10$ cm	3739
Require that both legs satisfy beam constraint	2577
Require good tracks, $\frac{\delta curv}{curv} < 0.3$	2474
Z' Cosmic Ray filter	2218
Badrun removal	2122
Total number of events above 50 GeV	2062
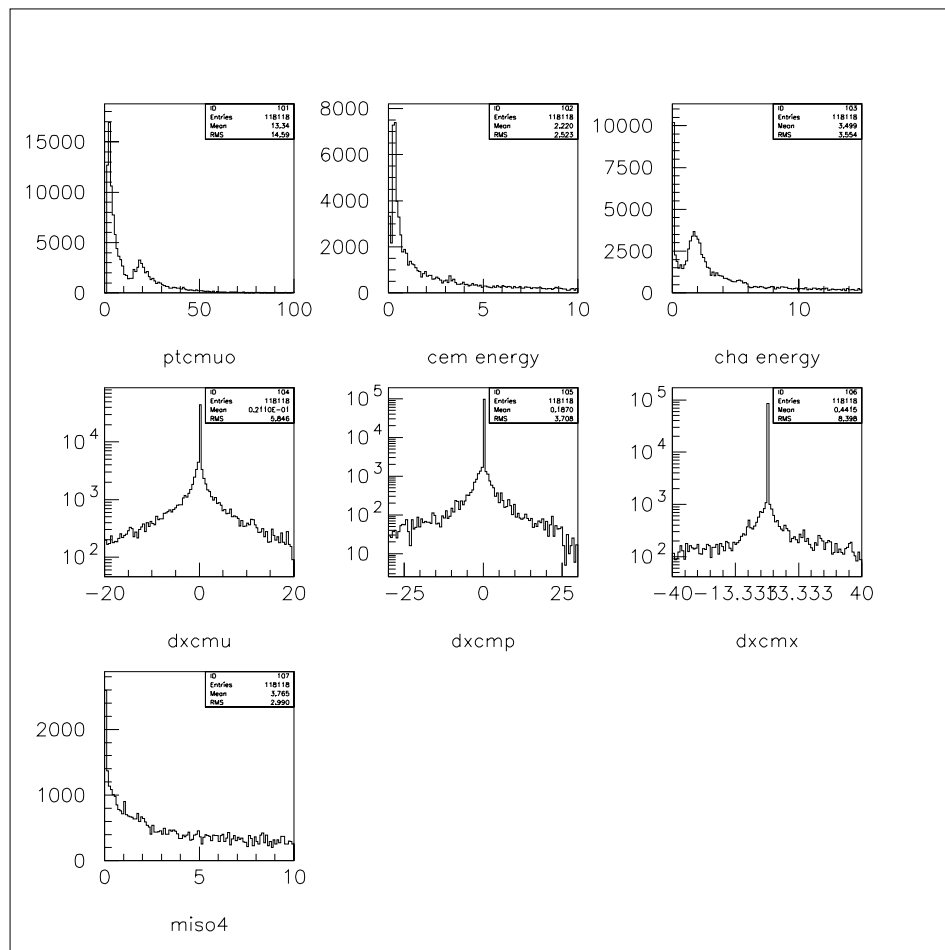
Figure 3.1: The distribution of variables for events in the sample in tape rk7456. Duplicate events coming from same files have been removed by running on the tapes properly.

Chapter 4

Cosmic Rays

4.1 Brief Overview

Cosmic Rays consist of streams of high energy particles and radiation that originate in outer space, possibly from both galactic extragalactic sources. These particles hit the upper atmosphere and generate copious quantities of high energy muons, which are highly penetrating.

Unless removed, cosmic ray muons can be a major source of background to this analysis as they can mimic dimuon events. A single cosmic-ray muon going through our detector can reconstruct to appear as a pair of back-to-back tracks in the Central Tracking Chamber (CTC). For a Z' event, there would be two distinct muons, which would reconstruct to form two back-to-back tracks in the CTC. In this section we briefly outline the strategy we use to discriminate between such events and the background from cosmic-rays.

- Cosmic Ray muons pass from the top of the detector towards the bottom, as

opposed to collider events, where dimuons are produced in the center of the detector. The time required for a cosmic ray muon to traverse the detector from top to bottom is:

$$\Delta_T = T_{top} - T_{bot}$$
$$= (L_1 + L_2)/c$$
$$\approx 2L/c$$

where L_1 and L_2 are the distances traversed by the cosmic ray in the top and the bottom sections of the detector. We approximate the velocity of the muon with the velocity of light as we are interested in very high energy muons ($P_t >$ 20 GeV)[1].

For a Z' event, the relation is, of course, quite different.

$$\Delta_T = T_{top} - T_{bot}$$
$$= (L_1 - L_2)/c$$
$$\approx 0$$

where L_1 and L_2 are the distances traversed by the muons in the top and the bottom sections of the detector, and are assumed to be approximately equal for a good event.

---

[1] For these high momenta the difference between the velocity of the muons and the speed of light is less than 10^{-3}

Therefore, the times at which the particles associated with a track enter and exit the detector can be used to discriminate between real events and cosmic rays. The resolution of the detector for these cosmic rays is approximately

- Another characteristic of cosmic ray muons is that the tracks are spatially back-to-back, when compared to Z' events. However, for very massive Z's, the muons also tend to be emitted back-to-back and therefore, a selection that took advantage of this parameter would be inefficient.

- Cosmic ray muons are uncorrelated with the position of the interaction vertex or the timing of interactions within the detector. If they do not arrive in time with an event the tracks do not get properly reconstructed by the CTC. For the small fraction of Cosmic Rays which get reconstructed, the tracks do not necessarily come close to an interaction $Vertex$ or to the position of the beam. Thus the requirement that the muon tracks be constrained to the beam position eliminates a major fraction of the background.

In this analysis, we need to define a set of analysis criteria that will eliminate these background events, but at the same time not have a major effect on the acceptance of our detector for detecting real Z' events.

Furthermore, we need to estimate the cosmic ray background that remains in the sample after all the analysis criteria have been applied.

To do both of these at the same time, we adopt the following strategy:

We design two sets of cosmic ray cuts, using *uncorrelated* physical measurements (the timing of the tracks and the spatial back-to-back nature of the tracks). We then *calibrate*

these cuts against each other. Once we optimize the efficiency of these cuts, we use the measured inefficiency of the cuts with the *known* estimate of cosmic ray events in the sample (that are rejected by our cuts) to estimate the contamination that remains *after* the cuts have been applied.

4.2 Cosmic Ray Rejection

We describe the two independent cuts designed to reject cosmic rays. The first cut is a back-to-back $\eta - \phi$ veto cut similar to the cut used in the 88-89 dimuon analysis [11]. The second cut is a cosmic ray rejection cut based on the Hadron Calorimeter Time to Digital Converter (Hadron TDC) information. Since the two cuts are uncorrelated we can use one to study the efficiency of the other. In the next section we describe cosmic ray rejection cuts based on a combination of both the Hadron TDC information and the back-to-back $\eta - \phi$ tracking cut veto.

4.2.1 Back-to-back veto

The *nominal* 88/89 back-to-back veto was defined as follows:

$|\eta_{b-b}| < 0.2$ and $|\phi_{b-b}| < 0.035$,

where we used beam unconstrained variables defined by,

$\eta_{b-b} = \eta_1 + \eta_2$

$\phi_{b-b} = \pi - |\phi_1 - \phi_2|$

where η_1, η_2 are defined as the η of each track,

$\eta = -ln[tan(\frac{\theta}{2})]$, and θ, the polar angle of the track. ϕ_1, ϕ_2 are defined as the azimuthal angle of the tracks.

In addition to above *nominal* 88/89 back-to-back veto, we introduce a *narrow* back-to-back veto cut ($|\eta_{b-b}| < 0.1$ and $|\phi_{b-b}| < 0.0175$), which is the primary veto used in this analysis. This veto has a higher geometrical acceptance for Z' events than the *nominal* 88/89 back-to-back veto. We can use this higher acceptance cut (veto) because in addition to the back-to-back veto we use cuts based on information from the Hadron TDCs. As a check we also studied a *wide* back-to-back veto ($|\eta_{b-b}| < 0.4$ and $|\phi_{b-b}| < 0.07$).

Figure 4.1 shows the η - ϕ distribution of muons in the Run 1A dimuon sample before the application any cosmic rejection cuts. The hatched events are those for which the Δ_{TDC} information (as described below) indicates that the events are out of time and consistent with being cosmic rays. It is clear that there is an excess of events at small $|\eta_{b-b}|$ and at small $|\phi_{b-b}|$ in the dimuon channel. Also shown in the figure (hatched) are the events which are identified as cosmic rays by the hadron TDC's. The excess at small $|\eta_{b-b}|$ and at small $|\phi_{b-b}|$ corresponds to cosmic rays and the hatched events show that they are also out of time. Figure 4.2 shows the same distributions for dielectrons from Z's and Drell-Yan events in Run 1A. As expected, no excess of events at small $|\eta_{b-b}|$ and $|\phi_{b-b}|$, is observed in the dielectron sample.

4.2.2   Hadron TDC cuts

The Hadron TDCs determine the time for particles traversing the Hadron Calorimeter. The TDCs are started by a beam-beam interaction and are stopped by the pulse coming out of the Hadron Calorimeter. When a particle deposits energy in the Hadron Calorimeter, the time elapsed between the electronic pulse corresponding to the energy
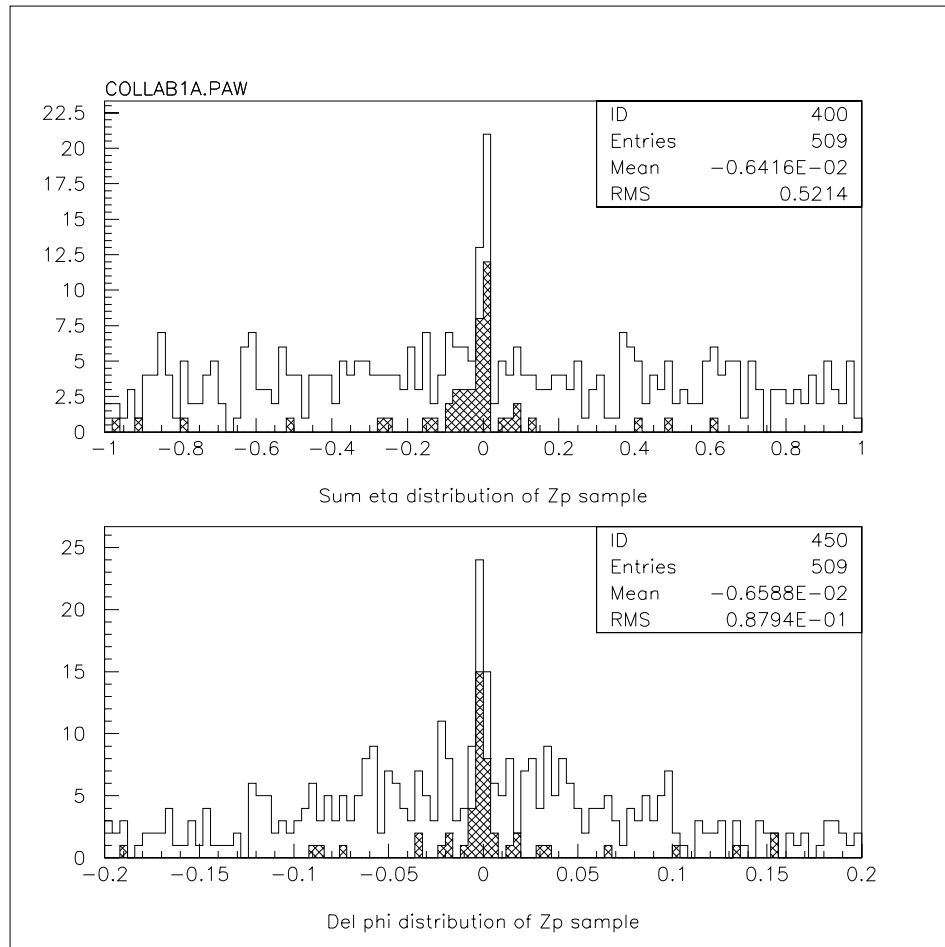
Figure 4.1: The distribution of muons in back-to-back η and ϕ, before the application of cosmic ray rejection cuts in Run 1A. The hatched events are flagged as cosmic ray by the $\Delta_{TDC} <$ -10 nsec cut . Note the peak at $|\eta_{b-b}| < 0.2$ and $|\phi_{b-b}| < 0.035$ originating from from cosmic ray muons.
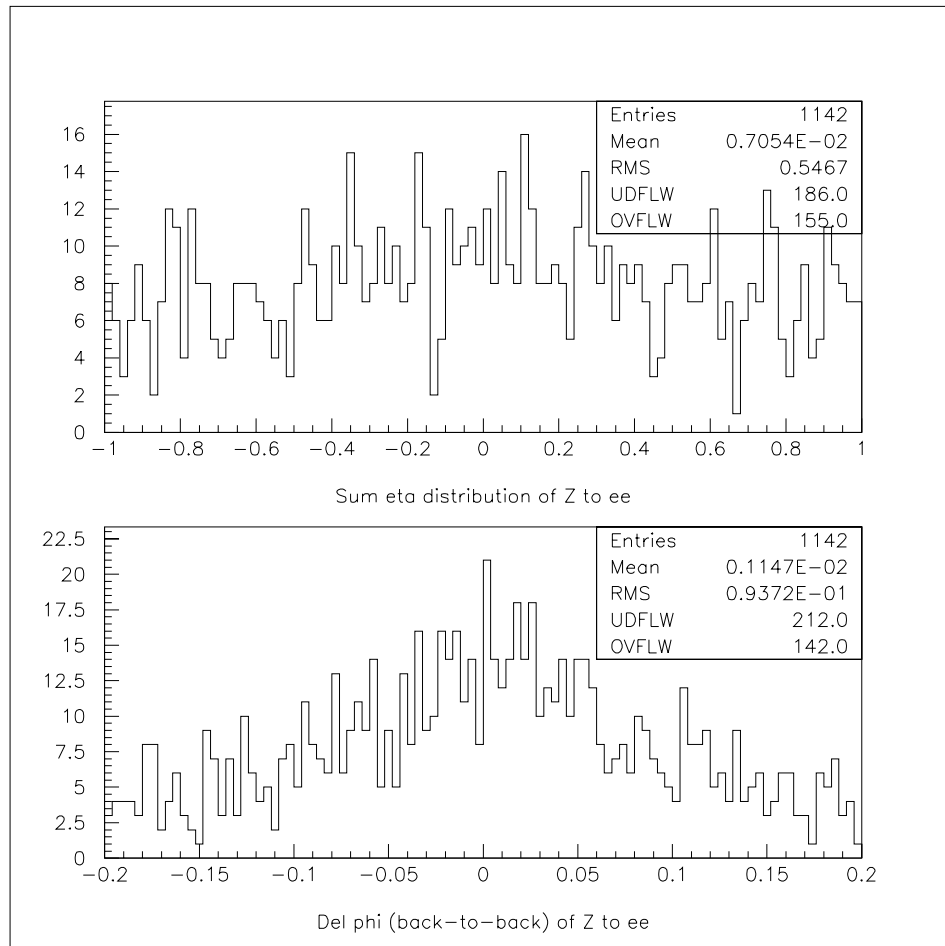
Figure 4.2: The distribution of Run 1A $Z \rightarrow ee$ events. the upper plot shows the sum η distribution η_{b-b} and the lower one the difference ϕ distribution ϕ_{b-b}. Note that there is no peak at $|\eta_{b-b}| < 0.2$ and $|\phi_{b-b}| < 0.035$.

deposition in the Hadron Calorimeter and the beam-beam crossing is thus recorded by the Hadron TDC. We use the Hadron TDC information from the Central Muon (CMUO) data bank. The Hadron TDC cuts are defined as follows. First, we look if there is Hadron TDC information for both muons. Hadron TDC data with very large and negative values, or with values equal zero are not used (these are indicative of hardware failures or counter inefficiency). Next, we form the difference between the Hadron TDC on the top and the Hadron TDC on the bottom.

$$\Delta_{TDC} = TDC_{top} - TDC_{bot} \qquad (4.2.1)$$

For dimuons originating from proton-antiproton collisions, the difference Δ_{TDC} is peaked at zero. Cosmic rays pass a TOP hadron calorimeter tower first, and then a BOTTOM hadron calorimeter tower. Therefore, one expects that on average the difference in time Δ_{TDC} should be peaked at $\approx$ - 20 nsec.

Table 4.1: Number of events with TDC information for Run 1A and Run 1B

Type of cut	$\eta - \phi_{veto}$	$1A_{events}$	$1A_{M>200}$	$1B_{events}$	$1B_{M>200}$
All Events	see below	509	10	2347	11
Both TDCs (category I)	$|\eta_{b-b}| < 0.1$ and $|\phi_{b-b}| < 0.0175$	450 88.4%	10 100%	2087 88.9%	10 90.9%
Top TDC only (category II)	$|\eta_{b-b}| < 0.2$ and $|\phi_{b-b}| < 0.035$	19 3.7%	0 0.0%	115 4.9%	0 0.0%
Bottom TDC only (category II)	$|\eta_{b-b}| < 0.2$ and $|\phi_{b-b}| < 0.035$	37 7.3%	0 0.0%	145 6.2%	1 9.1%
No TDC information (category II)	$|\eta_{b-b}| < 0.2$ and $|\phi_{b-b}| < 0.035$	3 0.6%	0 0.0%	0 0.0%	0 0.0%

4.2.3   Combined hadron TDC and back-to-back veto

We use a cosmic ray veto which is a combination of back-to-back veto and the hadron TDC cuts as described below.

We separate the data into two categories. The first category are events (88.4±1.4% of events in run 1A) in which TDC information is available for both muons. Here we reject events with $\Delta_{TDC} < -10$ nsec, and in addition, we reject events where the *absolute* value of the Hadron TDC information for either top, or bottom TDC are outside ± 14 nsec of the mean TDC values for in time events (+2 nsec for Run 1A, and +6 nsec for Run 1B). A detailed study of the Hadron TDC's for Z events versus cosmic ray events is described in subsection 4.3.

For category I events, after the application of the TDC cosmic ray removal cuts on both the absolute TDC values and on the Δ_{TDC} difference, we then remove any event which satisfy the *narrow* back-to-back cosmic ray veto.

The second category of events are events where there is only TDC information for one muon(11.5 ± 1.4% of events) , or no TDC information at all (0.6% of events). Here, when there is TDC information for one muon, we reject events in which the *absolute* value of the Hadron TDC data for either top, or bottom TDC are outside ± 14 nsec of the mean TDC values for in time events (+2 nsec for Run 1A, and +6 nsec for Run 1B). A more detailed study of this category of events is given in the next section (3.2). For category II events, after the application of the TDC cosmic ray removal cuts on the absolute values of the individual TDC data, we then remove any event which satisfy the *nominal* 88/89 back-to-back cosmic ray veto. Table 4.1 summarizes the number

of events according to the availability of the Hadron TDC information for each of the muons for the Run 1A data and for a 90 pb^{-1} sample of Run 1B.

Figure 4.3a shows the mass distribution of the 509 events for dimuons with invariant masses above 50 GeV/c^2, before the application of cosmic ray rejection cuts. Figure 4.3b shows that for the 450 events where both Hadron TDC information is available, there is a peak near $\Delta_{TDC} \approx$ 0 nsec, for proton-antiproton collision events, and a peak at $\Delta_{TDC} \approx$ - 20 nsec for cosmic ray events. We therefore reject events for which Δ_{TDC} is defined and have Δ_{TDC} less than -10 nsec. These events are marked in the hatched region of both the top and bottom plot. The light hatched events on the top plot are flagged as cosmic rays by the absolute timing TDC cut. Out of 10 events with invariant mass above 200 GeV/c^2, only one has Δ_{TDC} consistent with events originating from proton-antiproton collisions.

After the application of the Δ_{TDC} and absolute timing cosmic ray rejection cuts as described above the number of dimuon events in the Run 1A sample drops from 509 to 454 events. Figure 4.5 shows the mass distribution of those events on a linear scale (top plot), and on a log scale (bottom plot), for dimuons with invariant masses above 50 GeV/c^2. There is only one event above a mass of 200 GeV/c^2. The same plot is also shown for the Run 1B analysis in figure 4.6.

Following the application of the corresponding back-to-back cosmic ray veto, the number of dimuon events in the Run 1A sample drops from 454 to 444 events. Figure 4.7 shows the mass distribution of those events on a linear scale (top plot),and on a log scale (bottom plot), for dimuons with invariant masses above 50 GeV/c^2. The highest invariant mass event in the final Run 1A sample has a mass 206 GeV/c^2. It is an

COLLAB1A.PAW

ID	120
Entries	509
Mean	99.47
RMS	73.02
UDFLW	33.00
OVFLW	0.0000E+00

Invariant mass $\mu - \mu$, no c−ray cut

ID	500
Mean	−1.033
RMS	7.075

Difference in Hadtdc timing
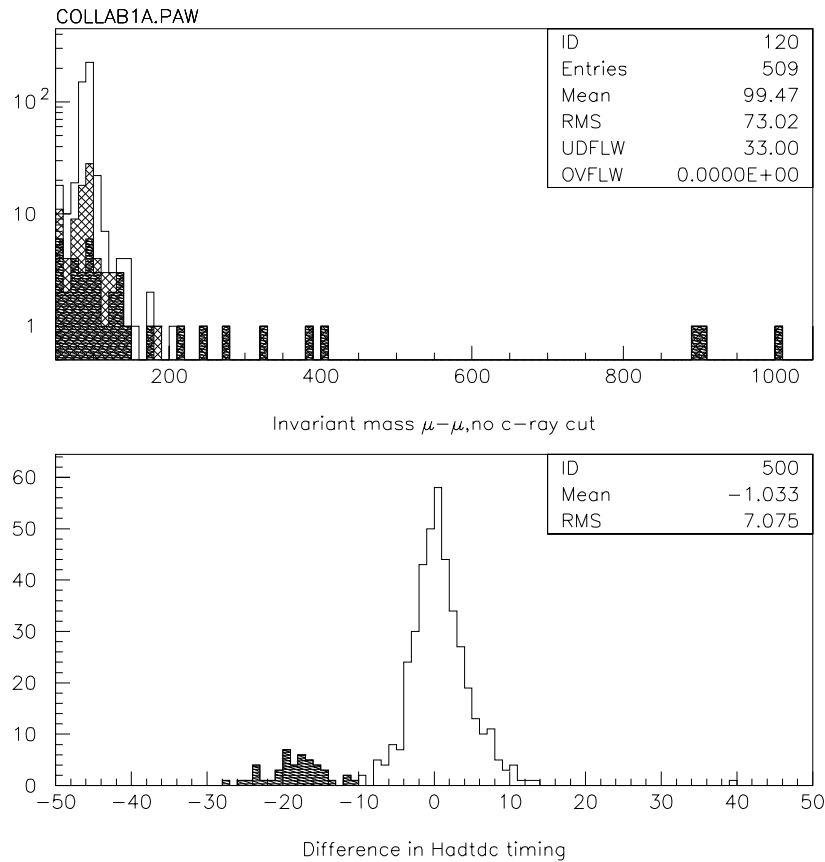
Figure 4.3: a) The Invariant Mass distribution of dimuons for Run 1A before any cosmic ray rejection cuts were applied. b) The difference in the Hadron TDCs between the top and bottom muon(in nsec). In this plot we have not applied any cosmic ray cuts. The peak at zero time difference is from events originating from proton-antiproton collisions. The peak at -20 nsec is from cosmic ray muons. There are 10 events above a mass of 200 GeV/c^2. The dark hatched events on the plots are events which are flagged as cosmic ray by the $\Delta_{TDC} <$ -10 nsec cut. The light hatched events on the top plot are flagged as cosmic rays by the absolute timing TDC cut.
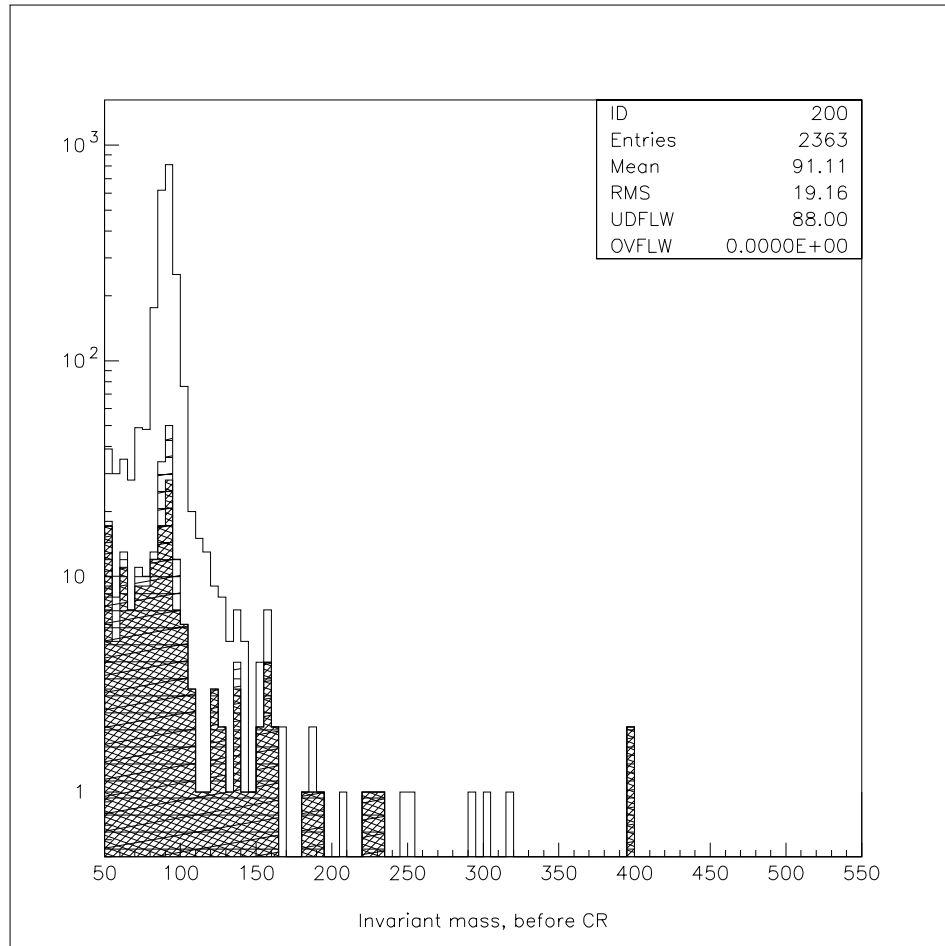
Figure 4.4: The Invariant Mass distribution of dimuons for Run 1B before any cosmic ray rejection cuts were applied. There are 10 events above a mass of 200 GeV/c². The dark hatched events on the plot are events which are flagged as cosmic ray by the $\Delta_{TDC} < $ -10 nsec cut. The light hatched events on the plot are flagged as cosmic rays by the absolute timing TDC cut.

a) histogram with statistics box:

Entries	454
Mean	91.24
RMS	13.32
UDFLW	23.00
OVFLW	0.0000E+00
ALLCHAN	431.0

Invariant mass $\mu-\mu$ hadtdc

b) histogram with statistics box:

Entries	454
Mean	91.24
RMS	13.32
UDFLW	23.00
OVFLW	0.0000E+00
ALLCHAN	431.0

Invariant mass $\mu-\mu$ hadtdc
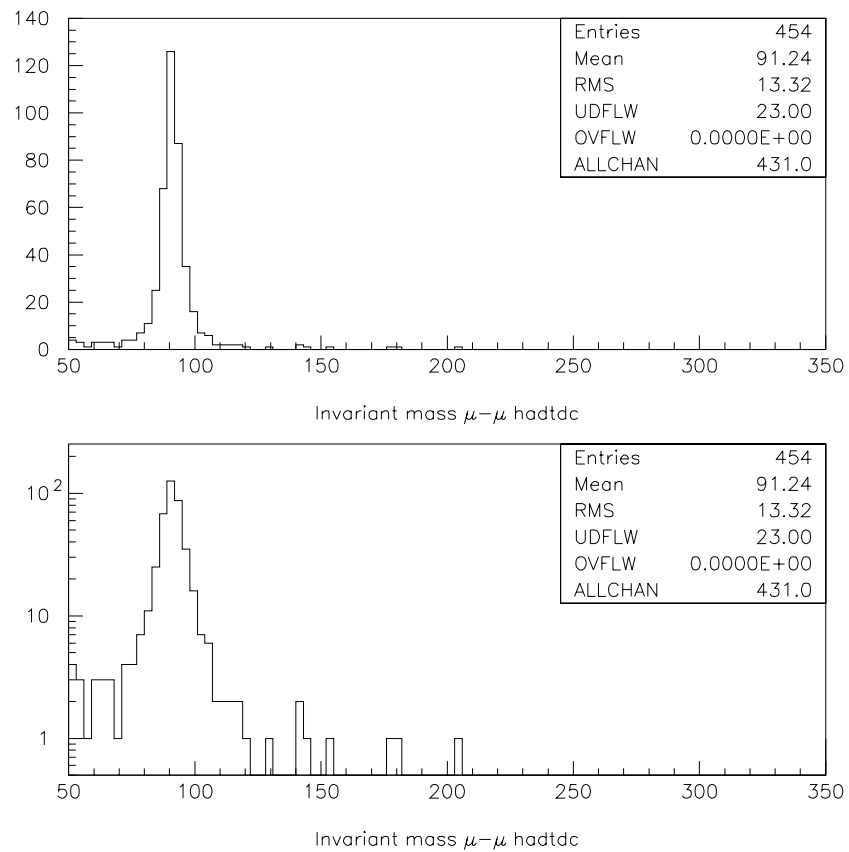
Figure 4.5: a) The invariant mass distribution of dimuons for Run 1A data. At this stage, cosmic rays are removed by a timing cuts on the Hadron TDCs only.

b) The same data in Log-scale. There is only one event with mass above 200 GeV/c^2.
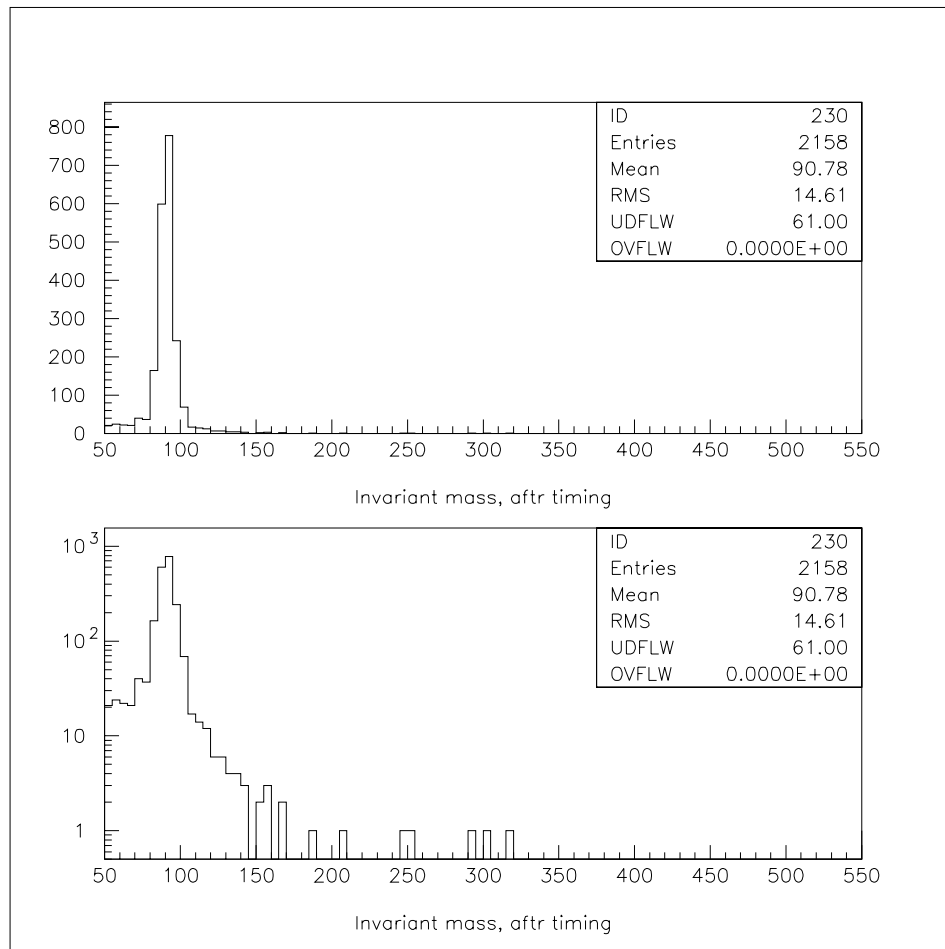
Figure 4.6: a) The invariant mass distribution of dimuons for Run 1B data. At this stage, cosmic rays are removed by a timing cuts on the Hadron TDCs only.

b) The same data in Log-scale. There are six events with mass above 200 GeV/c^2.

opposite sign event, with TDC(top)=6.9 nsec and TDC(bottom)=2.7 nsec. Its back-to-back variables are $\eta_{b-b} = 0.6$ and $\phi_{b-b} = 0.0022$.

4.3   A study of individual TDC information for Run 1A and 1B

The use of the difference between the top and bottom TDC eliminates the sensitivity to changes in the overall common start time of the TDC's. This common start time can vary for different runs. For example it is different in runs 1A and 1B. However, the individual TDC information are useful as well, and they are especially helpful when TDC information is only available for one of the muons in a dimuon event.

Figure 4.9 (top) shows the correlation between the top and bottom Hadron TDCs for the selected *enriched* sample of Z dimuon events in Run 1A. The *nominal* 88/89 back-to-back veto was used to remove cosmic rays from the sample. Figure 4.9 (bottom) shows the same correlation plot for a sample of cosmic rays in Run 1A.

Figure 4.10 (top) shows the correlation between the top and bottom Hadron TDCs for the selected *enriched* sample of Z dimuon events in Run 1B. Figure 4.10 (bottom) shows the same correlation plot for a sample of cosmic rays in Run 1B.

The top plots of Figure 4.11 show distributions of the top and bottom Hadron TDCs for *enriched* (*nominal* 88/89 back-to-back veto was used to eliminate cosmic rays) *Z* events for Run 1A. For events in Run 1A, the individual TDC values peak around + 2 nsec. The two plots on the bottom show the distributions of top and bottom TDCs for a sample of cosmic rays in Run 1A. We reject as cosmic rays any event in which the
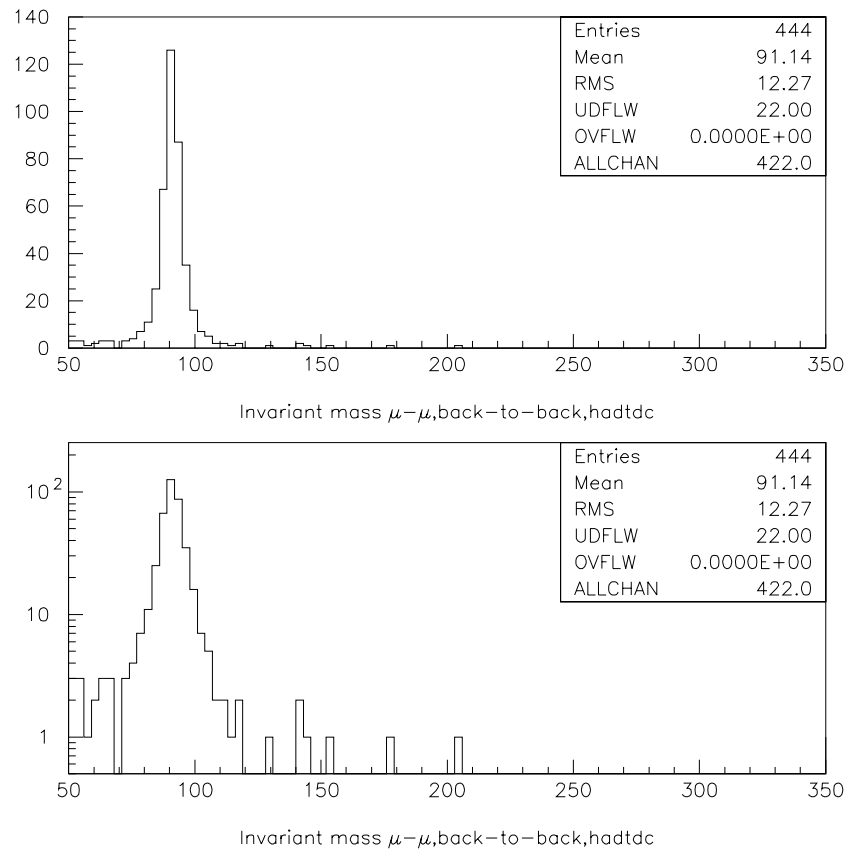
Figure 4.7: a) The Invariant Mass distribution of dimuons for the 18.8 pb^{-1} of Run 1A data. All the events in the final Run 1A sample above an invariant mass of 30 GeV are opposite sign dimuons.

b) The same data in Log-scale. Cosmic rays are removed by applying the Hadron TDC timing cut, and in addition the back-to-back η-ϕ veto. There is only 1 event above a mass of 200 GeV/c^2.
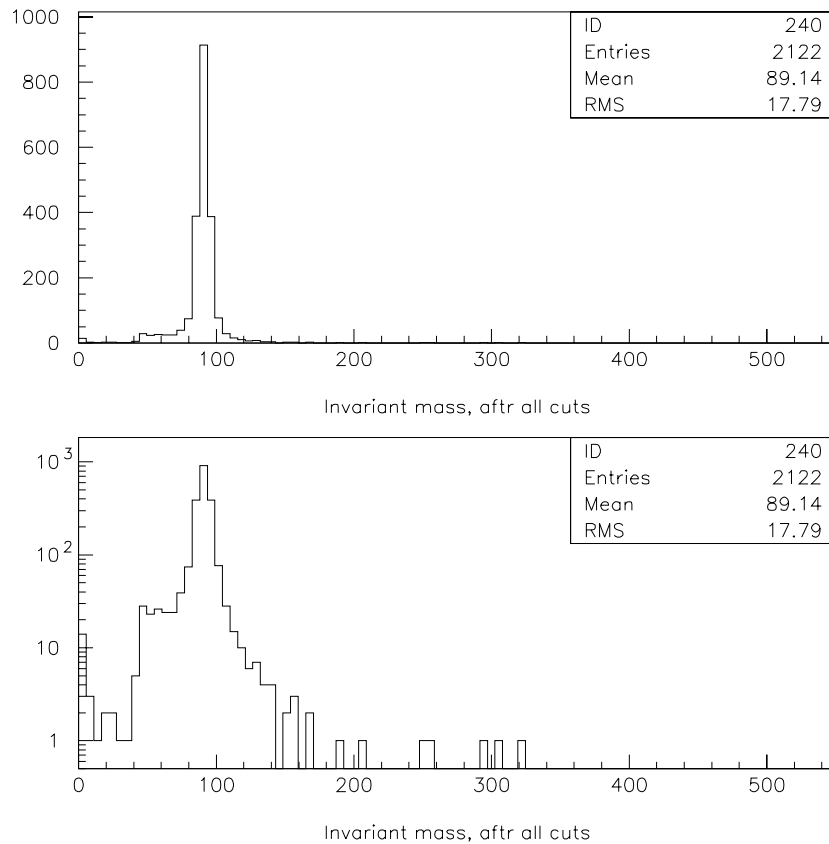
Figure 4.8: a) The Invariant Mass distribution of dimuons for the 88.6 pb^{-1} of Run 1B data. There is 1 event above an invariant mass of 50 GeV that has same sign dimuons. This gives us an estimate of the background.

b) The same data in Log-scale. Cosmic rays are removed by applying the Hadron TDC timing cut, and in addition the back-to-back η-ϕ veto. There are 2 events above a mass of 300 GeV/c^2.

values of the Hadron TDCs are less than -12 nsec or greater than +16 nsec.

The top plots of Figure 4.12 show distributions of the top and bottom Hadron TDCs for an *enriched* sample of Z events (*nominal* 88/89 back-to-back veto was used to eliminate cosmic rays) for Run 1B. For events in Run 1B, the individual TDC values peak around + 6.4 nsec. The two plots on the bottom show the distributions of top and bottom TDCs for a sample of cosmic rays in Run 1B. We reject as cosmic rays any event in which the values of the Hadron TDCs are less than -8 nsec or greater than +20 nsec.

A summary of the efficiencies of these TDC requirements in the rejection of cosmic ray events, and the resulting inefficiencies in the selection of *enriched* Z events (*nominal* 88/89 back-to-back veto used to eliminate cosmic rays) is given in Table 4.3.

The three following sections are organized as follows. First we estimate the inefficiencies for genuine Z' events resulting from the cuts rejecting cosmic rays. This calculation is done using a Monte Carlo simulation (for back-to-back veto cuts) and using Z sample (for timing cuts). Next, we estimate the efficiency of rejection of cosmic ray events using an enhanced sample of cosmic ray muons. Finally we calculate the cosmic ray contamination in the high mass dimuon sample.

4.4 Inefficiencies for selection of Z' events

4.4.1 Inefficiency of back-to-back veto cuts

We use a Monte Carlo simulation [14] to calculate the fraction of Z' events not accepted by different back-to-back veto cuts. Figure 4.13 shows the fraction of events rejected
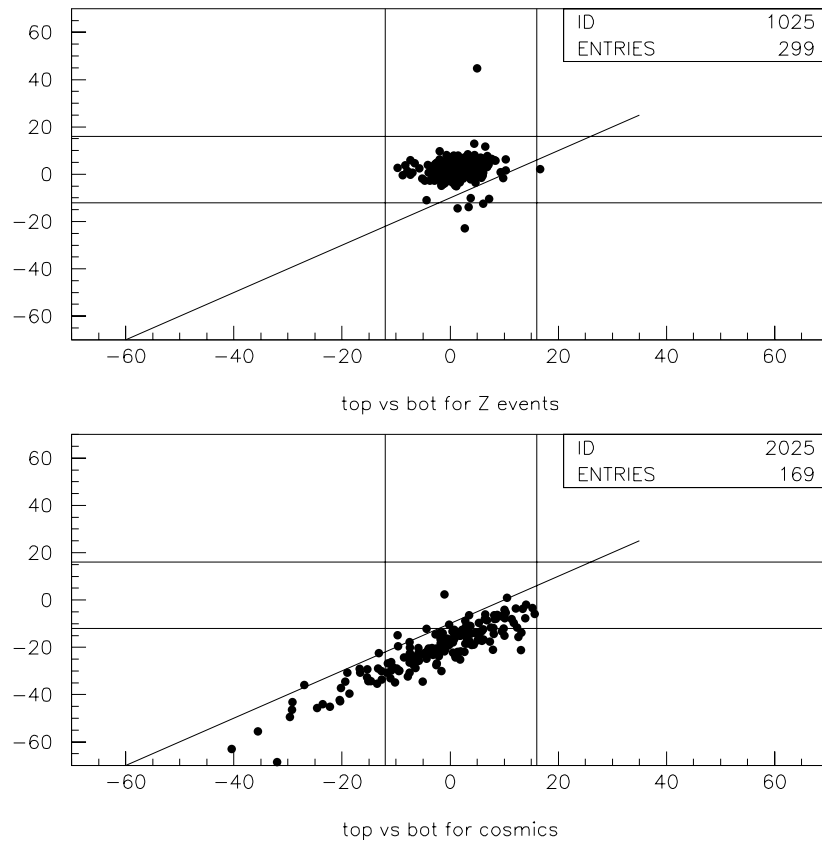
Figure 4.9: Correlation between the top and bottom Hadron TDCs in Run 1A $(18.8\ \mathrm{pb}^{-1})$. Top: Selected Z events. Bottom: Selected sample of cosmic rays. The vertical lines are the cuts applied to the bottom hadron TDC. The horizontal lines are the cuts applied to the top hadron TDC and the diagonal line is $\Delta_{TDC} = $ -10 nsec.
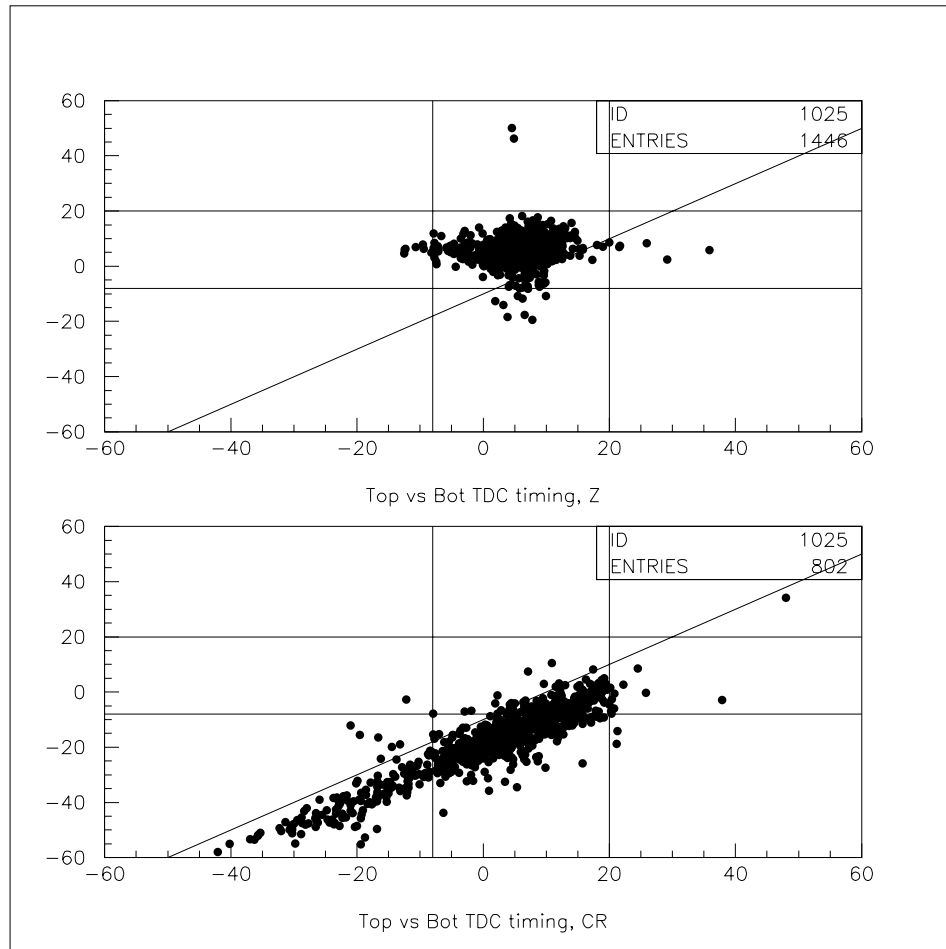
Figure 4.10: Correlation between the top and bottom Hadron TDCs in Run 1B (90 pb^{-1}) data. Top: Selected Z events Bottom: Selected sample of cosmic rays.The vertical lines are the cuts applied to the bottom hadron TDC. The horizontal lines are the cuts applied to the top hadron TDC and the diagonal line is Δ_{TDC} = -10 nsec.
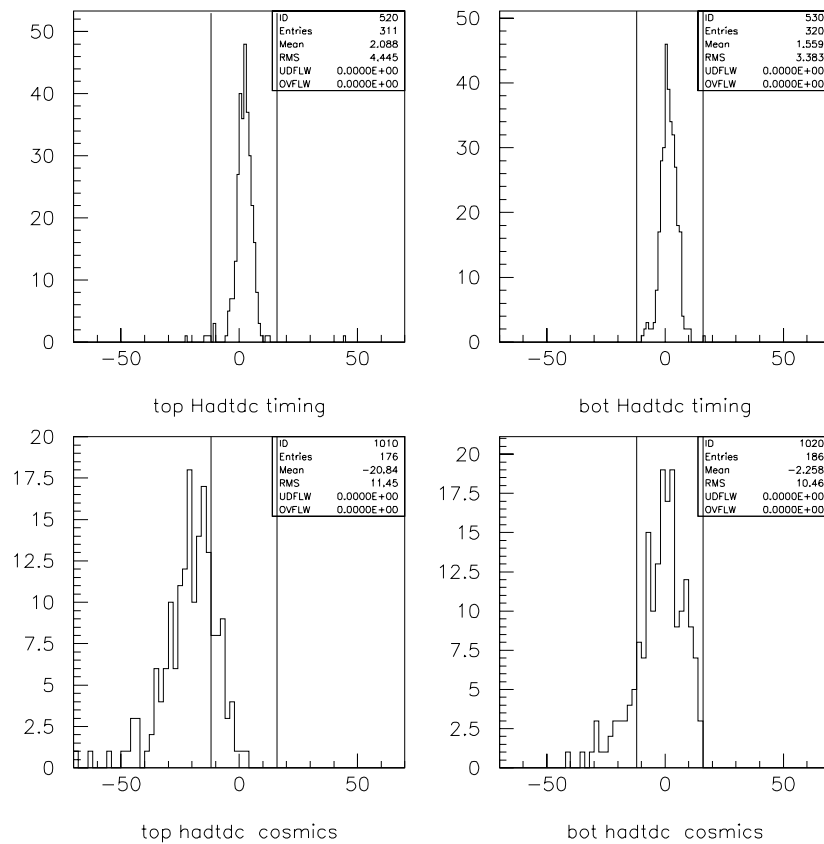
Figure 4.11: Run 1A data (18.8 pb^{-1}): Top: Hadron TDC distributions for top and bottom TDC for *enriched* Z events. Note that the data peak at + 2 nsec. Bottom: The top and bottom TDC distributions for a selected sample of cosmic rays. The vertical lines represent the cuts applied to the TDC's.
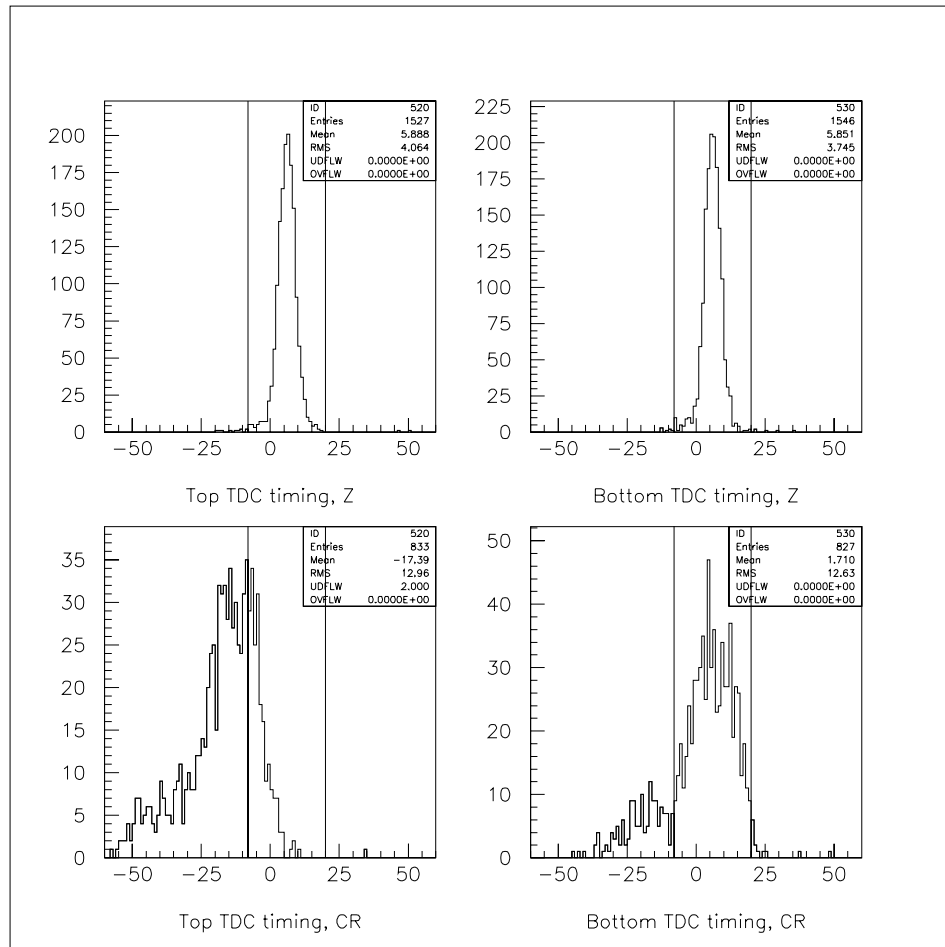
Figure 4.12: Run 1B data (90 pb^{-1}): Top: Hadron TDC distributions for top and bottom TDC for *enriched* Z events. Note that the data peak at + 6.4 nsec. Bottom: The top and bottom TDC distributions for a selected sample of cosmic rays. The vertical lines represent the cuts applied to the TDC's.

by the back-to-back veto cuts as function Z' mass, as determined from Monte Carlo simulation.

As can be seen from the figure, the inefficiency from the *narrow* back-to-back veto cut is approximately 4% for Z' with mass of 550 GeV/c^2. This veto is used for approximately 90% of events, when Hadron TDC information is available for both muons and in this case Δ_{TDC} can be defined. The Monte Carlo simulation also indicates that the inefficiency from the *nominal* 88/89 back-to-back veto is approximately 12% at Z' mass of 550 GeV/c^2 and becomes as large as 20% for Z' mass of 800 GeV/c^2. To avoid this inefficiency in the Z' search, we only use the *nominal* 88/89 back-to-back veto for the small fraction ($\approx 10\%$) of events for which the Hadron TDC information is not available for both muons.

As a check of the efficiency calculation of the back-to-back veto cuts for genuine Z' events, we find that the number of Zs removed by the back-to-back veto in the dielectron channel is compatible with the prediction from the Monte-Carlo simulation. The Monte-Carlo predicts that in the Z region 2.5% $\pm$ 0.5% of the events would be removed from the dielectron data by the *nominal* 88/89 back-to-back veto cut. From the Z $\to$ ee data we obtain an inefficiency of 3.6% $\pm$ 1%, which is consistent with the value from the Monte Carlo simulation.

4.4.2   Inefficiency of Hadron TDC cuts

In order to calculate the inefficiency in Z' selection originating from timing cuts, we turn to the $Z \to \mu\mu$ events. Here an *enriched* sample of Z events is selected by requiring an invariant mass tightly around the Z mass (91 $\pm$ 10 GeV/c^2), and by removing any

Fraction of Z' events removed by back-to-back cut
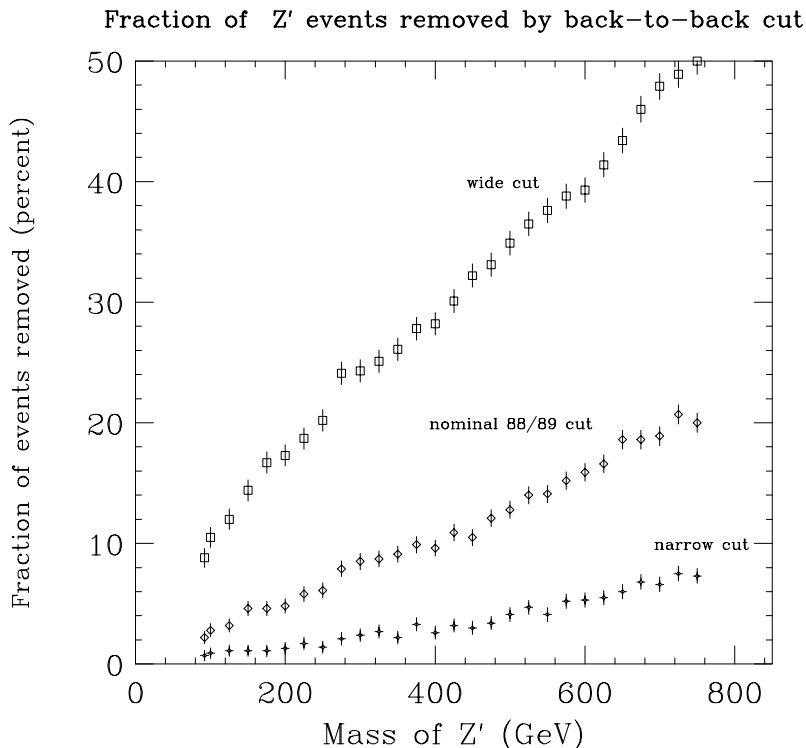
Figure 4.13: The fraction of Z' events that are removed by the cosmic ray back-to-back veto cuts as a function of the Z' mass. *Narrow* veto (star symbols) requires ($|\eta_{b-b}| < 0.1$ and $|\phi_{b-b}| < 0.017$). The *narrow* veto is used when TDC information is available for both muons ($\approx 90\%$ of events). *Nominal* 88/89 veto (diamond symbols) requires ($|\eta_{b-b}| < 0.2$ and $|\phi_{b-b}| < 0.035$), The *nominal* veto is only used when TDC information is not available for both muons ($\approx 10\%$). *Wide* veto (square symbols) requires ($|\eta_{b-b}| < 0.4$ and $|\phi_{b-b}| < 0.07$), The *wide* veto is shown for comparison only and is not used in this analysis. The fractions are determined from a Monte-Carlo simulation.

cosmic rays using the *nominal* 88/89 back-to-back veto. In addition, both muons are required to have opposite charge. Of the sample of 332 Z events, about 90% (299 events) have Hadron TDC information for both muons.

The top part of Figure 4.14 shows the number of events as a function of the difference between the top and bottom Hadron TDCs (Δ_{TDC}) for Z events decaying to dimuons. Of these 299 Z events 8 events or 2.7% $\pm$ 1% of the Z dimuons have an out of time $\Delta_{TDC} <$ -10 nsec. Therefore, when timing information is available for both muons, in time events can be selected with an efficiency of 97.3% $\pm$ 1% using the Δ_{TDC} cut only. The timing requirement is that events with either $\Delta_{TDC} < -10$ nsec or with the value of the individual Hadron TDC outside of the $\pm$ 14 nsec (about the mean value) are removed. We find that timing cuts (Δ_{TDC} and absolute timing cut combined) remove 9 out of 299 events Z events, thus introducing an inefficiency of 3.0% $\pm$ 1.0%.

4.4.3 Combined Inefficiency of cuts for cosmic ray rejection

The inefficiency losses of the combined timing cuts and the *narrow* back-to-back veto are 7% for a Z' mass of 550 GeV/c^2. About 4% of the inefficiency originates from the back-to-back cosmic veto, and 3% originates from the timing cuts. For events for which both TDC information is not available (about 10% of the sample), the inefficiency at a mass of 550 GeV/c^2 is about 13%. Here 12% of the inefficiency originates from the *nominal* 88/89 back-to-back cosmic ray veto, and 1% originates from the timing cuts on a single Hadron TDC. However, as shown in Table 4.1, all of the high mass events in Run 1A, and most of the high mass events in Run 1B, have the Hadron TDC information for both muons.
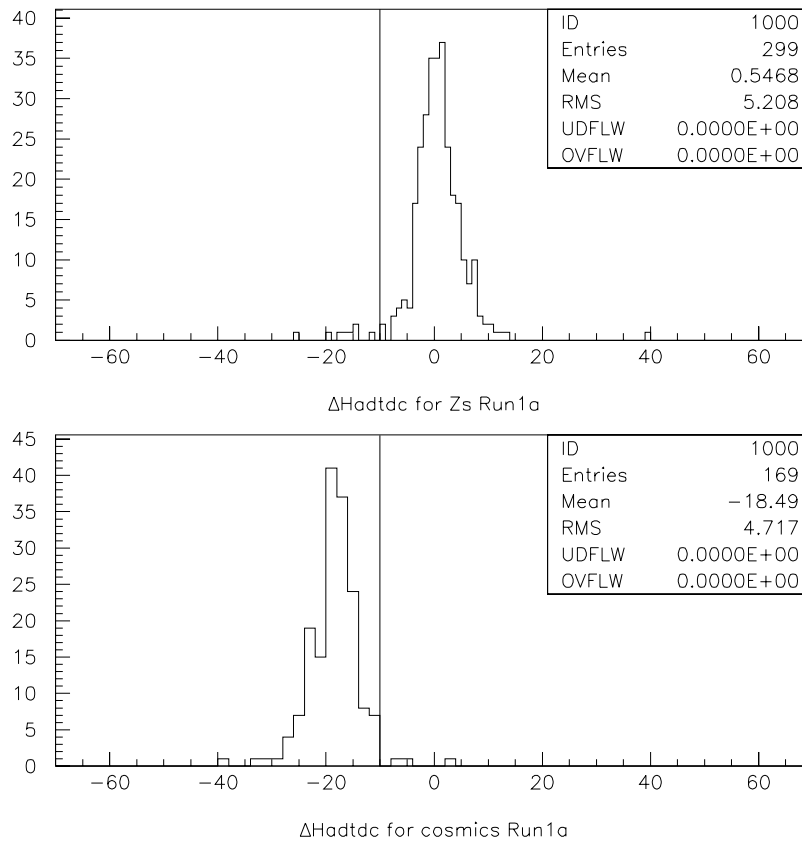
Figure 4.14: Top : The distribution of (Δ_{TDC}) for dimuons from Z's in Run 1A (cosmic rays are removed using the *nominal* 88/89 back-to-back veto). Bottom: The distribution of (Δ_{TDC}) for a cosmic ray muon muon sample selected by a removing the beam constraints in the track fitting, requiring back-to-back geometry, and by removing events in the Z mass peak. The Hadron TDC's cosmic ray rejection cuts removes events with Δ_{TDC} less than -10 nsec.
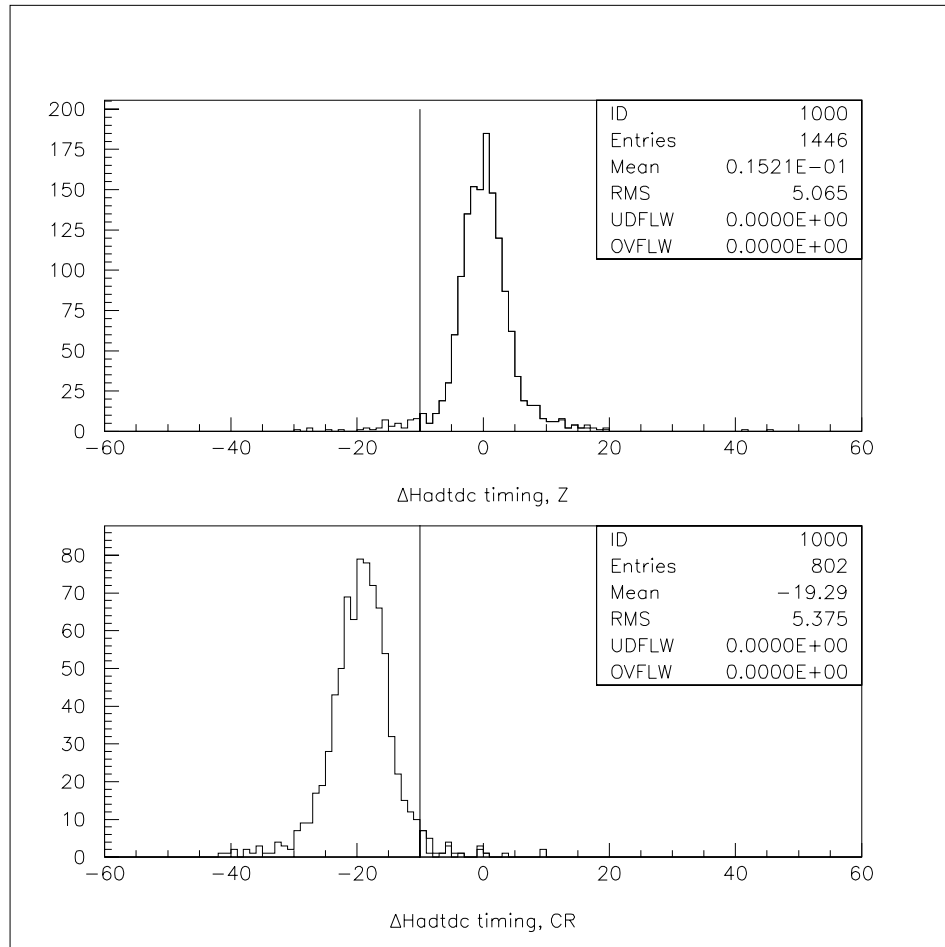
Figure 4.15: Top : The distribution of (Δ_{TDC}) for dimuons from Z's in Run 1B (cosmic rays are removed using the *nominal* 88/89 back-to-back veto). Bottom: The distribution of (Δ_{TDC}) for a cosmic ray muon muon sample selected by a removing the beam constraints in the track fitting, requiring back-to-back geometry, and by removing events in the Z mass peak. The Hadron TDC's cosmic ray rejection cuts removes events with Δ_{TDC} less than -10 nsec.

4.5   Efficiency of cosmic rays rejection

We now estimate the rejection efficiency of the back-to-back veto in Run 1A by using a larger sample of 693 dimuon events for which the cut on the beam constrained momentum is not applied. Specifically, we do not require P_t(beam constrained) > 20 GeV/c. In addition, events in the region of 91 ± 30 GeV/c^2 around the Z mass are removed. The Hadron TDC's are used to select events that are clearly out-of-time with respect to the beam crossing by requiring Δ_{TDC} < -15 nsec instead of the standard Δ_{TDC} < -10 nsec cut. Of these 693 events, 145 dimuons are identified as clearly out of time cosmic rays by the Hadron TDCs.

The top part of Figure 4.16 shows that out of 145 cosmic ray candidates 3 events or 2.1% ± 1.2% are not rejected by the *nominal* 88/89 back-to-back veto, and 32 events (22.1% ± 0.4%) are not rejected by the *narrow* back-to-back veto. Therefore, in Run 1A we estimate the efficiency of the *nominal* 88/89 and *narrow* back-to-back veto in rejecting cosmic rays to be 97.9% ± 1.2%, and 77.9% ± 0.4%, respectively. The bottom part of Figure 4.16 shows the data for a sample of cosmic rays from Run 1B. Table 4.2 summarizes the inefficiency of back-to-back veto cuts for a 550 GeV/c^2 Z' (from Monte Carlo simulation) and the cosmic ray rejection efficiencies using data samples from runs 1A and 1B.

We can use a similar technique to determine the efficiency of cosmic ray rejection of the Δ_{TDC} cuts. In this case, we start again with the 693 dimuon event sample without the beam constrained vertex requirement (Run 1A sample). We then select an *enriched* cosmic ray sample by requiring the events to be within the *nominal* 88/89 back-to-back
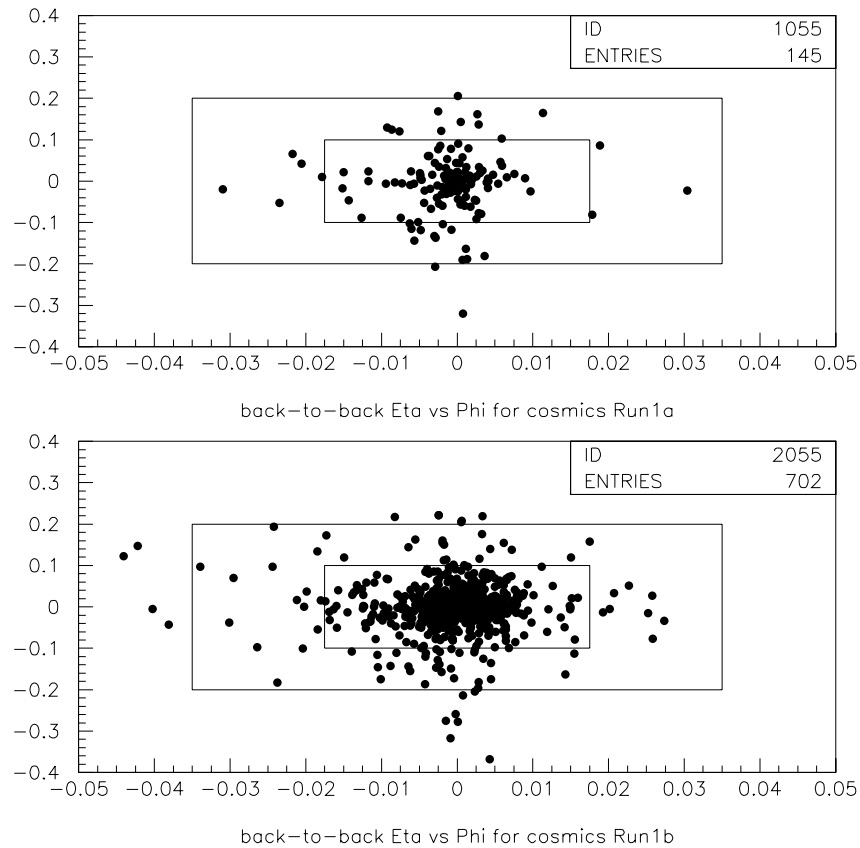
Figure 4.16: Top: The distribution of cosmic ray muons in the sum η - difference ϕ plane for Run 1A. This cosmic ray muon sample is selected by removing the beam constraints in the track fitting, and requiring $\Delta_{TDC} <$ -15 nsec. Events in the Z mass region are also removed. Bottom: The same distributions for cosmic ray events in Run 1B. The outer box is the *nominal*, and the inner box is the *narrow* back-to-back cosmic ray veto boundary.

Table 4.2: Percentage of Z' events (at $M_{Z'}$ of 550 GeV/c^2) lost due to back-to-back veto and rejection efficiency of cosmic rays using the back-to-back veto for Run 1A and Run 1B

Type of cut	550 GeV Z'	1A cosmics	1B cosmics
Narrow cuts (with 2 TDCs)	4%	113/145 (77.9%)	613/702 (87.3%)
nominal cuts (with $\leq$ 1 TDC)	12%	142/145 (97.9%)	684/702 (97.4%)
wide cuts (not used)	34%	145/145 (100%)	702/702 (100%)

veto cut region. In addition we require events to have the invariant mass of the two muon legs outside the Z region (91 ± 30 GeV/c^2). In this study, we find a total of 193 cosmic ray events passing the above cuts. In this sample, 169 events have Hadron TDC information for both legs.

The bottom part of Fig. 4.14 shows the Δ_{TDC} distribution for sample of 169 cosmic ray events. Of these 169 events, 3 events (or 1.8% $\pm$ 1.0%) fail the cut on Δ_{TDC}. Therefore, in Run 1A the $\Delta_{TDC} < $ -10 nsec timing cut is 98.2% $\pm$ 1.0% efficient in removing cosmic rays from the sample, when Hadron TDC information is available for both legs. The timing requirement is that events with *either* $\Delta_{TDC} < 10$ nsec, *or* with the *absolute* value of the *individual* Hadron TDC outside of the nominal $\pm$ 14 nsec are *removed*. We find that for this requirement, the cosmic rays in Run 1A are rejected with an efficiency of 99.4% $\pm$ 0.6% (168/169 events).

Table 4.3 summarizes the the resulting inefficiency in the Z' selection measured by applying the cuts to a sample of Z events (see top plots in Figs 4.14 and 4.15) and efficiencies of the timing cuts in the rejection of cosmic ray events (see bottom plots in Figs 4.14 and 4.15) from Run 1A and Run 1B respectively.

Table 4.3: TDC cuts in runs 1A and 1B: Efficiencies for cosmics rejection and corresponding inefficiencies in the selection of Z events

Type of cut	1A($Z_{inefficiency}$)	1A$_{cosmics}$	1B($Z_{inefficiency}$)	1B$_{cosmics}$
$\Delta_{TDC} <$ -10 nsec *only*	2.7±0.9% (8/299)	98.2±1.0% (166/169)	3.6±0.5% (43/1446)	96.6±0.6% (775/802)
$\Delta_{TDC} <$ -10 nsec or Top or Bottom out of time	3.0±1.0% (9/299)	99.4±0.6% (168/169)	4.5±0.9% (52/1446)	98.0±0.5% (786/802)
Top out of time *only*	1.6±0.7% (5/311)	80.1±3.4% (141/176)	0.8±0.2% (12/1527)	75.4±1.4% (628/833)
Bottom out of time *only*	0.3±0.7% (1/320)	15.1±2.8% (28/186)	0.7±0.2% (12/1546)	19.8±1.4% (164/827)

4.6 Estimate of cosmic ray contamination in the high mass dimuon sample

We now estimate the cosmic ray contamination in the high mass dimuon sample for Run 1A. With no cosmic ray veto cuts applied to the sample, we find 10 events with invariant mass greater than 200 GeV/c^2. All 10 high mass events in Run 1A have Hadron TDC information for both muons. Of these 10 events, we find 1 event passing both the Hadron TDC timing cuts and also the *narrow* and *nominal* 88/89 back-to-back veto cuts. All of the other 9 events are out of time, and also within the *nominal* back-to-back region. Therefore, it is clear that these 9 events are all cosmic rays. An estimate of the number of cosmic rays remaining in the Run 1A sample at high mass is determined as follows. The probability for a cosmic ray event to survive both the timing cut and the *narrow* back-to-back veto cut is given by the 0.6% ± 0.6% (from timing) × 22.1% (from back-to-back) or 0.0013 with an uncertainty of about 100%. Therefore, the expected number of cosmic ray events in this Run 1A sample above a mass of 200

GeV/c^2 is 9 events times (1.3×10^{-3}) or 0.012 ($\pm$ 0.012) events.

A similar estimate of the background for the Run 1B dimuon sample gives the cosmic ray background to be less than 0.1 events.

Chapter 5

Results of Search

In this chapter we outline briefly the results of the search. Of the events that pass the cuts, the highest mass event from Run 1A has a dimuon invariant mass slightly above 200 GeV. The highest mass event from Run 1B has a dimuon invariant mass at an approximate mass of 320 GeV.

Figure 5.1 shows the highest mass event from Run 1A. It is a dimuon pair recoiling against a jet. Figures 5.2, 5.3, 5.4 show the three highest mass events from Run 1B. A brief description of the three highest mass events is given below.

The highest mass event (Figure 5.2) is from Run # 64975 Event # 188218, with a dimuon invariant mass of 320 GeV. There are two very high P_t muons in this event:

Muon P_t(1st muon) = 174. GeV, Fiducial CMUP, positively charged

Muon P_t(2nd muon) = 137. GeV, Fiducial CMUP, negatively charged

TDCs are : 7.5 ns, 6.4 ns; well in time with respect to the interaction itself.

Back-to-Back in ϕ (5 degrees) but not so in η.
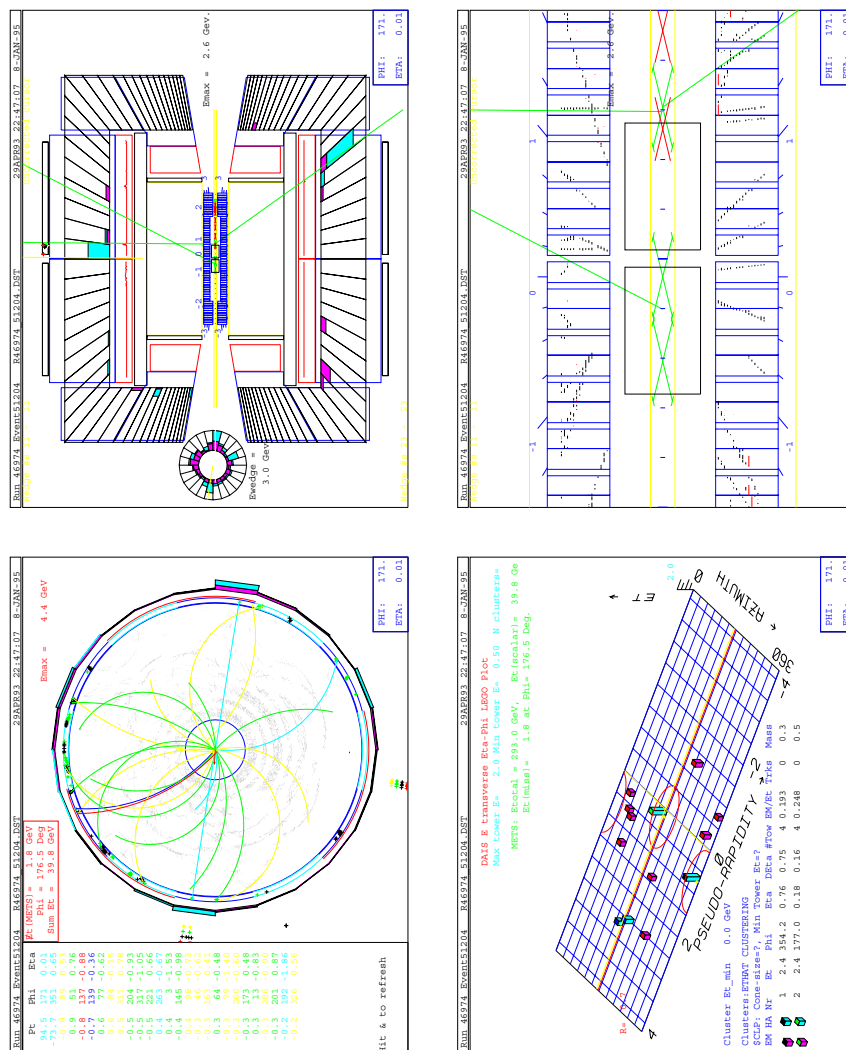
Figure 5.1: The four figures show the highest mass dimuon event recorded during the Run 1A. The top left figure shows the CTC view of the event. The two very straight tracks are the tracks of the muons. The figure on the top right shows the side view of the detector, and the tracks emerge from a vertex. The figure on the bottom left shows the calorimetric energy deposition as a function of $\eta - \phi$. The right hand figure on the bottom shows an expanded side view of the detector showing the position in the vertex chamber (VTX) from where the tracks emerge.

The negative muon is along proton direction.

The second highest mass event (Figure 5.3) is from Run # 61124 Event # 307203, with a dimuon invariant mass of 303 GeV. There are two very high P_t muons in this event:

Muon P_t(1st muon) = 131. GeV, Fiducial CMUP, positively charged

Muon P_t(2nd muon) = 128. GeV, CMX, negatively charged

TDCs are : 4.6 ns, 6.4 ns; well in time with respect to the interaction itself.

Back-to-Back in ϕ but not so in η.

The negative muon is along proton direction.

The third highest mass event (Figure 5.4) is from Run # 64358 Event # 277019, with a dimuon invariant mass of 292 GeV. There are two very high P_t muons in this event:

Muon P_t(1st muon) = 107. GeV, Fiducial CMUP, positively charged

Muon P_t(2nd muon) = 139. GeV, CMIO track, negatively charged

TDCs are : 3.0 ns, 5.4 ns; well in time with respect to the interaction itself.

Back-to-Back in ϕ but not so in η.

The negative muon is along proton direction.

All the three dimuon events have positive asymmetry and are consistent with the expected Drell-Yan background.
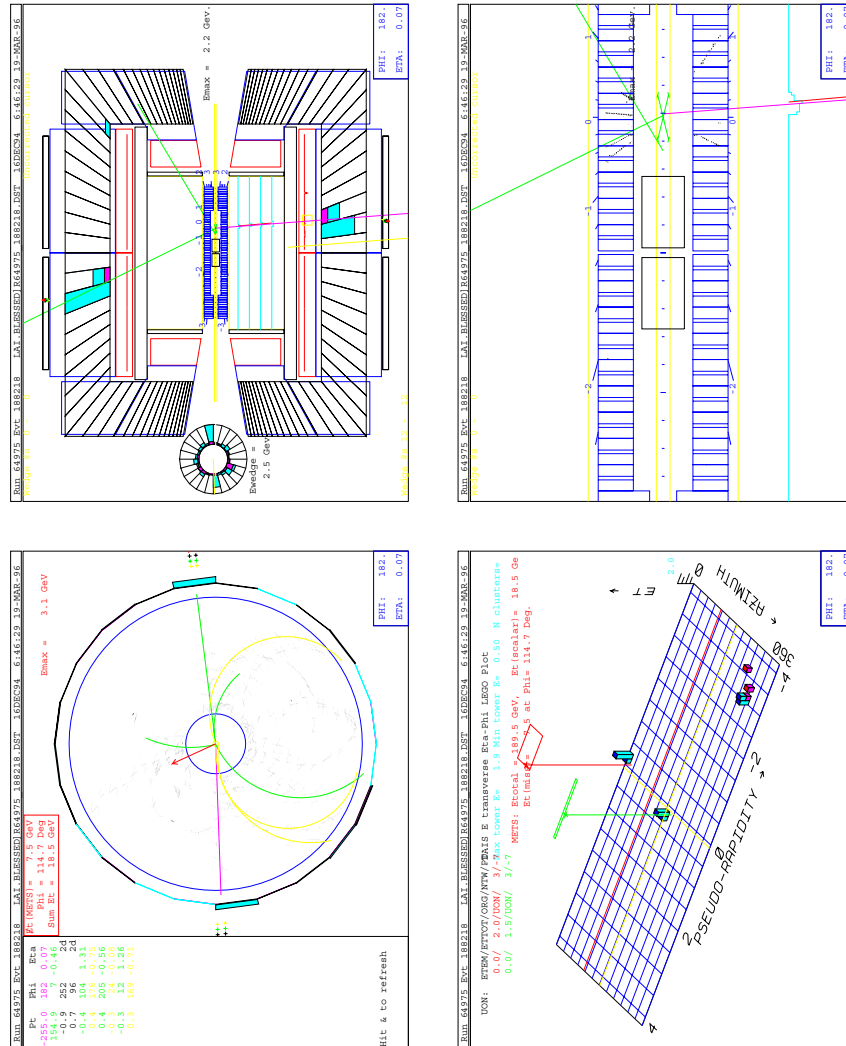
Figure 5.2: The four figures show the highest mass dimuon event recorded during the Run 1B. The top left figure shows the CTC view of the event. The two very straight tracks are the tracks of the muons. The figure on the top right shows the side view of the detector, and the tracks emerge from a vertex. The figure on the bottom left shows the calorimetric energy deposition as a function of $\eta - \phi$. The right hand figure on the bottom shows an expanded side view of the detector showing the position in the vertex chamber (VTX) from where the tracks emerge.
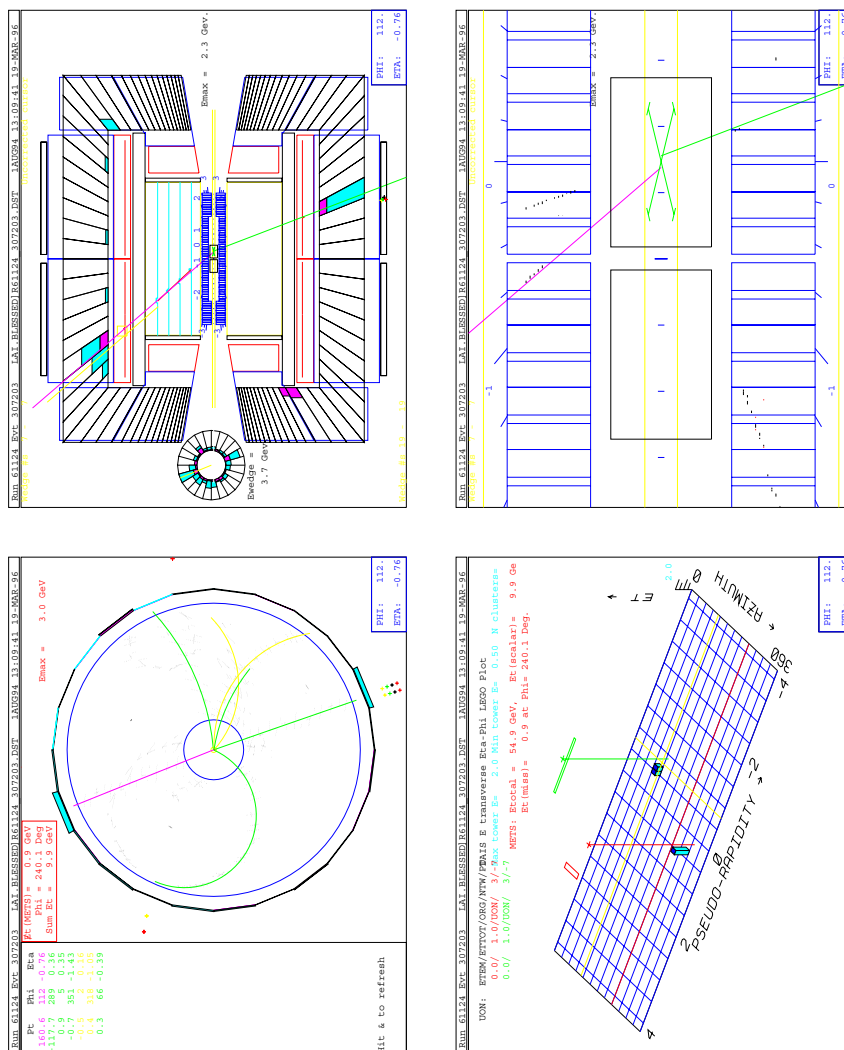
Figure 5.3: The four figures show the second highest mass dimuon event recorded during the Run 1B. The top left figure shows the CTC view of the event. The two very straight tracks are the tracks of the muons. The figure on the top right shows the side view of the detector, and the tracks emerge from a vertex. The figure on the bottom left shows the calorimetric energy deposition as a function of $\eta - \phi$. The right hand figure on the bottom shows an expanded side view of the detector showing the position in the vertex chamber (VTX) from where the tracks emerge.
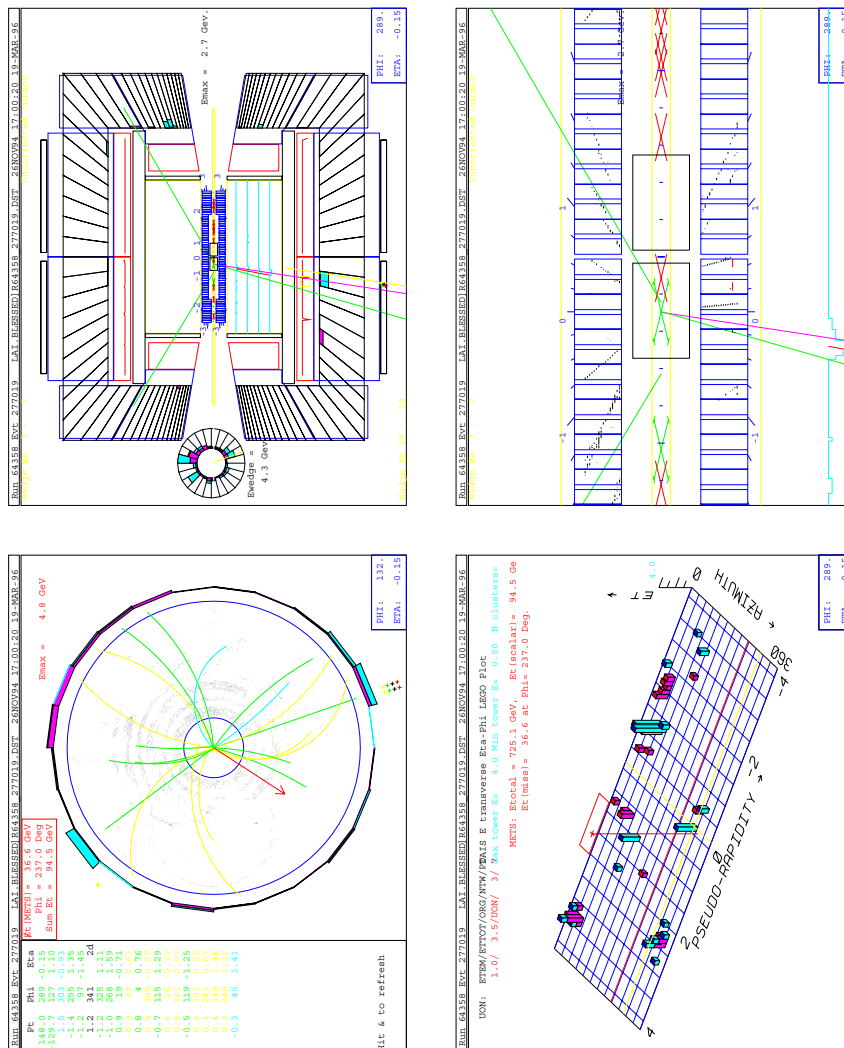
Figure 5.4: The four figures show the third highest mass dimuon event recorded during Run 1B. The top left figure shows the CTC view of the event. The two very straight tracks are the tracks of the muons. The figure on the top right shows the side view of the detector, and the tracks emerge from a vertex. The figure on the bottom left shows the calorimetric energy deposition as a function of $\eta - \phi$. The right hand figure on the bottom shows an expanded side view of the detector showing the position in the vertex chamber (VTX) from where the tracks emerge.
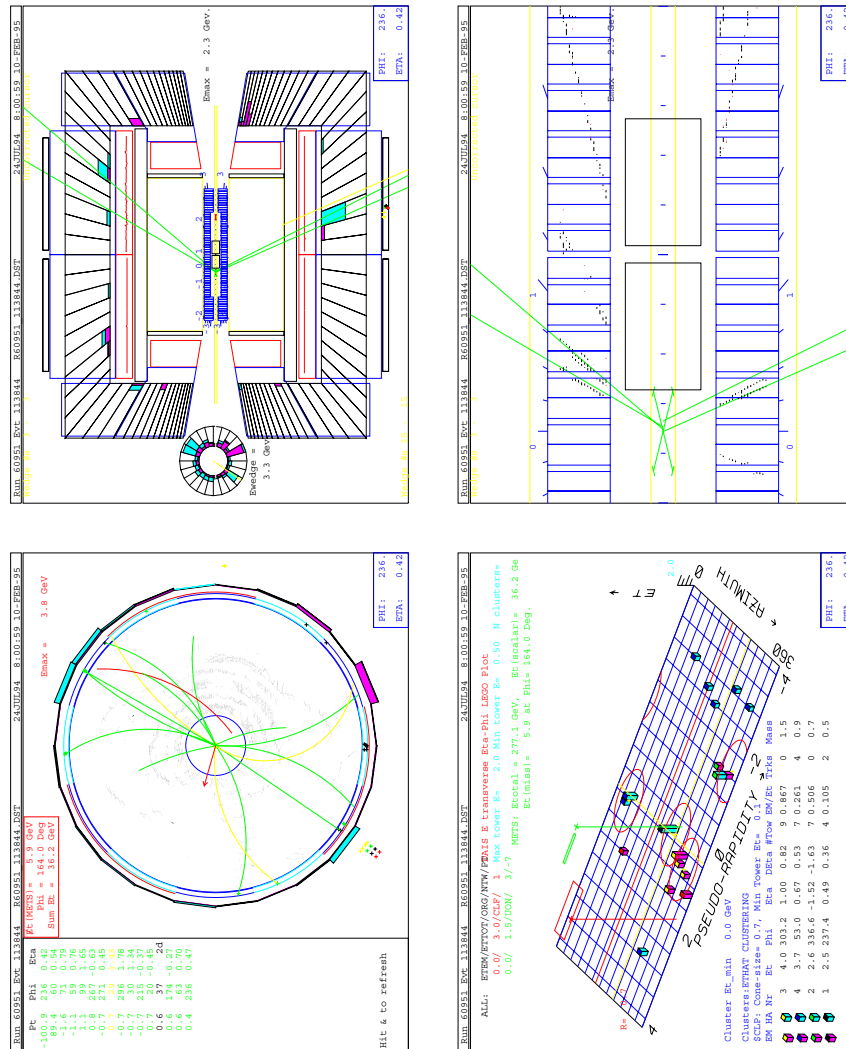
Figure 5.5: Run 1B event : Dimuon. This event fails the cut on the difference in the Hadron TDCs by 0.3 ns. This is consistent with the inefficiency of this cut. The fact that the angle between the muons is outside the wide cosmic ray veto indicate that this is a good dimuon event.
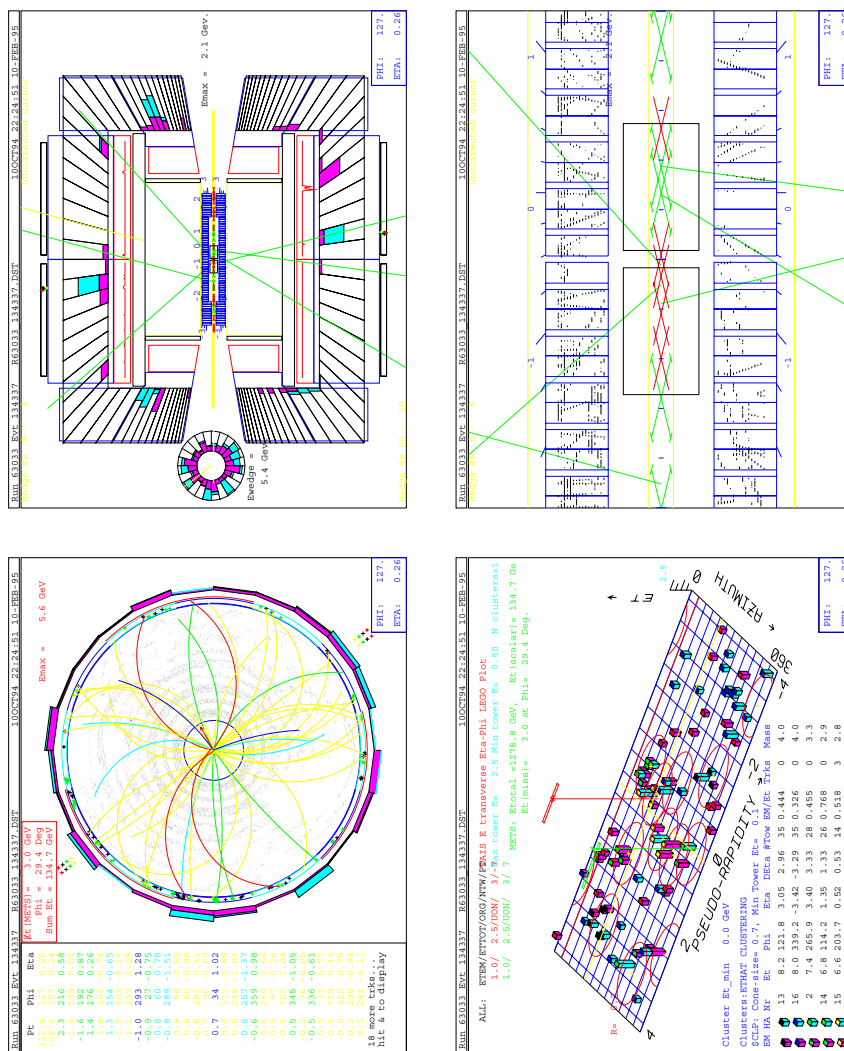
Figure 5.6: Run 1B event : W + cosmic ray. One side of the cosmic ray muon track is reconstructed by the CTC while the other side is not reconstructed at all. However, the EM and Hadron towers opposite the one muon leg indicate that there is another muon. He, a single muon from a W is picked up as one of the muons in the dimuon event selection program. This event is not rejected even by a wide cosmic ray veto. However, the Hadron TDC information corresponding to the reconstructed section of the cosmic ray track clearly shows the muon to be out of time and it is rejected as a cosmic ray by the TDC cuts.

Chapter 6

Efficiencies

In order to carry out the search for a new particle we have to understand the data
on the basis of the existing theory (Standard Model). We need to study whether the
results are consistent with the Standard Model. To do that, we need to "simulate"
what the data should look like on the basis of the efficiency of the cuts and the detector
acceptance (geometric and kinematic). The efficiencies of the detector dependent cuts
are determined by an analysis of the data sample using Z events. The geometric and
kinematic acceptance is usually determined from a simulation of the detector. Eventu-
ally the two are combined in a simulation, and this simulation is used to predict what
the data should look like. In this chapter we study the efficiencies of the muon identifi-
cation cuts, i.e. given a good muon, what is the probability that it would pass a certain
identification cut (isolation, minimum ionizing or dx cuts). In general, this efficiency
depends on the momentum of the muon. However, we select Z events and determine
the efficiency from Z events. We justify the procedure a-posteriori by showing that
the dependence of the efficiency on the muon momentum is small. However, there are

several cuts for which the dependence of the cut efficiency on the muon momentum is significant, especially for high mass Z' events. For these cuts, the ratio of the efficiency for high momentum muons (originating from Z' decays) to the efficiency for muons of energy 40 GeV is separately studied.

In the final phase we simulate Z' events and then estimate the overall efficiency of our detector to detect Z' events based on the cut efficiencies and the kinematic identification. This overall efficiency is a function of the mass of the Z'. The reconstructed mass of the Z', in general, is different compared to the real mass as it is clearly affected by the resolution of our detector. Therefore, one piece of information we need to know is how well our detector reconstructs the mass of the dimuon pair, i.e., the effect of the detector resolution as a function of Z' mass. Armed with this information, we will get a good idea of how the signal looks like. In addition, we will still need to simulate the Standard Model Drell-Yan background (since that is indistinguishable from Z' decays), which is the subject of a later chapter.

6.1 Efficiencies of muon identification

We show in Table 6.1 the cuts that are used to select the event sample. Each of these cuts that is applied to the data sample reduces the signal. However,these cuts reduce background to a larger extent and hence improves the ratio of signal to background. As we apply these cuts, we need to study the effect of these cuts on the signal, viz. what fraction of the signal survives the cut. Here we briefly explain how the efficiency of each of these cuts (i.e. how much of the signal survives the cut) is estimated.

- **Kinematic Cuts**

  The effect of these cuts is estimated using a Monte-Carlo simulation of Z' or Z events.

- **Minimum ionizing cuts**

  The effect of these cuts in the Z mass region is estimated using the Z events themselves. A GEANT simulation is used to study the inefficiency of the cuts for high momentum muons arising from Z' decays or high mass Drell-Yan processes.

- **Vertex Requirement**

  This distribution arises from the fact that the collisions can occur over a wide region, and therefore the event vertex could be anywhere. It is normally distributed with a mean position of 0 cm (roughly) and a standard deviation of approximately 26-30 cm. The efficiency is determined from the Monte-Carlo to be 95.5%.

- **Track to Vertex matching**

  The track to vertex matching cut is studied using the Z events (see below).

- **Tracks extrapolate to the same point on the Z axis**

  We studied the distribution of this variable for tightly cut Z events with cosmic rays removed by stringent back-to-back requirements. This efficiency was found to be above 97%. This efficiency is multiplied to give the final overall efficiency.

- **Well measured tracks**

  The efficiency of this cut is included in the efficiency study that we have done using the Z events.

- **Track to muon stub matching**

  This efficiency is measured below in the Z efficiency study.

- **Isolation efficiency**

  This efficiency is measured in the efficiency study that we do below.

- **Triggerable track**

  This requirement means that the track in Central Tracking Chamber should point to an active area of the muon chambers. This is a geometric requirement, and therefore it is simulated in the Monte-Carlo.

- **Track is in active CTC region**

  This requirement is also a fiducial(geometric) requirement, and it is also simulated in the Monte-Carlo.

- **Trigger requirement**

  This is included in the overall efficiency calculation as a Trigger efficiency. The efficiency of the triggers were measured by using tightly selected Z events and requiring that one of the muons satisfy a different trigger requirement. The second muon can now be used to measure the efficiency of the triggers.

- **Cosmic Ray removal**

  The efficiency of these cuts for real events was measured in a previous chapter on Cosmic Rays. The efficiency of the TDC cuts were measured using Z events, while the efficiency of the back-to-back cuts were measured using a Monte-Carlo simulation (See Table 4.3 and Table 4.2 in section 4.5 of chapter 4.

- **Badrun removal**

  Badruns are runs where important sections of the detector (i.e. those that are relevant to this analysis) were not working or were flagged as having problems. For our analysis, bad runs include runs where the Central Muon chambers (CMU or CMP) malfunctioned, or when the trigger malfunctioned or the entire detector developed problems. Events from such runs were not included in the analysis and therefore, the luminosity from these runs was not included as well. Removing badruns from the sample reduces the integrated luminosity of the sample.

Table 6.1: This table shows the definition of the *tight* and *loose* requirements as applied in the event selection procedure.

Type of cut	*Tight* cut	*Loose* cut
Kinematic cuts:		
Transverse Momentum, P_t	> 18 GeV	>18 GeV
(after beam constraint), P_t^{beam}	> 20 GeV	>20 GeV
Minimum ionizing cuts :		
Energy in EM calorimeter	< 2 GeV	< 2 GeV
Energy in Had calorimeter	< 6 GeV	< 6 GeV
Vertex requirement, $|Z_{vertex}|$	< 60 cm	< 60 cm
Track to Vertex matching, $|\Delta Z|$	< 5 cm	< 5 cm
Tracks extrapolate to the same point on the Z axis		
$|Z_\mu^1 - Z_\mu^2| < 10$ cm	YES	YES
Well measured track, $|\frac{\delta curv}{curv}| < 0.3$		
	YES	YES
Track- muon stub matching		
dx (CMU)	< 2 cm	not applied
dx (CMP)	< 5 cm	not applied
(with CMP confirmation)		
Isolation (calorimetry)	< 2 GeV	not applied
Triggerable Track (fiducial)	YES	not applied
Track is in active CTC region	not applicable	Applied only to CMIO [1]
Event should have set off triggers at level 1,2 and 3		
Cosmic Ray removal using back-to-back and Hadron TDC cuts		
Badruns are removed from the sample		

Thus in studying the efficiency of the *tight* cuts with Z events, we mean that we use only the *tight* quality cuts, and those quality cuts that are not simulated in the Monte-Carlo or determined in any other manner. The same consideration applies when we estimate the efficiency of the loose quality cuts.

6.1.1 Selection of efficiency sample

Efficiencies of the detector dependent muon identification cuts are determined by pre-electing Z events with no cuts except kinematic cuts applied on the second muon, and applying the cuts one by one to the second muon. The cuts that are applied on the first muon to preselect a clean sample of Z events are shown in Table 6.2.

Table 6.2: Table of cuts applied for selecting the efficiency sample

Type of cut	First muon	Second muon
Kinematic cuts:		
Transverse Momentum, P_t	> 18 GeV	>18 GeV
(after beam constraint), P_t^{beam}	> 20 GeV	>20 GeV
Minimum ionizing cuts :		
Energy in EM calorimeter	< 2 GeV	not applied
Energy in Had calorimeter	< 6 GeV	not applied
Vertex requirement, $|Z_{vertex}|$	< 60 cm	not applied
Track to Vertex matching, $|\Delta Z|$	< 5 cm	not applied
Tracks extrapolate to the same point on the Z axis		
$|Z_\mu^1 - Z_\mu^2|$ < 10 cm	YES	YES
Well measured track, $|\frac{\delta curv}{curv}|$ < 0.3		
	YES	not applied
Track- muon stub matching		
dx (CMU)	< 2 cm	not applied
dx (CMP)	< 5 cm	not applied
(with CMP confirmation)		
Isolation (calorimetry)	< 2 GeV	not applied
Triggerable Track (fiducial)	YES	NO
Track is in active CTC region	not applicable	Applied only to CMIO [2]
Invariant mass of dimuon required to be in the range 81-101 GeV		
Event should have set off triggers at level 1,2 and 3		
Cosmic Ray removal using the standard cosmic ray filter		
Badruns are removed from the sample		

The efficiencies of the respective cuts are determined by applying the cuts on the second muon.

The correlation between these cuts is taken into account by applying all the cuts at once and determining how many events pass the cuts. In the subsection that follows we outline the algebraic procedure whereby the efficiency of the cuts is determined.

6.1.2   Method of calculation

The technique for calculation of the efficiencies is based on a probabilistic analysis. First we classify the cuts. There are two different types of cuts that are applied to a muon.

- The first type of cut is a kinematic cut or a fiducial cut. A kinematic cut is a requirement on the energy-momentum of the particles involved in the physics process. This cut can be simulated with a detailed knowledge of the detector. A fiducial requirement is a spatial requirement on the coordinates of the detected particles or a spatial requirement on the vertex in the collision. For example, the muon chambers have spatial extension and any muon that does not fall within these coordinates cannot be detected by the muon chamber.

- The second type of cut is a detector dependent quality requirement that distinguishes between different types of particles. We take for an example the minimum ionising cut in the calorimeters. A high energy muon passing through the calorimeters (EM or HAD) deposits a certain minimum amount of energy. However, a small fraction of muons (depending on the quality of the detector) deposit a substantial amount of energy through catastrophic collisions.

These two types of cuts are different because of the manner in which their efficiencies (or acceptance as it is commonly referred to) are simulated.

The effect of a kinematic cut can be determined on the basis of general considerations and also partly from theory. For example, the kinematic cut can be simulated from a knowledge of the model i.e. once we know the P_t distribution of the muons from Z decays. The effect of the detector, in this case, is a "smearing" of momentum.

Given a muon from a Z decay, the chances that it passes a detector dependent cut is assumed to be probabilistic. In other words, one can assign a finite probability to this chance, and this value can be used in the simulation. This probability is considered to be independent of the kinematics of the decay or the spatial distribution of the decay, so long as the particle passes the kinematic and fiducial requirements. However, in order to simulate this type of cut, one needs as an input the probability that the muon passes the cut.

Here, we give an explanation of the procedure that is used to determine the probability that a Z event passing the kinematic and fiducial cuts passes the quality cuts (or the detector dependent cuts).

Let us define some probabilities. The probability that:

A *random* muon from a Z decay passes the *tight* cuts equals α_t given that the muon satisfies the tight fiducial requirements.

A *random* muon from a Z decay passes the *loose* cuts equals α_l given that the muon satisfies the loose fiducial and kinematic requirements. We also assume that the

probability of the loose cut does not depend on whether the muon is in the tight fiducial region or not.

We represent the total number of Z decays where both the muons satisfy the *tight* fiducial requirements by N_t.

The corresponding number of Z decays where one muon satisfies the *loose* fiducial requirements but not the tight requirements is represented by N_l. The second muon in this category is required to satisfy the *tight* fiducial requirement.

Now we will calculate the number of muons that pass these cuts subject to the condition that the Z events are selected by applying all the pre-selection cuts to any one muon.

We expect that when the Z particles decay within our detector the decay is expected to be random, i.e. there is an even chance that either of the muons may pass the *tight* cuts. Therefore, we categorize Z events in the following manner(see Table 6.3).

- Events where one muon passes the *tight* cuts and the second muon also passes the *tight* selection cuts, TT

- Events where one muon passes the *tight* cuts but the other muon does not pass the *tight* selection cuts, TO or OT depending on which one is the first muon.

- Events where neither muon passes the *tight* selection cuts represented by OO.

Since N_t events were classified in this manner,

$$N_t = (N_{TT} + N_{TO} + N_{OT} + N_{OO}) \qquad (6.1.1)$$

Table 6.3: Classification of the Z events for *tight* cuts

Number Category	Probability	Number of events
N_{TT}	$\alpha_t\alpha_t$	$N_t\alpha_t\alpha_t$
N_{TO}	$\alpha_t(1-\alpha_t)$	$N_t\alpha_t(1-\alpha_t)$
N_{OT}	$(1-\alpha_t)\alpha_t$	$N_t\alpha_t(1-\alpha_t)$
N_{OO}	$(1-\alpha_t)^2$	$N_t(1-\alpha_t)^2$

The last category of events do not make it into the efficiency sample because the events are selected by using the *tight* quality cuts on the first muon. So we do not observe all the N_t events.

We can now find the efficiency of the *tight* cut, α_t, in the following manner,

$$
\begin{aligned}
N_{passed} &= N_{TT} \\[2mm]
N_{total} &= (N_{TT} + N_{TO} + N_{OT}) \\[2mm]
R_t &= \frac{N_{passed}}{N_{total}} \\[2mm]
&= \frac{N_{TT}}{(N_{TT} + N_{TO} + N_{OT})} \\[2mm]
&= \frac{\alpha_t}{(2 - \alpha_t)} \\[2mm]
\alpha_t &= \frac{2R_t}{1 + R_t}
\end{aligned}
\tag{6.1.2}
$$

In the above argument, we define N_{passed} as those events that passed the *tight* cuts on both the muons, while N_{total} is the number of events that were selected to form the efficiency sample. Both are directly observable.

For finding the efficiency of the *loose* cut, an easy technique is to require that one muon satisfy *tight* quality and fiducial cuts and the second muon satisfy only the *loose*

quality cuts but not be in the *tight* fiducial region. In this case the categorization of Z

decays based on the quality of the muons is shown in Table 6.4

Table 6.4: Classification of the Z events for *loose* cuts

Category	Probability	Number of events
N_{TL}	$\alpha_t \alpha_l$	$N_l \alpha_t \alpha_l$
N_{TO}	$\alpha_t(1 - \alpha_l)$	$N_l \alpha_t(1 - \alpha_t)$

The category of events represented by N_{TL} are events that have one muon passing

the *tight* cuts and the other muon passing the *loose* cuts but also not satisfying the

tight fiducial requirements. In this case, the category of events represented by N_{TO} are

those that have one muon passing the *tight* cuts with the other muon not passing *loose*

cuts, but also not satisfying the *tight* fiducial requirement (geometric region).

In this case the efficiency is merely given by,

$$\alpha_t = \frac{N_{TL}}{(N_{TL} + N_{TO})} \qquad (6.1.3)$$

The efficiencies of the individual quality cuts are set by a different equation. Each

of the individual quality cuts is used in the pre-selection, as part of the *tight* cut re-

quirement. Suppose we remove the cut in question from the sample selection procedure.

Then, assuming that this individual cut is not correlated substantially with the rest of

the *tight* cut requirements, it is possible to now find the individual cut efficiencies in

the same manner as in the case of the *tight* cuts. Thus, the efficiency sample has two

different criteria in its pre-selection process. The first criterion is the rest of the *tight*

cuts except for the cut that we are using to determine the efficiencies. Again, we go

through the same procedure as before for the *tight* cuts and therefore, use the same formulation.

In each of the above equations we have assumed that the events in the pre-selection have no background. However, this is rarely the case.

In this analysis, for example, there is background coming from W + jets events. The W could decay into a high P_t muon and the jet could fake the second muon, due to *punchthrough*. However, tracks within jets are as likely to be of the same sign as the original muon as they could be of opposite sign. By sign of the track we mean, the sign of the charge of the particle that causes the track. Such background could also come from underlying events and multiple interactions. Therefore, in a category C, we determine the number of same sign as well as opposite sign events.

$$N_{obs,C} = N_{Z,C}^{os} + N_{bkgd,C}^{os} + N_{bkgd,C}^{ss} \qquad (6.1.4)$$

where the left side of equation 6.1.4 represents the observed number of events in a Category and the terms on the right hand side represent the real Z events (which are of opposite sign) , the opposite-sign background and the same-sign background respectively. Notice that we assumed that the same-sign background and the opposite sign backgrounds are identical.

$$N_{obs,C}^{os} \;\; = \;\; N_{Z,C}^{os} + N_{bkgd,C}^{os}$$

$$or, \;\; N_{obs,C}^{ss} \;\; = \;\; N_{bkgd,C}^{ss}$$

$$or, \;\; N_{obs,C}^{os} - N_{obs,C}^{ss} \;\; = \;\; N_{Z,C}^{os} + N_{bkgd,C}^{os} - N_{bkgd,C}^{ss}$$

$$or, \;\; N_{obs,C}^{os} - N_{obs,C}^{ss} \;\; = \;\; N_{Z,C}^{os} \qquad\qquad (6.1.5)$$

After the assumption that the same sign and the opposite sign backgrounds are equal, we see that the background corrected number of events in any category is given by the number of events of opposite sign minus the number of events of same sign. This background becomes especially important at the high instantaneous luminosities encountered in Run 1B.

Table 6.5 summarizes the efficiencies for Run 1A. Figure 6.2 shows the dependence of the efficiency of each of the detector dependent cuts as a function of the muon's transverse momentum (P_t). This P_t dependence is studied to make certain that the cuts do not become severely inefficient for large P_t muons. In order to eliminate any bias coming from the P_t dependence of the muons we average over the transverse momenta of the two muons and then study the efficiency as a function of this average momentum.

Figure 6.1: The distribution of the identification variables for muons, and the cuts applied on these for real Z events (Run 1A). The dimuons in the background events were of the same sign, and are not shown in the figure.
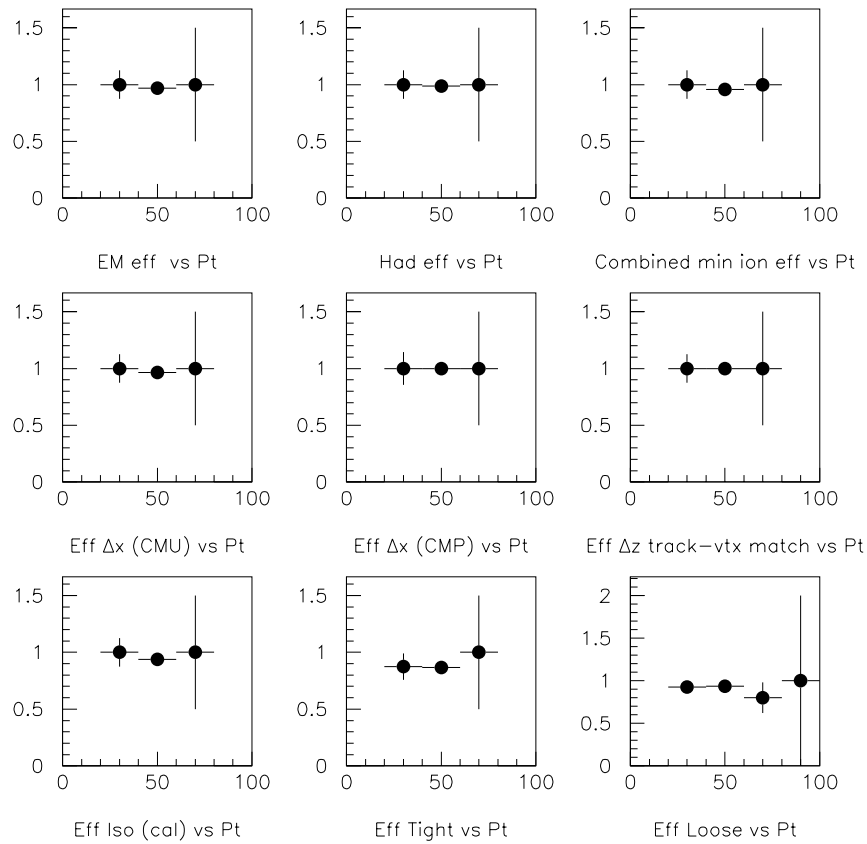
Figure 6.2: The momentum dependence of the efficiencies of the cut variables as a function of the muons transverse momentum. From the figures it is clear that the dependence of each of the detector cuts on the average transverse momentum of the muons is within the expected statistical fluctuations.

Table 6.5: Number of events passing different cuts in Run 1A. N^{os}_{passed} represents the number of Z events that passed, out of a total of N^{os}_{total} events for which the cut was applied on the second muon. Here dimuons are required to be of opposite sign. N^{ss}_{passed} represents the number of Z events that passed, out of a total of N^{ss}_{total} events for which the cut was applied on the second muon. The dimuons are required to be of the same sign.

Type of cut	$N^{os}_{passed}/N^{os}_{total}$	$N^{ss}_{passed}/N^{ss}_{total}$	Efficiency (%)
Minimum ionizing cuts			
EM < 2 GeV	125/133	0/0	$96.9^{+0.8}_{-1.5}\%$
Had < 6 GeV	130/133	0/0	$98.9^{+0.3}_{-1.1}\%$
Combined min ion cuts	122/133	0/0	$95.7^{+0.9}_{-1.7}\%$
Track stub matching cuts			
dx (CMU) < 2 cm	124/133	0/0	$96.5^{+0.8}_{-1.5}\%$
dx (CMP) < 5 cm (with CMP confirmation)	99/99	0/0	$100.0^{+0.0}_{-0.9}\%$
Combined dx matching	124/133	0/0	$96.5^{+0.8}_{-1.5}\%$
Isolation < 2 GeV	117/133	0/0	$93.6^{+1.2}_{-1.9}\%$
ΔZ matching	133/133	0/0	$100.0^{+0.0}_{-0.7}\%$
Combined *loose* cuts	272/295	0/0	$92.8^{+1.2}_{-1.8}\%$
Combined *tight* cuts	98/133	0/0	$85.6^{+2.0}_{-2.6}\%$

The overall efficiency of the identification cuts for the *tight* cuts is 85.6% for Run 1A data. [9] Efficiencies are determined in a similar manner for Run 1B. Figure 6.3 shows the distribution of the identification variables of the second leg of Z events that are selected as before and the cuts applied. From the figure, it is clear that the cuts applied are very efficient in selecting real Z events. Figure 6.4 shows the dependence of the efficiency of each of the detector dependent cuts as a function of the muon's P_t. This P_t dependence is studied to make certain that the cuts do not become severely inefficient at large P_t. The minimum ionizing cuts for the Electromagnetic and the Hadronic Calorimeters are, however, energy dependent. This energy dependence is studied using a simple GEANT Monte-Carlo simulation of the detector.
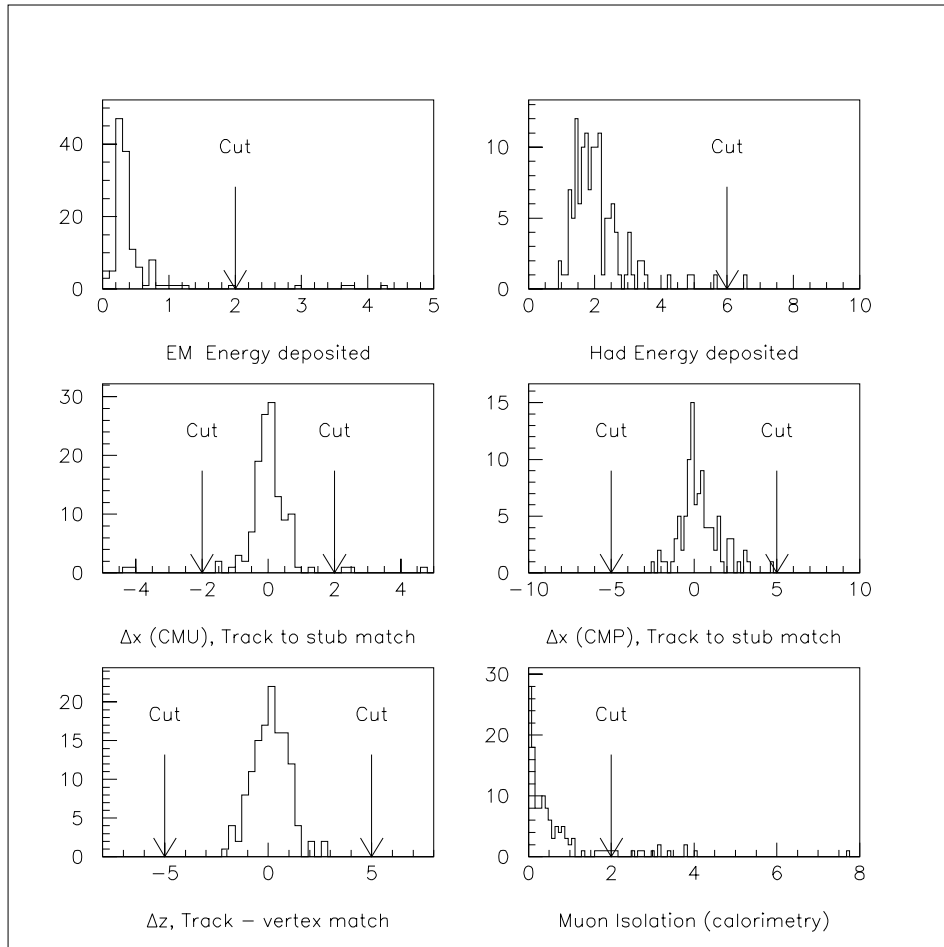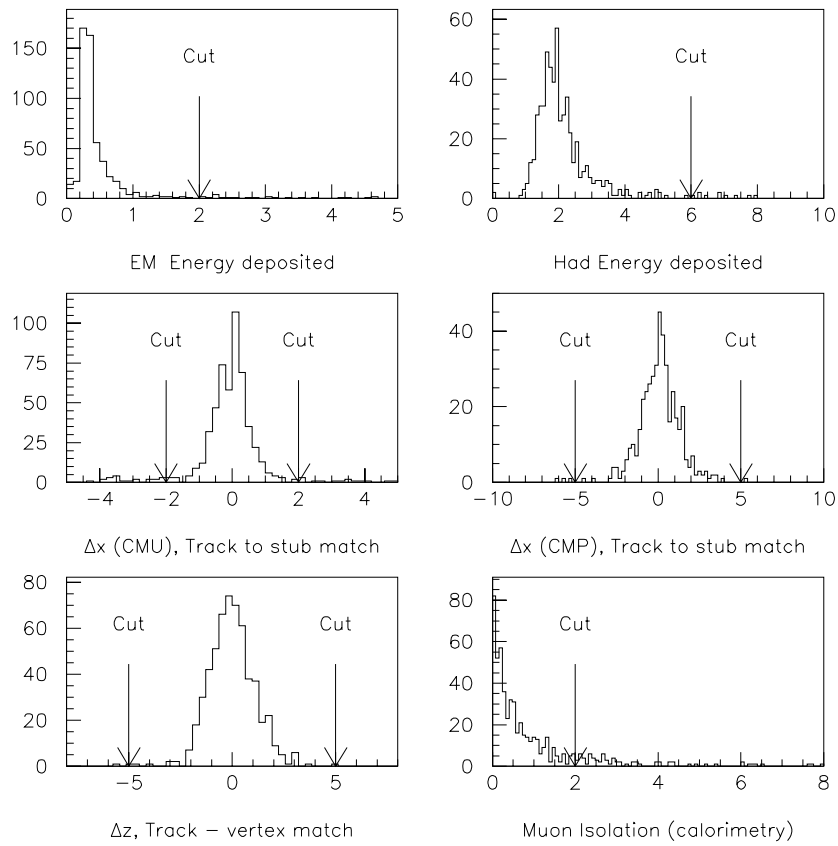
Figure 6.3: The distribution of the identification variables for muons, and the cuts applied on these for real Z events.

Table 6.6 summarizes the efficiencies for Run 1B.

Table 6.6: Number of events passing different cuts in Run 1B. N^{os}_{passed} represents the number of Z events that passed, out of a total of N^{os}_{total} events for which the cut was applied on the second muon. Here dimuons are required to be of opposite sign. N^{ss}_{passed} represents the number of Z events that passed, out of a total of N^{ss}_{total} events for which the cut was applied on the second muon. The dimuons are required to be of the same sign.

Type of cut	$N^{os}_{passed}/N^{os}_{total}$	$N^{ss}_{passed}/N^{ss}_{total}$	Efficiency (%)
Minimum ionizing cuts			
EM < 2 GeV	531/566	0/2	$97.5^{+0.4}_{-0.6}\%$
Had < 6 GeV	544/566	0/2	$98.2^{+0.3}_{-0.5}\%$
Combined min ion cuts	515/566	0/2	$95.5^{+0.6}_{-0.7}\%$
Track stub matching cuts			
dx (CMU) < 2 cm	503/566	0/2	$94.3^{+0.6}_{-0.8}\%$
dx (CMP) < 5 cm (with CMP confirmation)	431/435	0/2	$99.5^{+0.1}_{-0.4}\%$
Combined dx matching	500/566	0/2	$94.0^{+0.6}_{-0.8}\%$
Isolation < 2 GeV	483/566	0/2	$92.3^{+0.7}_{-0.9}\%$
ΔZ matching	566/566	0/2	$100.0^{+0.0}_{-0.2}\%$
Combined *loose* cuts	1275/1380	0/2	$92.8^{+0.6}_{-0.8}\%$
Combined *tight* cuts	382/566	0/2	$80.8^{+1.2}_{-1.3}\%$
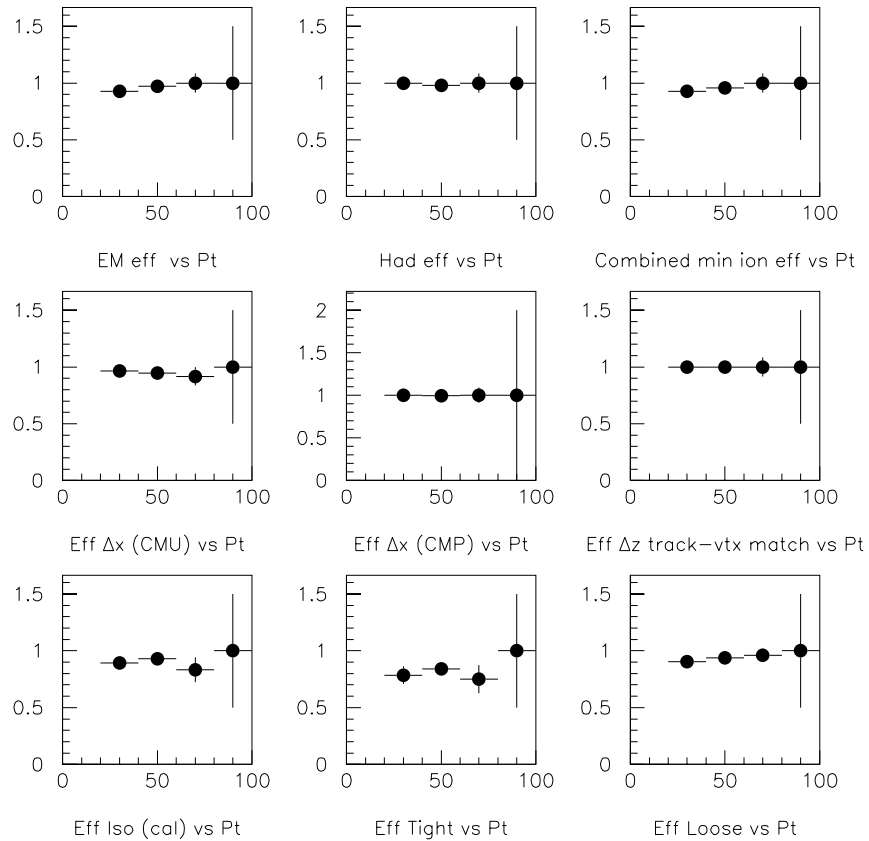
Figure 6.4: The momentum dependence of the efficiencies of the cut variables as a function of the muons transverse momentum. From the figures it is clear that the dependence of each of the detector cuts is minimal.

6.2 GEANT study of the momentum dependence of EM and HAD cuts

The mean energy deposition of low momentum cosmic ray muons in the EM calorimeter is 0.3 GeV. The mean energy deposition of low momentum cosmic muons in the hadron calorimeter is 1.85 GeV. For muons from Z decays (W. Badgett [9], and P. Schlabach [17]) the mean energy deposition in the electromagnetic calorimeter is 0.4 GeV, and the mean energy deposition in the hadron calorimeter is 2.0 GeV. The following are the standard muon selection cuts that require a minimum ionizing signal in the EM and Hadron calorimeters.

- EM Energy (energy deposited in EM calorimeter)< 2 GeV

- Had Energy (energy deposited in Had calorimeter)< 6 GeV

These minimum ionizing cuts are very reasonable cuts to apply to muons originating for Z decays. However, as the muon momentum increases, the mean energy deposition in the EM and hadron calorimeters increases linearly with momentum [16]. For momenta greater than 20 GeV the mean energy deposition in the hadron calorimeter is given approximately by the expression $2 + 4\ P(muon)/500$, where $P(muon)$ is given in GeV/c. This implies that the mean energy deposition in the hadron calorimeter increases from 2 GeV for low momentum muons to 4.4 GeV for 300 GeV/c muons. For 500 GeV/c muons the mean energy deposition in the hadron calorimeter is 6 GeV, which is equal to the value of the CDF minimum ionizing cut. Figure 6.5 shows the comparison of energy deposition for muons from Z's (CDF data), from 50 GeV and 400 GeV muons using

GEANT CDF simulation. The energy scale of GEANT distributions is normalized to match the average deposited energy of muons from CDF data distributions at average muon momenta of 40 GeV/c. The left-hand column corresponds to muon energy deposition in the EM calorimeter, while the right-hand column corresponds to that in the Hadron calorimeter.
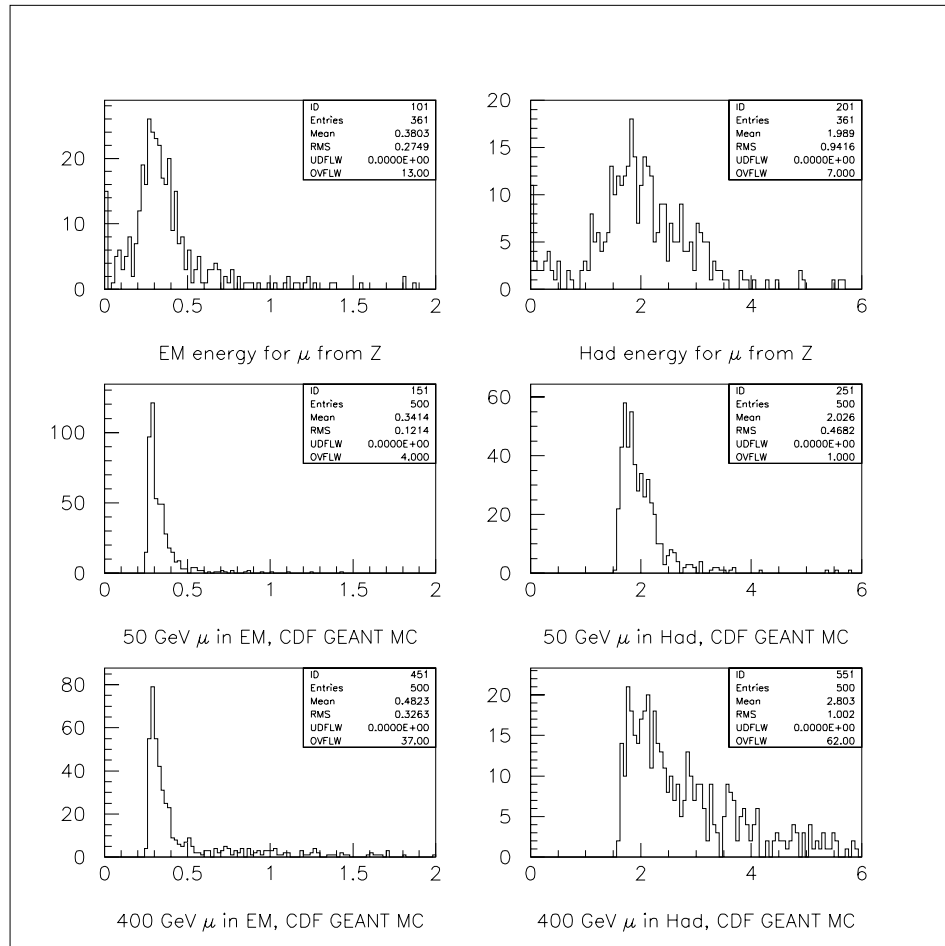
Figure 6.5: Comparison of muon energy depositions for muons from Z's (CDF data), from 50 GeV and 400 GeV muons using GEANT CDF simulation. The energy scale of GEANT distributions was normalized to match the average deposited energy of muons from CDF data distributions at at average muon momenta of 40 GeV/c. The left-hand s column corresponds to muon energy deposition in the EM calorimeter, while the right-hand column corresponds to that in the Hadron calorimeter.

The increase in the mean originates from large high energy tails from muon interactions such as e^+e^- pair production and bremsstrahlung processes. The CCFR data [16] show that although the mean energy deposition in the hadron calorimeter increases by 0.8 GeV per 100 GeV/c increase in muon momentum, the momentum dependence of the truncated mean (taken between 20% and 200% of its value) is only 0.2 GeV per 100 GeV/c increase in muon momentum.

We have performed a GEANT simulation of muon energy deposition in the EM and hadron calorimeters for muon momenta in the range 15 to 500 GeV/c. Figure 6.6 shows the momentum dependence of the inefficiency of the EM (upper curve) and Hadron (lower curve) calorimeter minimum ionizing cuts. Figure 6.7 shows the combined EM/Hadron efficiency for the minimum ionizing cuts. The muon energy deposition is a function of the muon momentum, and not transverse momentum. At the highest energies most of the inefficiency originates from the Hadron energy cut of 6 GeV.

Figure 6.6: Efficiency of EM (square symbols) and HAD (diamond symbols) muon ID minimum ionizing cuts (as determined from a GEANT simulation) as a function of the average muon momentum.

Figure 6.7: Efficiency of the combined EM and HAD muon ID minimum ionizing cuts (as determined from a GEANT simulation) as a function of the average muon momentum.
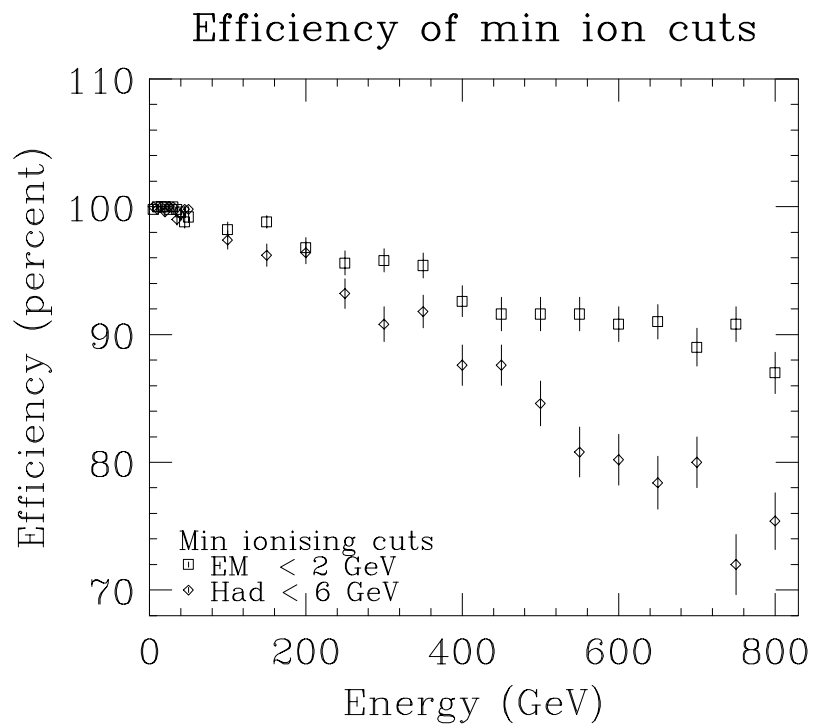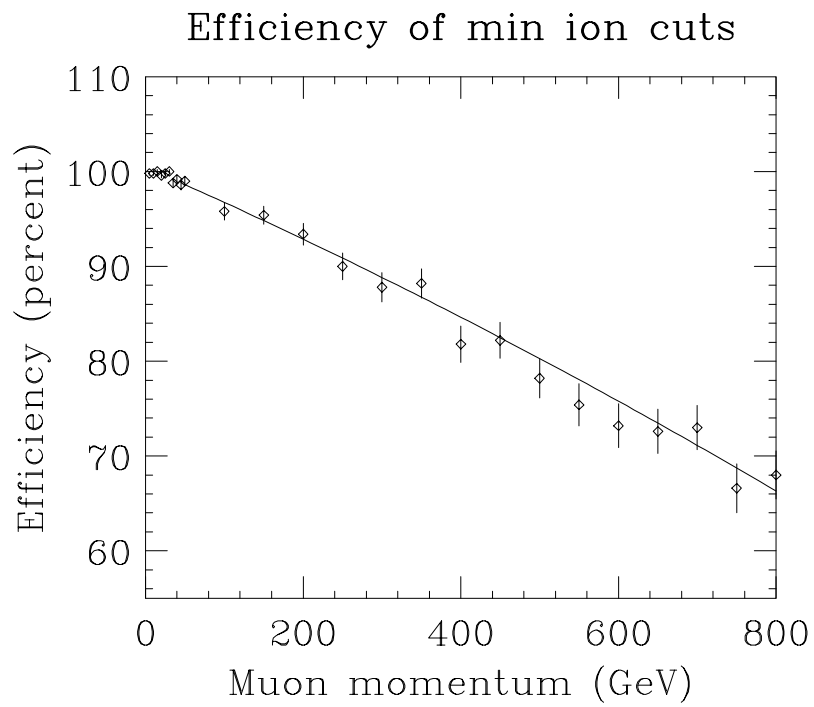
The GEANT simulation yields an combined inefficiency of about 1.5% $\pm$ 1% per muon for 50 GeV/c muons from Z decays. In the CDF data, the inefficiency as determined from events at the Z peak [9] is 4% $\pm$ 0.7%. We expect that in the data the inefficiency will have additional contribution from photon radiation and background from the underlying event which are not included in the muon GEANT simulation.

For high momentum muons, the e^+e^- pair production process becomes very important. For a dimuon invariant mass of 500 GeV/c^2 the average momentum of muons is approximately 267 GeV/c. Figure 6.6 indicates that, for a 267 GeV/c muon, the inefficiency from the EM calorimeter cut is about 4% per muon, and the inefficiency from the HAD calorimeter cut is about 8% per muon. Figure 6.7 indicates that for a 267 GeV/c muon, the combined inefficiency of the EM and Had cuts for 267 GeV/c muons is about 11%, which is approximately 9% larger than the combined efficiency at 50 GeV/c for muons from Z decays.

We have determined the average muon momenta for accepted muons from Z' decays using the same Monte Carlo that was used for the overall acceptance calculations. The average muon momenta are approximately factor of 1.1 times (M/2), where M is the mass of the Z'. Table 6.7 shows the mean muon momenta as a function of the mass of the Z'. Also shown are the efficiency of the minimum ionizing cuts as determined from a fit to the Monte-Carlo data shown in in Figure 6.7 (ϵ_μ), and the efficiency relative to the efficiency at the mass of the Z ($\epsilon_\mu(\text{rel})$), and the overall efficiency for both muons to pass the minimum ionizing cuts relative to the efficiency for two muons at the mass of the Z ($\epsilon_{\mu\mu} = [\epsilon_\mu(\text{rel})]^2$.

Table 6.7: Efficiency of selection using ionisation criteria, as calculated from GEANT

Mass GeV/c^2	Mean P$_\mu$ GeV/c	ϵ_μ	ϵ_μ(rel)	$\epsilon_{\mu\mu}$(rel)
100	55	0.984	1.000	1.000
150	83	0.974	0.990	0.980
200	109	0.964	0.980	0.960
250	136	0.954	0.969	0.940
300	162	0.944	0.959	0.920
350	188	0.933	0.949	0.900
400	213	0.923	0.938	0.880
450	239	0.913	0.928	0.861
500	264	0.903	0.918	0.842
550	288	0.893	0.908	0.824
600	313	0.883	0.897	0.805
650	338	0.873	0.887	0.787
700	362	0.863	0.877	0.769
750	385	0.853	0.866	0.751

6.2.1 Comparison with the CCFR hadron calorimeter

An extensive study of the energy deposition of muons in an iron-scintillator calorimeter was performed by the CCFR collaboration [16]. The CDF hadron calorimeter is constructed of 32 2.5cm steel plates, each followed by a scintillation counter for a total of 0.8 meters of iron. The CCFR calorimeter is composed of 80 10cm steel plates, each followed by a scintillation counter. We have obtained data from the CCFR collaboration in which the muon energy deposition in 1 meter sections (10 CCFR counters) was investigated. The calibration of the CCFR detector for hadrons is 0.211 GeV per minimum ionizing particle per counter. The most probable energy value for the energy deposition of a 45 GeV/c muon in 10 CCFR counters is 2.19 GeV, and the truncated mean energy deposition is 2.48 GeV. Therefore, a 1 meter section of the CCFR calorimeter is similar to the CDF 0.8m hadron calorimeter in terms of response to muons.

Figure 6.8 shows the comparison of muon energy deposition for 50 GeV and 400 GeV muons from CCFR data and using GEANT CDF simulation. The left-hand column corresponds to muon energy deposition at 50 GeV/c, while the right-hand column corresponds to the energy deposition at 400 GeV/c.
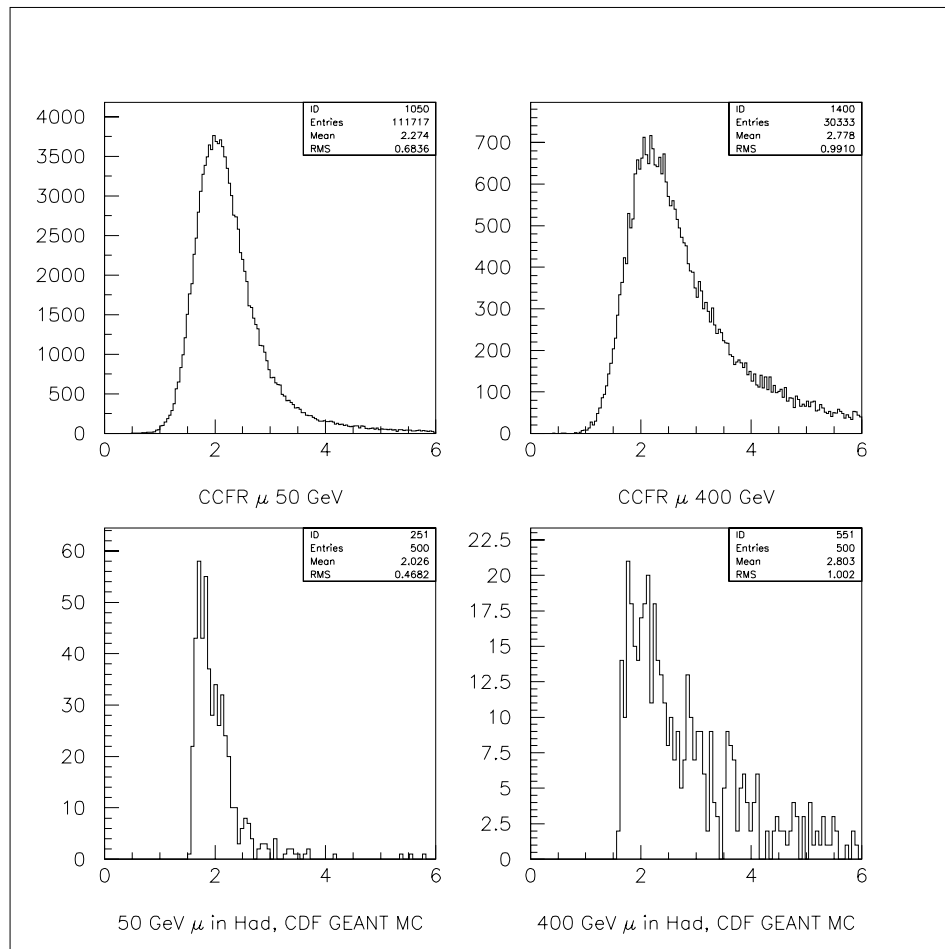
Figure 6.8: Comparison of muon energy depositions for 50 GeV and 400 GeV muons from CCFR data and using GEANT CDF simulation. The left-hand side column correspond to the muon energy depositions at 50 GeV/c, while the right-hand side column corresponds to the energy depositions at 400 GeV/c.

Efficiency of min ion :CCFR
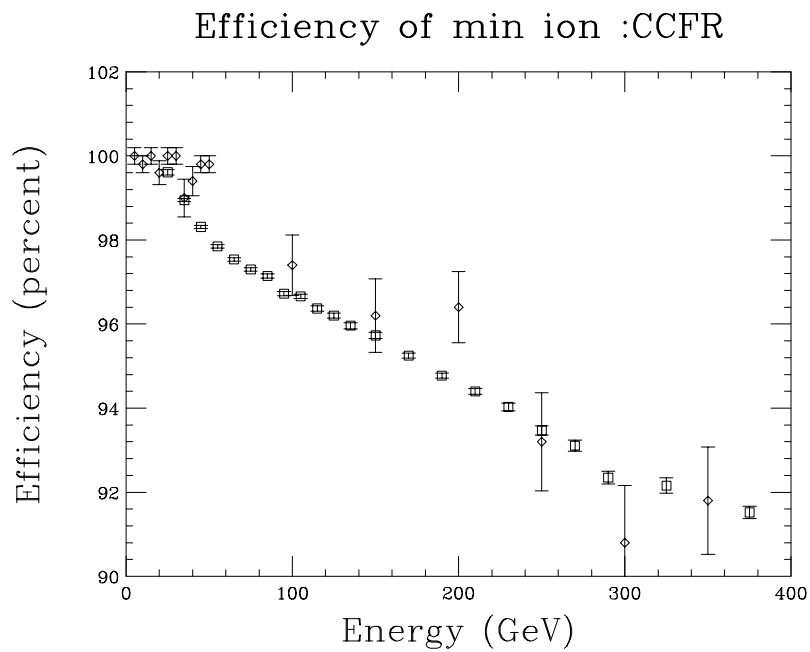
Figure 6.9: The CCFR data (open squares) for the fraction of muons that deposit less than 6 GeV in a 1 meter Fe section of the CCFR calorimeter as a function of muon momentum from 15 to 300 GeV/c. Also shown are the results from a GEANT simulation of the 0.8 m Fe hadron calorimeter of CDF (open diamonds).

Figure 6.9 shows the CCFR data (open squares) for the fraction of muons that deposit less than 6 GeV in a 1 meter section of the CCFR calorimeter as a function of muon momenta in the range 15 to 300 GeV/c. Also shown (open diamonds) is the same fraction as calculated from a GEANT simulation of the CDF detector. The agreement between the CCFR data and GEANT simulation of the CDF detector supports the use of a GEANT simulation in determining the corresponding efficiencies for the CDF hadron calorimeter. We are currently redoing the GEANT comparison by running the simulation for the exact geometry of the CCFR detector.

6.3 Overall Efficiency from Monte-Carlo

In addition to the identification cuts for the muons, the geometrical acceptance needs to be calculated. This simulates effects due to the finite detector coverage in η-ϕ, cuts on kinematic variables like P_t and the η_{CTC} cut of 1.2.

To compute the geometrical acceptance a simple Monte-Carlo program is used [14] with the appropriate smearing in detector variables (due to detector effects), as was used in the previous Z' analysis for 1988-1989 data [11]. Z' events were generated in a range of masses from 90 to 500 GeV/c^2, with the CTEQ2L parton distribution function, and these particles are allowed to decay to dimuons according to theory. We note that the generator that simulated the process, $q\bar{q} \rightarrow Z' \rightarrow \mu\mu$, contained contributions to leading order in α_S, higher order contributions to this process were approximated by the inclusion of a K-factor and the p_T distribution was modeled after the observed Z^0 p_T distribution measured by CDF [13].

The momentum of each muon is smeared by the resolution function of the tracking detector (CTC) by the formula:

$$\frac{1}{P_t^{smr}} = \frac{1}{P_t^{unsmr}} + \Delta \times Gauss \qquad (6.3.6)$$

where Gauss is a random number generated by a Gaussian function with a unit standard deviation. Here Δ represents the resolution of the detector, and is given by

$$\Delta = 0.0008 \ GeV^{-1} \ (\text{forRun 1A data})$$

$$\text{and} \ \ \Delta = 0.00112 \ GeV^{-1} \ (\text{for Run 1B data})$$

$$(6.3.7)$$

The resolution is worse in Run 1B due to higher luminosity and consequently a larger number of hits in the detector leading to a deteriorating quality of the track reconstruction.

The events are simulated through the detector and are accepted or rejected depending on whether they satisfy the cuts. The effect of the detector cuts and the trigger were implemented probabilistically, according the calculated efficiencies.

An additional complication in Run 1B was the problem of prescaling of one of the triggers. This was corrected for by modelling the trigger in the simulation.

Figure 6.3 shows the overall efficiency as a function of $\mu\mu$ invariant mass. The dimuon acceptance increases as a function of invariant mass until it reaches a value of approximately 20% at very high invariant mass.

CDF PRELIMINARY
$Z' --> \mu\mu$
Overall Acceptance*Efficiency
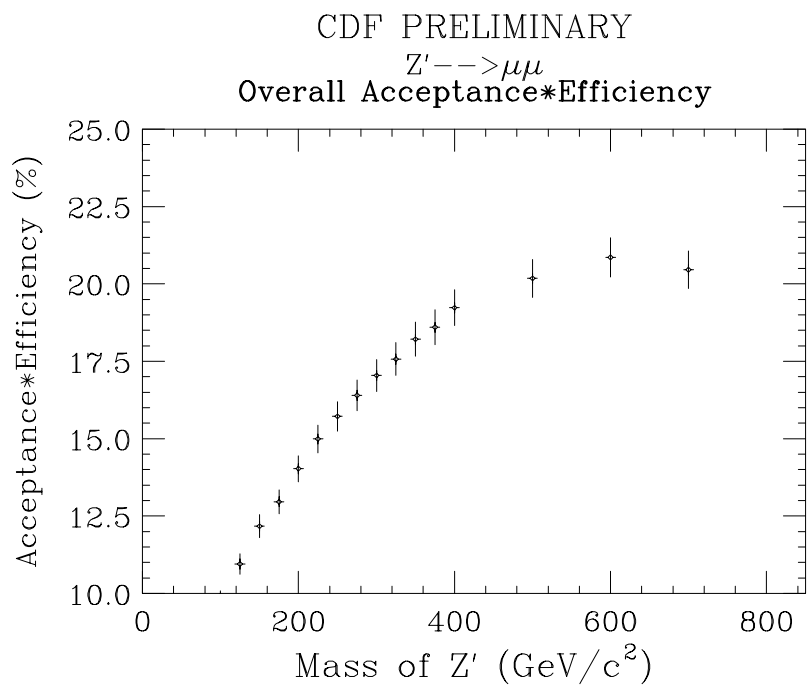
Figure 6.10: Acceptance*Efficiency of the detector to dimuons as a function of the invariant mass of the Z' for the combined Run 1A and Run 1B data. Acceptance rises to reach approximately 20% for very high masses.

Chapter 7

Comparison with Drell-Yan

One of the major backgrounds for this analysis is the standard model Drell-Yan process ($q\bar{q} \to Z^*, \gamma^* \to l\bar{l}$) of the production of dimuon pairs. This type of background cannot be eliminated by kinematic cuts as these events are physically indistinguishable from Z' events. Therefore, this background is estimated from a Monte-Carlo and used as an input in the calculation of limits.

We use the same Monte-Carlo for the estimation of Drell-Yan backgrounds as was used to calculate the acceptance.

The cross-section for the Drell-Yan process is given by equation 1.2.2 with terms only for the Z and the photon. There is an event generator for Drell-Yan events followed by a simple detector simulation. The event generator generates events based on the theoretical Drell-Yan cross-section and the dilepton momenta are stored into a file. A second detector simulation reads in the detector momenta and simulates the event. The virtual boson is given a random P_t-boost weighted by the 1988/89 CDF measured P_t distribution of Z bosons [13]. The dilepton momenta are then transformed

back to the laboratory frame and these are smeared with the resolution of the tracking detector (CTC). The events are then propagated (simulated) through the detector and only those events that reconstructed in the detector are selected to represent real data. The path of the event through the detector is simulated to correspond to all detector elements and materials as are in the real experiment. We then obtain the distribution of events in invariant mass for the selected simulated events. This distribution is then normalised (scaled) so that the number of events in the Monte-Carlo is equal to the number of events in the data in the Z mass region. This scaling to the Z cross section reduces the sensitivity to both experimental and theoretical systematic uncertainties. The experimental uncertainties include uncertainties in the efficiencies, acceptance, and overall luminosity. The theoretical uncertainties include the uncertainties in the parton distributions, and higher order QCD corrections to the cross sections and kinematic distributions.

In the following table we show the number of events as a function of the invariant mass.

The comparison between the data and the Monte-Carlo is also shown in figure 7
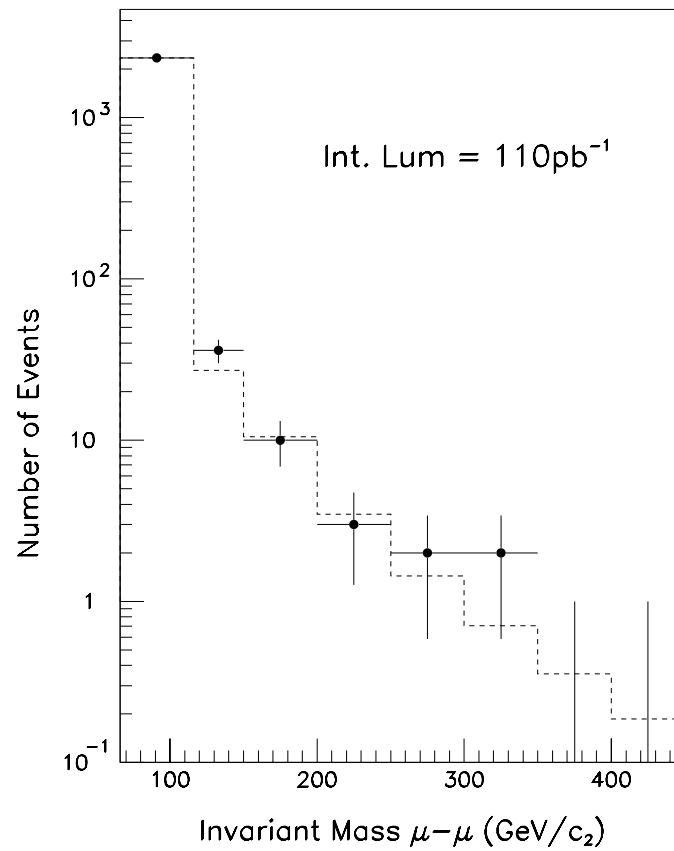
Figure 7.1: The number of events predicted in in a mass-bin Monte-Carlo versus the number of events observed in the data. The dotted histogram represents the Monte-Carlo while the solid dots represent the data.

Table 7.1: Number of events expected in normalised DY-prediction vs observed number in the data as a function of Invariant Mass of the dimuons

Mass > (GeV)	Run1A pred/data	Run1B pred/data	Run1A + Run1B pred/data
150	2.75/3	13.76/14	16.51/17
200	1.04/1	5.20/6	6.24/7
250	0.47/0	2.38/4	2.85/4
300	0.24/0	1.21/2	1.45/2
350	0.12/0	0.64/0	0.76/0
400	0.075/0	0.36/0	0.43/0
450	0.042/0	0.20/0	0.24/0
500	0.023/0	0.12/0	0.14/0
550	0.013/0	0.070/0	0.083/0
600	0.0076/0	0.041/0	0.049/0
650	0.0042/0	0.024/0	0.028/0
700	0.0020/0	0.0125/0	0.0145/0
750	0.0008/0	0.0051/0	0.0059/0

Chapter 8

Limits Using Dimuon Data

8.1 Procedure for setting limits

In order to set limits on the production of new neutral heavy gauge bosons, the invariant

mass distribution in the data is compared to the sum of the Monte-Carlo for Z' pro-

duction and the Z + Drell-Yan (Z + DY) continuum. The production of a boson yields

a peak in the invariant dilepton mass distribution. The Monte-Carlo for a particular

model Z' at a certain mass yields the expected number of events from the theoretical

cross-section and including the effects of acceptance and efficiencies. In general, if the

number of expected events is μ and the number of observed events is N then a 95%

Confidence Limit (C.L.) can be obtained from the likelihood function. For the case of

statistical uncertainty this is given by the Poisson distribution:

$$Lik(N,\mu) = \frac{\mu^N}{N!}e^{-\mu} \tag{8.1.1}$$

Using this likelihood function, a 95% CL is set by requiring that μ satisfy the constraint:

$$0.95 = \int_0^{\mu_{lim}} d\mu \, \frac{\mu^N}{N!} e^{-\mu} \tag{8.1.2}$$

The Poisson distribution yields $\mu_{lim} = 3.0$ for $N = 0$.

For the case when background events from other processes are expected (e.g. DY production) , we compare the data in each mass bin (i) to the sum of the Z' Monte-Carlo expectation and the background (Z + DY continuum) to determine the likelihood function.

$$Lik(\mu_i) = (Normfac) \times \prod_{i=bins} \frac{\mu_i^N}{N!} e^{-\mu_i} \tag{8.1.3}$$

where the product over the index i runs over different mass bins. This likelihood function is just a sum over products of likelihood in each bin.

The quantity μ_i is given by :

$$\mu_i = ZDY_i + \alpha \times Z'_i \tag{8.1.4}$$

Since the μ_i are constrained by the equation 8.1.4 the quantities μ_i are no longer independent, and the likelihood is a function of a single parameter α. The quantity α

is the level of the Z' content in the data with respect to the prediction from the model.

The quantity $Normfac$ is determined by the requirement that the likelihood function

be normalised to 1.0, i.e.,

$$1.0 = \int_0^\infty d\alpha \ Lik(\alpha) \qquad (8.1.5)$$

As described below, the likelihood function falls off rapidly as a function of α, and

the integration need not be carried to large values of α.

The Monte-Carlo Z + DY prediction is normalised to the data in the region of the

Z mass (66 $GeV < M_{\mu\mu} < 116 \ GeV$).

In other words we require that,

$$\sum_i Data_i = f \sum_i ZDY_i \qquad (8.1.6)$$

where, the sum on the index i runs only over the bins that are in the Z mass region.

The quantity f is close to 1.0 if all the experimental effects are properly simulated

and if the theoretical Z cross section agrees with the data:

$$f = \frac{\sum_i Data_i}{\sum_i ZDY_i} \qquad (8.1.7)$$

Deviations from 1.0 originate from any remaining small experimental and theoretical

uncertainties. As mentioned earlier, the experimental systematic uncertainties include uncertainties in efficiencies, acceptance, and luminosity determinations. The theoretical uncertainties include knowledge of parton distributions which are derived from other experiments (i.e. proton structure functions), and higher order QCD corrections to the overall cross section and distributions.

Equation 8.1.4 is rewritten as:

$$\mu_i = f \times ZDY_i + f\,\alpha \times Z'_i \tag{8.1.8}$$

The likelihood function defined in eqn 8.1.3 is now calculated as before. However the bins that are in the Z mass region (66 GeV < $M_{\mu\mu}$ < 116 GeV) are not included in the product.

The 95% Confidence level limits are determined by the requirement that α_{95} be determined by:

$$0.95 = \int_0^{\alpha_{95}} d\alpha\, Lik(\alpha) \tag{8.1.9}$$

The 95% CL limit on the number of Z' events is N_{95}, given by:

$$N_{95} = \alpha_{95}\, f \times \sum_i Z'_i \tag{8.1.10}$$

where the sum on the index i runs over all the bins above the Z mass region ($M_{\mu\mu} > 116~GeV$).

The limit on the cross-section times branching ratio, $\sigma \times Br$, is given by,

$$\sigma \times Br(95\%C.L.) = \frac{N_{95}}{f \times A \times Lum} \qquad (8.1.11)$$

where A is the overall acceptance times efficiency of the selection cuts given by

$$A = \frac{\sum_i Z'_i}{Ntot_{MC}}, \qquad (8.1.12)$$

where Lum is the integrated luminosity of the data sample, and $Ntot_{MC}$ is the total number of generated Monte-Carlo Z' events.

8.2   Limits on the data

Figure 8.1 shows an expected likelihood distribution from the combined Run 1A and 1B data for a Z' of mass 300 GeV.

The 95% CL limit on this likelihood is given by α_{lim} such that the upper shaded region of the likelihood function (above this value of α) corresponds to 5% integrated likelihood.

Figure 8.2 shows the 95% Confidence Level curve on the cross-section times branching ratio to dimuons for the production and decay of a Z' boson for the reference model
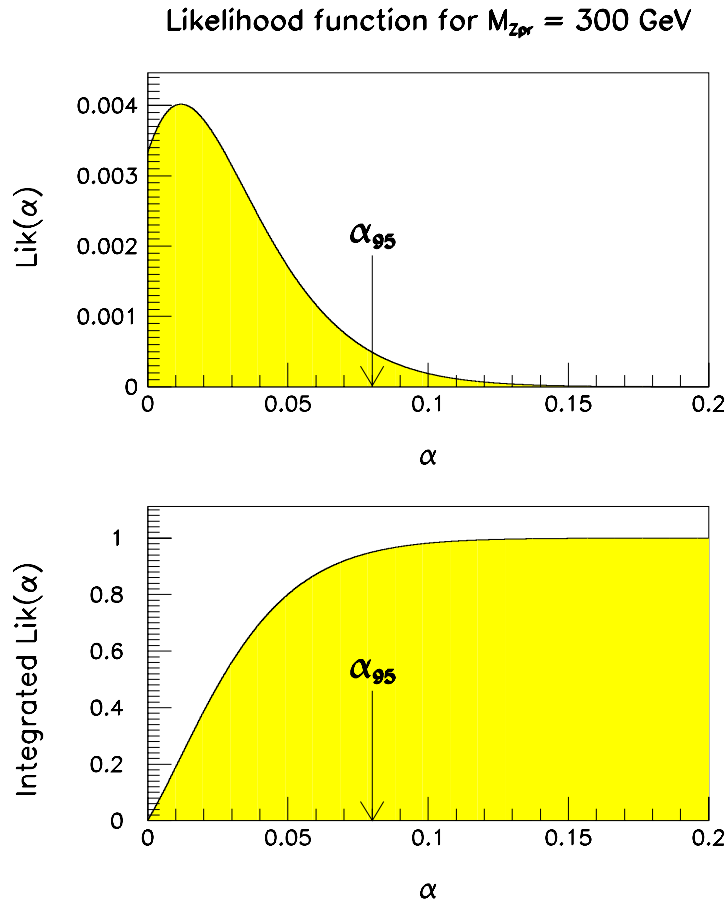
Figure 8.1: Likelihood function, $Lik(\alpha)$, from the fit to a Z' of mass 300 GeV for Run 1A and Run 1B data. The 95% C.L. on α is shown in the figure.

(with standard couplings). The intersection of the limit curve with the function describing the expected theoretical cross section as a function of the Z' mass yields the experimental mass limit on the Z' mass within this model. For the reference model with standard couplings, the corresponding mass limit using the dimuon data is 570 GeV. A better limit can be obtained when combining both electrons and dimuons channels, as described in the next chapter

Several other interesting theoretical models which predict Z' bosons have also been

investigated.

Most of these models arise from an extra $U(1)$ symmetry left over from superstring theories that describe the behaviour of matter at a very high scale (like the Planck scale).

Figure 8.3 shows the 95% CL limits on the cross-section times branching ratio to dimuons of the Z' boson compared to the expectations of the cross sections for various theoretical models. The solid line is the curve expected from theory in the case of the Z' decaying to known fermions only. The dashed line is the case when all decay modes including supersymmetric decay modes are considered.

The corresponding exclusion limits for each of these models are shown in Table 8.1.

Table 8.1: 95% CL limits on the mass of a Z' in different models using Run 1A, Run 1B and combined dimuon data.

Zprime model	Run 1A (18.8 pb^{-1}) (GeV)	Run 1B (88.6 pb^{-1}) (GeV)	Combined (107.4 pb^{-1}) (GeV)
Z_{SM}	440	575	590
Z_χ	360	485	500
Z	350	475	495
Z_η	375	500	520
Z_{LR}	380	510	530
Z_I	335	460	480
Z_{ALRM}	360	480	500

8.3   Effect of systematics

The effect of systematic uncertainties on the limits maybe easily incorporated by introducing a gaussian uncertainty (or smearing) into the variables that go into calculating

the expected number of Z' in each mass bin. Since we are normalizing data and theory in the region of the Z mass, many of these systematic uncertainties cancel out. The major systematic uncertainties originate in the ratio of Z' to Z production from mass dependent differences in acceptance, efficiency, P_t distribution of the gauge boson, structure functions, and the statistical error in f arising from the normalization in the Z region.

The contribution from the uncertainty in the luminosity, errors in acceptance and efficiency, and to first order that from the structure functions do not change significantly with mass and thus, largely cancel out when the data and the Monte-Carlo are normalised to each other. Normalization errors coming from structure functions are larger than the statistical error that we get at the Z, and hence it is prudent to normalised the data to the Z.

Table 8.2 shows the systematics in the data, calculated for different masses.

Table 8.2: Systematic effects in the determination of acceptance

Mass (GeV)	Syst (in %)
150	2.9
200	2.8
500	2.7
700	2.6

We note that the overall systematic uncertainty (excluding the luminosity) is independent of the mass of the Z', and will henceforth use a number of 3%.

The uncertainty in the efficiency translates into a systematic uncertainty in the quantity μ in equation 8.1.1, which is the expected number of events in each mass bin. The new likelihood function is now, for each bin, the convolution of the previous

likelihood function with the systematic uncertainties folded in as gaussians.

$$Lik(N,\mu) = \int dA\ dL\ ...\ \frac{\mu(A,L,..)^N}{N!}e^{-\mu(A,L,..)} \times Gauss(A,A_0,\delta A) \times Gauss(L,L_0,\delta L)$$

$$(8.3.13)$$

where the quantities A, L are parameters on which the quantity μ depends, and Gauss

is the gaussian probability function defined by:

$$Gauss(a,a_0,\delta a) = \frac{1}{\delta a\sqrt{2\pi}}e^{-\frac{(a-a_0)^2}{2(\delta a)^2}} \qquad (8.3.14)$$

where, a is the variable, a_0 is the mean and δa is the width of the Gaussian function.

The integral in equation 8.3.13 is best done by using a Monte-Carlo. For this purpose

the integral is transformed into a form that is suitable for Monte-Carlo integration.

For each variable that is integrated over, we make a transformation, for example for

the variable, L, we write:

$$x = \frac{L}{L_0} \qquad (8.3.15)$$

$$\delta x = \frac{\delta L}{L_0} \qquad (8.3.16)$$

and rewrite the Gaussian function in terms of x. The mean of this function is now

1, and the width is given by δx, which is the fractional systematic uncertainty in the variable L. The integration is also converted to one over the variable x.

The quantity μ is proportional to the variable L, in general, and so we can write:

$$\mu = \mu_0(1 + \delta x) \qquad (8.3.17)$$

These are now put into equation 8.3.13 and then the resulting equation is used to perform the Monte-Carlo calculation.

The effect of systematics was found to change the cross-section limits by less than 2% and, since the mass limits vary only logarithmically with the cross-section, the limits are mostly unaffected by the systematics. This is mostly due to the fact that the predictions are normalized to the observed Z cross section, thus effectively cancelling most of possible systematic uncertainties.
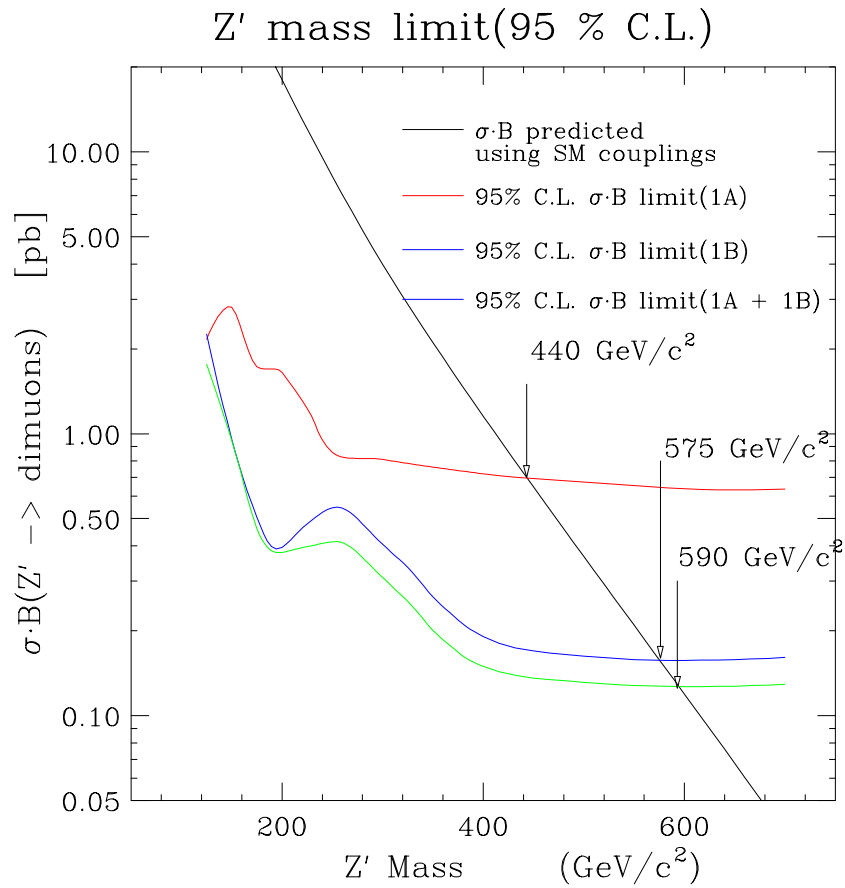
Figure 8.2: 95% CL limits on the cross-section times branching ratio to dimuons for a reference model Z' (with standard couplings) using data from Run 1A and Run 1B, with a total integrated luminosity of 110 pb^{-1}. A better limit can be obtained when combining both electrons and dimuons channels, as described in the next chapter.
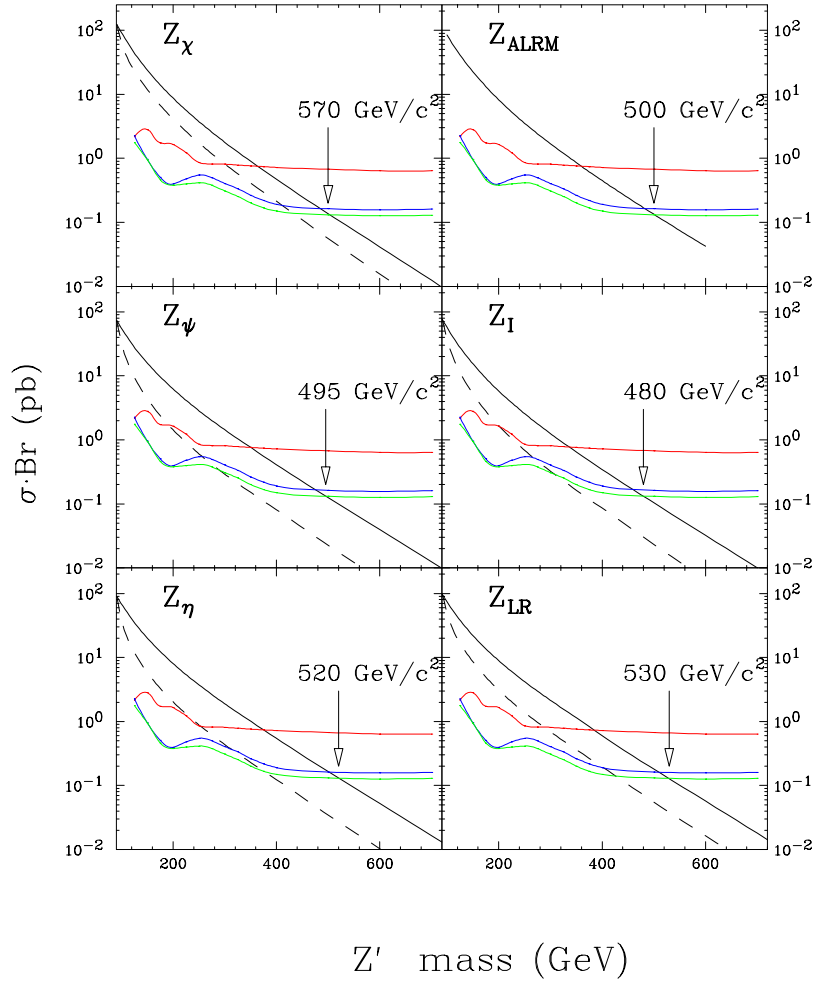
Figure 8.3: 95% CL limits on the cross-section times branching ratio to dimuons for different Z' models using data from Run 1A and Run 1B, with a total integrated luminosity of 110 pb^{-1}. The solid line is the curve expected from theory in the case of the Z' decaying to known fermions only. The dashed line is the case when all decay modes including supersymmetric decay modes are considered. The corresponding limits are given in Table 8.1.

Chapter 9

Limits using dielectron and dimuon data

In this chapter, we will show how we set limits on Z' production and decay using the combined dielectron and dimuon data at CDF. The first section deals with dilepton data from CDF, while in the second section we also discuss how this limit can be extended by using the combined data from CDF and D0, without doing an extended likelihood analysis.

9.1   Limits using dielectron and dimuon data from CDF

The data from dielectrons and dimuons is combined by using a likelihood function that is a direct product of the individual likelihood functions. The dielectron analysis was done by E. Hayashi [19] , at the University of Tsukuba, Japan. In the discussion of how the limits were combined, we will first present a summary of the analysis.

At first we will show the data, the acceptance $\times$ efficiency, the Standard Model Drell-Yan background for both the dimuon and the dielectron cases. At the risk of repetition we will mention in brief the cuts that were applied, the methods used for the determination of the efficiencies, the backgrounds, and the comparison of the data with the Monte-Carlo.

The calorimeters, the Central Tracking Chamber (CTC) and the Muon chambers are the principal detector components used for this search. [8] Data are collected with a multi-level trigger. The electron trigger requires a minimum E_t in the calorimeter with $\approx 100\%$ efficiency. The muon trigger requires a match between a Central Muon Chamber stub and a high P_t track in the CTC with $\approx 90\%$ efficiency.

Candidate events are selected by requiring one "tight" and one "loose" lepton. Dielectron events are required to have one isolated central electron with $E_t > 25$ GeV/c^2 , and $P_t > 13$ GeV/c. The second electron could be detected in the Central or in the Plug region of the detector. Muons are required to be minimum ionizing with $P_t > 20$ GeV/c. One muon is required to be isolated and detected in the Central Muon detector.

We find 7120 dielectron events and 2562 dimuon events. The distribution of these events as a function of invariant mass is shown in Figure 9.1. The highest mass e^+e^- and $\mu^+\mu^-$ events have invariant masses of 511 GeV/c^2 and 320 GeV/c^2 respectively.

Efficiencies of the lepton identification cuts are determined from a sample of dileptons from Z decays. The geometric and kinematic acceptance were determined from a Monte-Carlo sample of Z and Z' events generated at different masses. The overall acceptance (see Fig 9.1) times efficiency rises to a value of 48% for dielectrons and 20% for dimuons at very high Z' invariant mass.
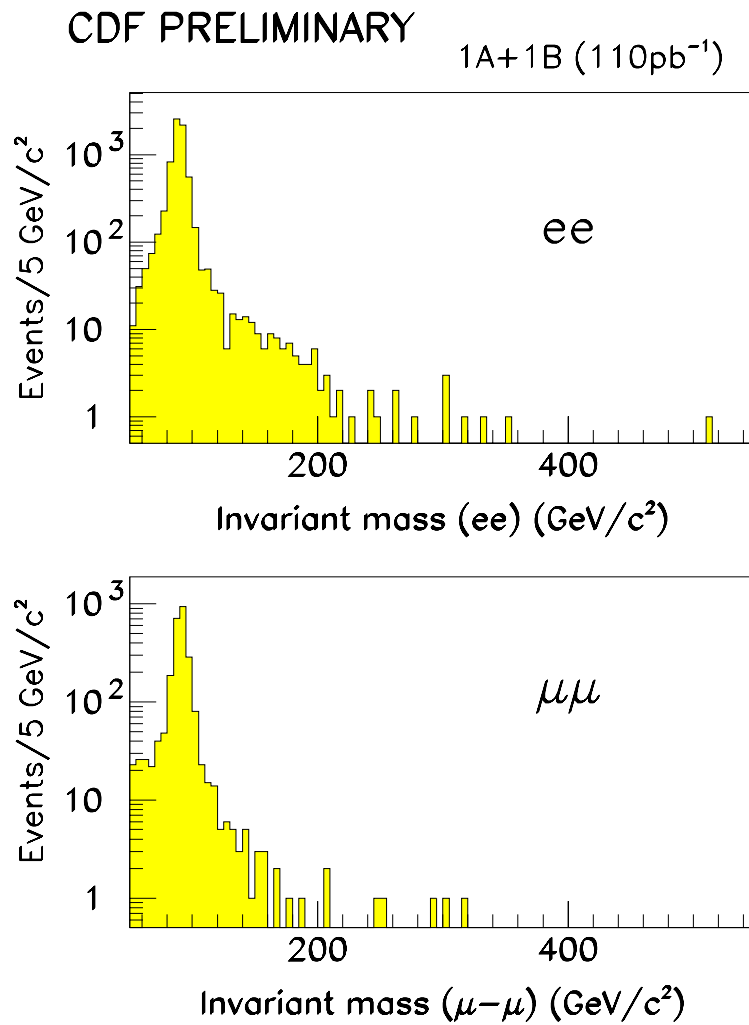
Figure 9.1: Distribution of dilepton events as a function of invariant mass in 110 pb^{-1} of data taken at CDF.

CDF PRELIMINARY

Overall Acceptance*Efficiency
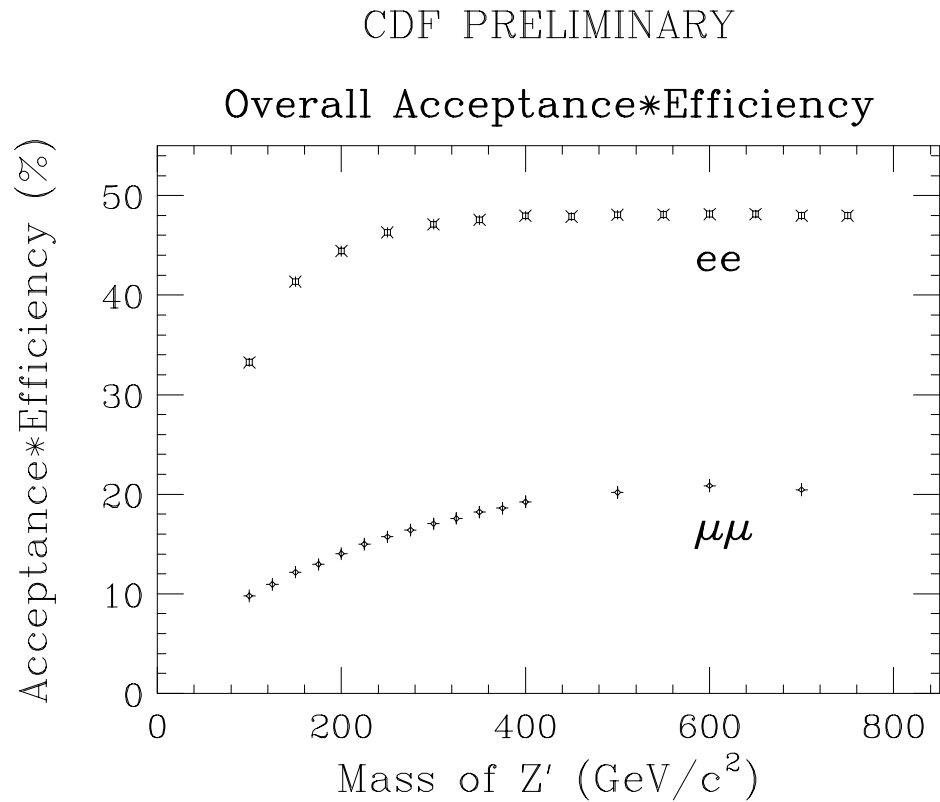
Figure 9.2: Acceptance*Efficiency of the detector to dileptons as a function of the invariant mass of the Z'. Acceptance rises to reach approximately 48% at very high masses for dielectrons and 20% for dimuons.

Mass (GeV)	ee DY + QCD pred/data	$\mu\mu$ DY pred/data
> 150	68.0/70	16.5/17
> 200	21.7/19	6.2/7
> 250	8.1/9	2.8/4
> 300	3.3/6	1.4/2
> 350	1.4/2	0.7/0
> 400	0.7/1	0.4/0
> 450	0.3/1	0.2/0
> 500	0.2/1	0.1/0
> 550	0.1/0	0.0/0
> 600	0.0/0	0.0/0

Table 9.1: Predicted number of events from Drell-Yan and other backgrounds compared with the data.

Figure 9.3: Comparison of dielectron and dimuon data with the Standard Model Z + Drell-Yan Monte-Carlo and expected backgrounds.

Figure 9.3 shows a comparison of the data with the Standard Model expectation and estimated backgrounds. The top figure shows the comparison in the case of the dielectrons while the bottom fig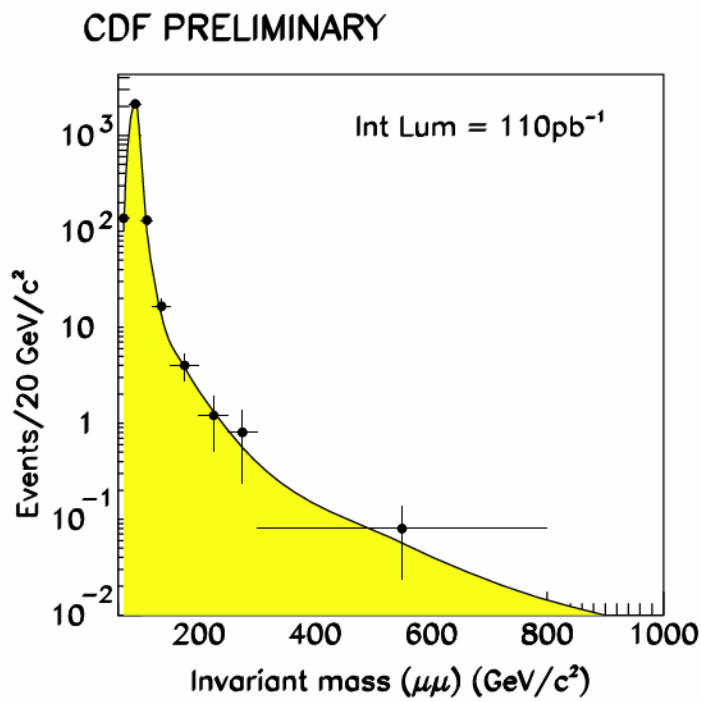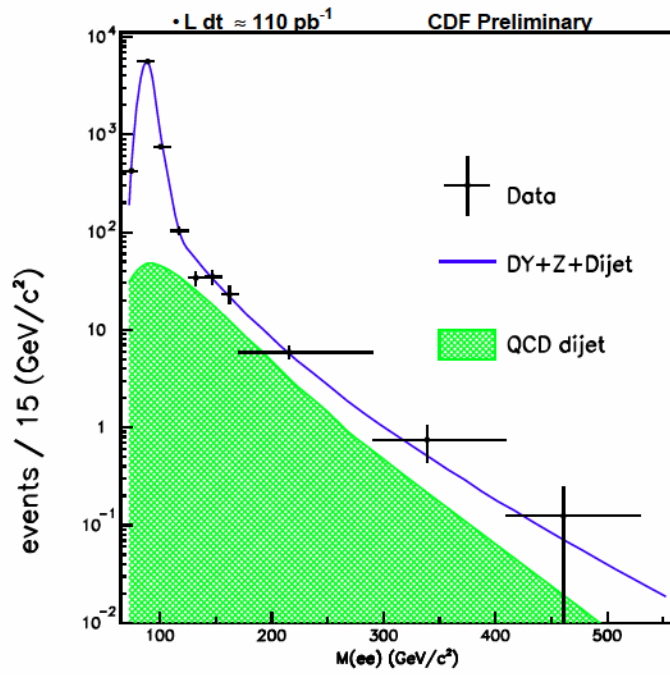ure shows the same comparison in the case of the dimuons. The y-axis in both figures shows the expected number of events in the data, while the x-axis shows the invariant mass. In case of mass bins (above 150 GeV) that have a larger bin width, the number of events is correspondingly scaled to a constant bin width, to reflect the falling cross-section. The data is shown by points with error bars, while the Monte-Carlo is represented by the solid curve. The shaded region on the top plot shows the QCD-dijet background. We find no significant excess in the data (see also Table 9.1).

The Monte-Carlo Drell-Yan backgrounds are separately normalised to have the same number of events in the Z region for each of the channels (for the ee and the $\mu\mu$). This method of normalization of the Monte-Carlo reduces the effect of systematic uncertainties. Systematic errors arising from the choice of structure functions and P_t distributions are less than 3%.

The dielectron and dimuon data are combined by assuming that lepton universality holds for Z' decays. Z' mass limits are obtained by comparing the observed data to a superposition of the Standard Model prediction and the expected distribution from Z' decays using the method of binned likelihood.

Figure 9.4 shows the 95% Confidence Level curve on the cross-section for the production and decay of a Z' boson into dileptons for the Standard model Z'. For this reference case with standard coupling, the combined dimuon and dielectron data set yields a mass limit of 690 GeV.

Figure 9.5 shows the 95% CL limits on the cross-section times branching ratio to

dileptons (dimuon and dielectron cross sections averaged) of the Z' boson compared to

the E_6 and the LR theoretical models.The solid line is the curve expected from theory in

the case of the Z' decaying to known fermions only. The dashed line is the case when all

decay modes including supersymmetric decay modes are considered. The corresponding

limits are given in Table 9.2.

The corresponding exclusion limits for each of these models are shown in Table 9.2.

Table 9.2: 95% CL limits on the mass of a Z' in different models using dimuon, dielectron data separately and the combined limits. The dielectron data was analysed by E. Hayashi, et. al.

Zprime model	Dimuon (110 pb^{-1}) (GeV)	Dielectron (110 pb^{-1}) (GeV)	Combined (ee $+$ $\mu\mu$) (GeV)
Z'_{SM}	590	650	690
Z'_{χ}	500	530	585
Z'	495	520	580
Z'_{η}	520	550	610
Z'_{LR}	530	565	620
Z'_{I}	480	505	555
Z'_{ALRM}	500	525	590

9.2 Limits using data from CDF and D0

Limits have also been set on Z' decaying to dielectrons using ≈ 90 pb^{-1} of data obtained

at the D0 detector at the Tevatron. [28] The limits are expressed as follows:

$$\frac{\sigma \cdot Br(Z' \to ee)}{\sigma \cdot Br(Z^0 \to ee)} \quad \leq \quad 4 \times 10^{-4} \text{ at the 95\% CL}$$

$$\sigma \cdot Br(Z^0 \to ee) \quad = \quad 210 \ pb$$

$$or, \ \sigma \cdot Br(Z' \to ee) \quad \leq \quad 210 \ pb \times 4 \times 10^{-4}$$

$$= \quad 84 fb$$

This should be compared with the 42 fb obtained by the combined CDF data. The combined systematic uncertainty on the CDF data is $\approx 3\%$ while that on the D0 data, at present, is tentatively set at 10%. [28]

In the following discussion, we will suppress the quantity Br (the branching ratio), in fact we will assume that by the term cross-section (σ or σ_{lim}) we refer to the cross-section $\times$ the branching ratio in the appropriate channels. The limiting cross-sections (at very high mass) are defined by: (here we refer to the cross-section times branching ratio to the appropriate channel or channels)

$$\sigma_{lim} \quad = \quad \frac{3.0}{A \times \epsilon \times \int L \ dt}$$

where A, ϵ, $\int L \ dt$ are the acceptance, efficiency and the integrated luminosity respectively, for each detector. We combine the two cross-section limits in the following

manner:

$$\sigma^{comb}_{lim,Z'}(95\% \ CL) = \frac{3.0}{A\epsilon\int L \ dt(CDF) + A\epsilon\int L \ dt(D0)}$$

$$= \frac{3.0}{\frac{3.0}{\sigma_{lim,Z'}(CDF)} + \frac{3.0}{\sigma_{lim,Z'}(D0)}}$$

$$or, \ \frac{1}{\sigma^{comb}_{lim,Z'}} = \frac{1.0}{\sigma_{lim,Z'}(CDF)} + \frac{1.0}{\sigma_{lim,Z'}(D0)}$$

The above expression is now easily tractable for combining several experiments and their systematics (especially based on their acceptances, etc).

$$\sigma^{comb}_{lim,Z'}(95\% \ CL) = \frac{1}{(42 \ fb)^{-1} + (84 \ fb)^{-1}}$$

$$= 28 \ fb$$

We use the 10% tentative systematic error assigned to the D0 measurement, and a 3% systematic error for the CDF measurement. This systematic error in each of these cross-sections is converted into a systematic on the overall cross-section, as follows:

$$\delta\left(\frac{1}{\sigma}\right) = \delta\left(\frac{1}{\sigma_{lim,Z'}(CDF)}\right) \oplus \delta\left(\frac{1}{\sigma_{lim,Z'}(D0)}\right)$$

where the corresponding cross-sections are the limiting cross-sections at very high

masses (M > 700 GeV), and the uncertainties are added in quadrature. The overall
uncertainty comes out to be 6% on the combined measurement. We now convolute a
gaussian with a width of 0.06 and a mean of 1.0 with the Poisson distribution, and use
this to reconstruct the likelihood. We get the 95% CL on the number of events from
this likelihood distribution when the observed number is consistent with 0 events. This
is larger by $\sim$ 2% compared to the number without the systematics, included and so
is the corresponding cross-section. We will neglect the systematics in this calculation.
The limit on $\sigma \times Br(Z' \to l\bar{l})$ without systematics is found to be 28 fb at very high
masses. For the standard model Z' this corresponds to a region M < 740 GeV, which is
excluded at the 95% Confidence Level. For non-standard model Z', the excluded regions
are easily ascertained from the theoretical limit curves. The corresponding mass limits
are extracted from the plots. [30]

The exclusion limits for each of these models are shown in Table 9.3.

Table 9.3: 95% CL limits on the mass of a Z' in different models using dimuon, dielectron
data separately and the combined limits. The dielectron data was analysed by E.
Hayashi, et. al. at CDF. The first 3 columns are for the CDF data, while the last
column is for the combined data from CDF and D0.

Zprime model	ee (GeV)	$\mu\mu$ (GeV)	(ee + $\mu\mu$) (GeV)	(CDF & D0) (GeV)
Z'_{SM}	590	650	690	740
Z'_χ	500	530	585	630
Z'_ψ	495	520	580	630
Z'_η	520	550	610	655
Z'_{LR}	530	565	620	660
Z'_I	480	505	555	610

The above procedure is applicable to many other searches as well, especially ones
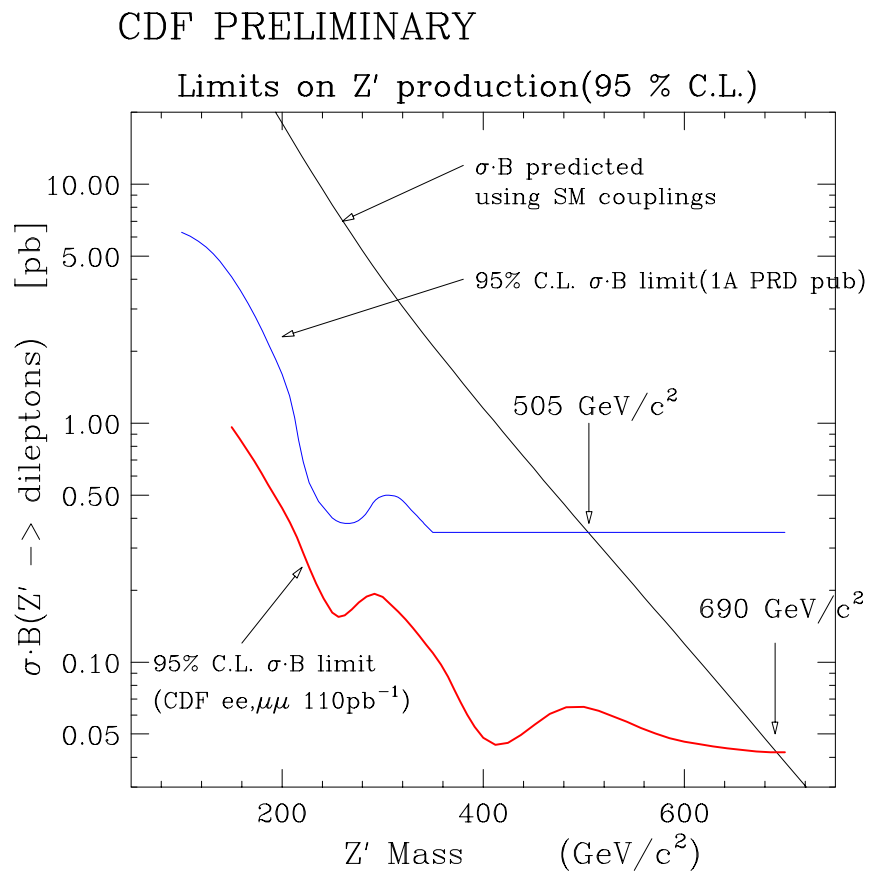where no candidate events have been found.

Figure 9.4: 95% CL limits on the cross-section times branching ratio for a Standard model Z' using dileptons (dielectrons and dimuons averaged) with a total integrated luminosity of 110 pb^{-1}.

Figure 9.5: 95% CL limits on the cross-section times branching ratio for different Z' models using dileptons (dielectron and dimuon data averaged) from Run 1A and Run 1B, with a total integrated luminosity of 110 pb^{-1}. The crosses represent the data points and the solid line joining these points is a smooth curve drawn through the data. The solid line is the curve expected from theory in the case of the Z' decaying to known fermions only. The dashed line is the case when all decay modes including supersymmetric decay modes are considered.
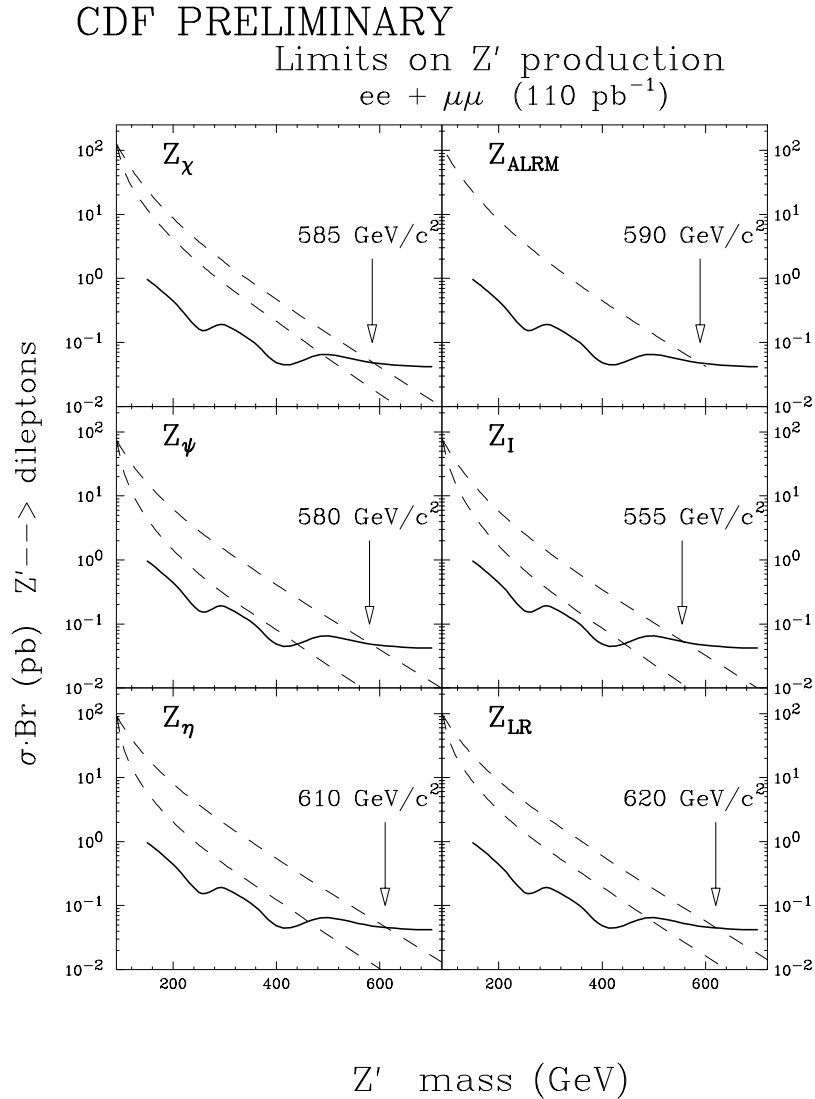
Figure 9.6: 95% CL limits on the cross-section times branching ratio for different Z' models using dileptons (dielectron and dimuon data averaged) from Run 1A and Run 1B, with a total integrated luminosity of 110 pb^{-1}. The crosses represent the data points and the solid line joining these points is a smooth curve drawn through the data. The solid line is the curve expected from theory in the case of the Z' decaying to known fermions only. The dashed line is the case when all decay 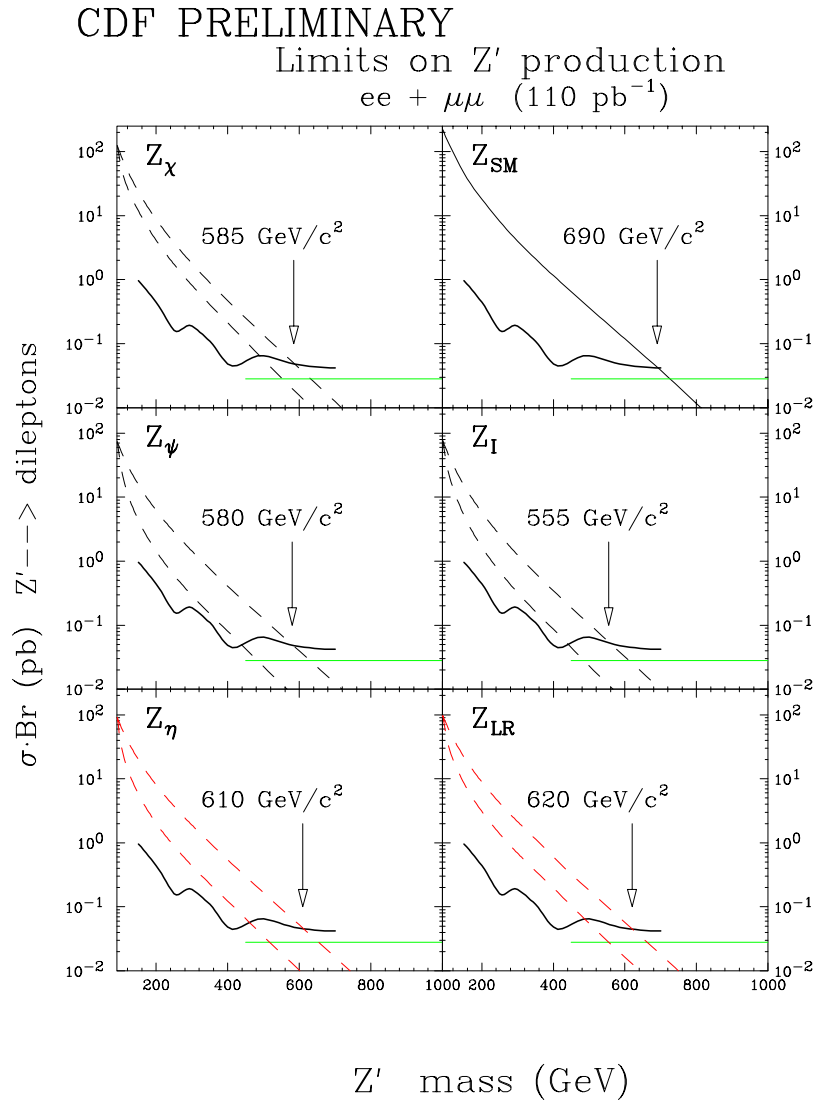modes including supersymmetric decay modes are considered. The corresponding limits are given in Table 9.3. The solid line at the bottom represents the limit on the cross-section from the combined data from CDF and D0.

Chapter 10

Conclusions

The previously published [20] direct search for the production and decay of Z' boson in the dielectron channel (using the run 1A 20 pb^{-1} of data) yielded in a lower limit of 505 GeV on the mass of the boson at the 95% CL assuming standard couplings. In this search, The corresponding limit from the full run 1A and 1B sample (110 pb^{-1}) using the dimuon channel only is 590 GeV. This search combined with the corresponding search in the di-electron channel using the full run 1A and 1B sample (110 pb^{-1}) increases the limit to 690 GeV. These limits are important in constraining new theoretical models within the framework of extended gauge theories. Note that it is not necessary that any new neutral current should have the same coupling to muons as to electrons. Therefore it is important that the search for a neutral current be carried out in all its decay modes, to all possible generations of leptons and quarks.

One of the simplest searches that one could make for an extended gauge theory is to look for an extra neutral vector gauge boson. This is because almost all models that are consistent with the standard model at low energy and and are theoretically promising

contain at least one additional neutral vector gauge boson. Searches for new neutral current interactions will remain one of the most promising fields for testing new physics, apart from searches for supersymmetry and fine tuning the parameters of the standard model.

Current plans at Fermilab are for the CDF and Dzero experiments to upgrade the detectors over then next two years. The Fermilab collider run II, planned to begin in 1999, will accumulate data with a total integrated luminosity of 2000 pb^{-1} ($= 2$ fb^{-1}), at an increased center of mass energy of 2 TeV. This sample would be sensitive to the production of a Z' boson with standard coupling up to a mass of 1.0 TeV. The sensitivity increases to 1.3 TeV for a sample of 30 fb^{-1}, as discussed in the TeV 2000 Fermilab report [21] about future physics opportunities at Fermilab with high luminosity. Sensitivity to higher Z' mass is also expected when a higher energy and high luminosity machine, the Large Hadron Collider is constructed at the CERN facility in Geneva, Switzerland.

Appendix A

A List of Acronyms

- **BBC**

  Beam-beam counter ADCs and TDCs (Phototubes read out by CAMAC/NIM logic)

- **Beam-Beam crossing**

  A beam-beam crossing occurs at the moment when a bunch of antiprotons and a bunch of protons cross at the center of the detector.

- **CCR**

  Central crack gas chamber (Ar/CO2 gas chamber read out by SCA cards) These chambers are located in front of the η cracks of the calorimeters. These are useful in reading out any energy that is deposited in the crack region by particles.

- **CEM**

  Central E-M calorimeter

- **CES**

Central E-M strip/wire gas chamber (Ar/CO2 gas chamber)

- **CHA**

  Central hadron calorimeter

- **CMP**

  Central muon wall chamber upgrade

- **CMU**

  Central muon chamber (Ar/CO2 gas chamber

- **CMX**

  Central muon wall chamber extension

- **CMIO**

  Not all muons passing through the Muon chambers will leave a stub since the muon chamber is not 100% efficient. Therefore, in order to make certain that one doesn't lose interesting events, very high transverse momentum CTC tracks are necessarily put into a bank as a possible muon candidate.

- **CMUO**

  Central Muon data is kept in a data structure known as a bank, on the computer. The particle (or it could be fake electronic noise) has to satisfy certain criteria before it is stored into a bank. In this analysis, any high transverse momentum track (CTC) that is close to a muon stub is stored into a CMUO bank.

- **CPR**

  Central pre-radiator gas chamber (Ar/CO2 gas chamber)

- **CSP**

  Central muon wall scintillator upgrade

- **CSX**

  Central muon wall scintillator extension

- **CTC**

  Central tracking chamber

- **ELES**

  This bank contains the information about the electrons that deposit energy in the Electromagnetic calorimeter. Data stored in the bank include the amount of energy deposited, location of the energy cluster, and tracks that spatially extrapolate to the location of the energy cluster.

- **EM**

  Electro-magnetic (usually as applied to a calorimeter)

- **FEM**

  Forward E-M gas calorimeter (Ar/Eth gas chamber)

- **FHA**

  Forward hadron gas calorimeter (Ar/Eth gas chamber)

- **FMU**

  Forward muon gas chamber

- **Fiducial**

  Different regions of the CDF detector are sensitive to different types of particles.

The sensitive portion of a detector for a particular type of particle is referred to as the fiducial region. These requirements are mostly geometric.

- **FRED**

  (FASTBUS card) Final Readout Event Decision (apocryphally, rumor has it FRED does not stand for anything)—a card which gathers the final Level 1 and Level 2 information from the trigger system and communicates with the TS; it comes in two flavors, CDF FRED (actually a collection of several FASTBUS cards) which allows for up to 12 Level 1 inputs on its front panel, and AFRED (autonomous FRED), which allows for up to 15 Level 1 inputs (and bypasses Level 2) in the AFRED patch panel

- **GEANT**

  GEANT is a detector simulation program that was written at CERN. [31] It models the detector geometry and then simulates the passage of a particle through the detector and the energy deposited in the detector is calculated using the known physics processes.

- **Integrated Luminosity**

  The integrated luminosity is a measure of the total number of collisions that have occurred during a run. The rate of collisions is proportional to the product of the proton and the antiproton fluxes, and is measured by the beam-beam counters (BBC). This rate is characterised by the instantaneous luminosity. The time integral of this luminosity over the entire run is the integrated luminosity.

- **Minimum Ionising Particle**

The energy that is deposited by energetic charged particles travelling at relativistic velocities is given by the Bethe-Bloch formula [18]. It predicts that as the particle becomes relativistic, the energy deposited per unit length reaches a minimum value at around $\gamma = 3.2$. Most relativistic particles lose energy close to this minimum rate and are known as minimum ionizing particles.

- **Muon Stub**

  When a muon crosses a muon chamber (which is essentially a drift chamber with wires in it), it deposits energy through ionisation. This charge is collected and the geometric position of the muon is fairly well known from the spatial position of the "hit" or the location where the charge is collected. Using several such drift chambers arranged in a series one gets several such "hits", and these form a small segment of a track. This is referred to as a muon stub.

- **PMT**

  PhotoMultiplier Tube (*a.k.a.*, phototube)

- **RABBIT**

  Redundant Analog-Based Backplane InsTrumentation—a system of custom crates with custom backplanes and custom cards used as the front-end readout for CDF calorimetry

- **SVX**

  (component; obsolete) Silicon vertex detector; now replaced by other components in SVX database as opposed to CALIB database (Silicon vertex chamber read out by port cards/SVX FASTBUS sequencers)

- **Track**

  Fast moving charged particles deposit energy in the Central Tracking Chamber, and this charge is collected on sense wires. The geometric location of the wire where the charge is deposited electronically displayed as a "hit". Several such hits are reconstructed together to form a track of a charged particle. In particular this is a complex pattern recognition process.

- **Trigger**

  Triggering is the method that is adopted to separate "interesting" events from other "uninteresting" events during online data taking. It requires the event to satisfy certain criteria (which is decided by the physics processes that one wants to study)..before it is read out.

Bibliography

[1] E. Fermi, Z. Physik **88** , 161 (1934).

[2] F. J. Hassert, et al, Phys. Lett. **46B**, 138 (1973), Nucl. Phys. **B73**, 1 (1974).

[3] G. Arnison, et al, Phys. Lett. **122B**, 103 (1983), Phys. Lett. **126B**, 398 (1983).

[4] M. Banner, et al, Phys. Lett. **122B**, 476 (1983).

[5] F. del Aguila, M. Quiros and F. Zwirner, *Nucl. Phys.* B **287**, 457 (1987),F. Feruglio,L. Maiani and A. Masiero, *Phys. Lett.* B **233**, 512 (1989)

[6] Salam, A., Nobel Symposium #8, edited by W. Svartholm (1968).

[7] R.P. Feynman, *Photon-Hadron Interactions*, Addison Wesley (1972).

[8] For a detailed description of the CDF detector see F. Abe *et al*,*Nucl. Instrum. Methods* A **271**, 387 (1988) and references therein.

[9] W. Badgett, Ph. D. Thesis, University of Michigan, Measurement of R(W/Z) from muons (1992).

[10] The author is grateful to Dr. M. Krasberg, currently at the University of Michigan, who made the dimuon dataset for Run 1A.

[11] F. Abe *et. al.*,Phys. Rev. Lett. **68**, 1463 (1992)

[12] F. Abe *et. al.*,Phys. Rev. Lett. **69**, 28 (1992).

[13] F. Abe *et. al.*, Phys. Rev. Lett. **67**, 2937 (1991)

[14] Claudio Campagnari's Toy MC, CDF internal note 1025

[15] F. Abe *et. al.*, Phys. Rev. **D49** (Jan 1994)

[16] Muon interaction in iron in CCFR detector: P. S. Auchincloss et al. (CCFR) Nucl. Inst. Meth. **A343**,463(1994).

[17] Phil Schlabach, CDF Note 2896, "Probing the Central Calorimeter Energy Scale with Run 0 Muons", Dec. 9, 1994.

[18] Particle Properties Data Booklet,June 1992 published by the American Institute of Physics, p. 114, Review of Particle Properties, Phys. Rev. **D45**, Part 2 (June 1992)

[19] E. Hayashi, Ph. D. Thesis, University of Tsukuba, Japan (to be published).

[20] F. Abe *et. al.*, Phys. Rev. **D51**,951 (1995)

[21] TEV 2000, Fermilab-Pub/96/082,page 184. D. Amidei and R. Brock editors, April 1996.

[22] J. D. Bjorken and S. D. Drell, Relativistic Quantum Fields (McGraw-Hill, New York, 1965)

[23] E. Eichten, I. Hinchliffe, K. Lane and C. Quigg, Rev. Mod. Phys. 56(1984) 579.

Other General References are:

[24] M. Pillai, et. al., CDF Note 2910, A search for Z' decaying to $\mu\mu$ using Run 1A data and a first look at Run 1B data, Feb 1995

[25] M. Pillai, et. al., CDF Note 3020, A search for Z' decaying to $\mu\mu$ from Run 1A and Run 1B: An Update M. Pillai, et. al, CDF Note 3548, A search for Z' decaying to $\mu\mu$ from Run 1A and Run 1B

[26] B. Kim, et. al.,CDF Note 3510, Z and Drell-Yan cross-section measurement in the dimuon channel

[27] M. Pillai, et. al.,CDF Note 3598, Limits on a Z' decaying to dileptons from Run 1A and Run 1B data

[28] Talk delivered by C. Gerber at the DPF conference in Minneapolis, Minnesota (August 1996) in session 1.b.2

[29] The D0 Z cross-section is taken to be 210 pb (Cecilia Gerber, private communications)

[30] M. Pillai, E. Hayashi, K. Maeshima, C. Gross-Pilcher, P. de Barbaro, A. Bodek, B. Kim, W. Sakumoto, et. al., DPF proceedings (1996), to be published.

[31] The GEANT program is written by CERN. Several groups have contributed to it. The GEANT team at CERN consists of R. Brun, F. Bruyant and M. Maire.